Determination and analysis of land deformation in major landslide areas in Kenya using geospatial techniques: A case study of Murang'a and Nyeri counties

Alex Yumbu
YMBALE001

Department of Architecture, Planning and Geomatics: Division of Geomatics
Faculty of Engineering and the Built Environment

Thesis submitted in fulfilment of the requirements for the Degree of
Master of Science in Engineering (Geomatics) at the
University of Cape Town

Supervisor:
Associate Professor Patroba Achola Odera

March, 2024

Copyright Declaration

Authorship Declaration

I know that plagiarism is wrong and that I cannot use another author's work and pretend that it is my own. This thesis is my own work.

Each significant contribution to, and quotation in this thesis from the work(s) of other people has been attributed, and has been cited and referenced.

The work in this thesis has not previously been published in whole or in part for the award of any degree.

Name: **Alex Yumbu**

Date: **March, 2024**

Signature: Signed by candidate

Research Ethics Declaration

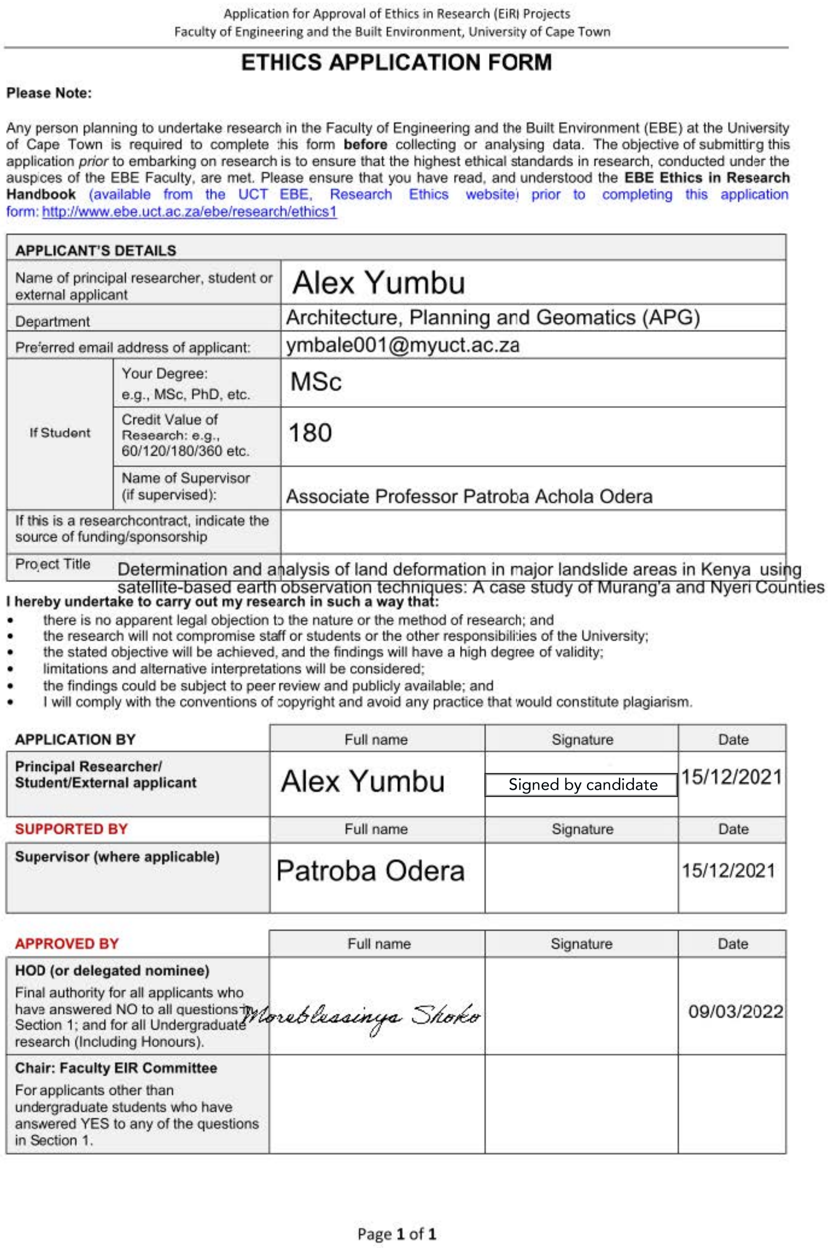

Application for Approval of Ethics in Research (EiR) Projects
Faculty of Engineering and the Built Environment, University of Cape Town

ETHICS APPLICATION FORM

Please Note:

Any person planning to undertake research in the Faculty of Engineering and the Built Environment (EBE) at the University of Cape Town is required to complete this form **before** collecting or analysing data. The objective of submitting this application *prior* to embarking on research is to ensure that the highest ethical standards in research, conducted under the auspices of the EBE Faculty, are met. Please ensure that you have read, and understood the **EBE Ethics in Research Handbook** (available from the UCT EBE, Research Ethics website) prior to completing this application form: http://www.ebe.uct.ac.za/ebe/research/ethics1

APPLICANT'S DETAILS		
Name of principal researcher, student or external applicant		Alex Yumbu
Department		Architecture, Planning and Geomatics (APG)
Preferred email address of applicant:		ymbale001@myuct.ac.za
If Student	Your Degree: e.g., MSc, PhD, etc.	MSc
	Credit Value of Research: e.g., 60/120/180/360 etc.	180
	Name of Supervisor (if supervised):	Associate Professor Patroba Achola Odera
If this is a researchcontract, indicate the source of funding/sponsorship		
Project Title		Determination and analysis of land deformation in major landslide areas in Kenya using satellite-based earth observation techniques: A case study of Murang'a and Nyeri Counties

I hereby undertake to carry out my research in such a way that:

- there is no apparent legal objection to the nature or the method of research; and
- the research will not compromise staff or students or the other responsibilities of the University;
- the stated objective will be achieved, and the findings will have a high degree of validity;
- limitations and alternative interpretations will be considered;
- the findings could be subject to peer review and publicly available; and
- I will comply with the conventions of copyright and avoid any practice that would constitute plagiarism.

APPLICATION BY	Full name	Signature	Date
Principal Researcher/ Student/External applicant	Alex Yumbu	Signed by candidate	15/12/2021
SUPPORTED BY	Full name	Signature	Date
Supervisor (where applicable)	Patroba Odera		15/12/2021

APPROVED BY	Full name	Signature	Date
HOD (or delegated nominee) Final authority for all applicants who have answered NO to all questions in Section 1; and for all Undergraduate research (Including Honours).	Moreblessings Shoko		09/03/2022
Chair: Faculty EIR Committee For applicants other than undergraduate students who have answered YES to any of the questions in Section 1.			

Page **1** of **1**

Abstract

This thesis presents a meticulous investigation into determining and analysing land deformation in the prominent landslide-prone areas of Kenya, specifically within the central highlands encompassing Murang'a and Nyeri counties. The research employs a spectrum of areal deformation methods, including Small Baseline Subset (SBAS) Interferometric Synthetic Aperture RADAR (InSAR) from processed ALOS PALSAR and Sentinel-1 datasets, Gravity Recovery and Climate Experiment (GRACE/GRACE-FO) satellite data, and hydrological modelling data from the Global Land Data Assimilation System (GLDAS), to elucidate and dissect the time series deformation trends prevalent in the study area.

A multi-faceted methodology was employed to investigate the deformation induced by landslides in the study area. Various datasets were harnessed to provide a comprehensive understanding of the phenomena. Satellite gravimetry data from GRACE and GRACE-FO, in conjunction with hydrological modelled data from GLDAS, delivered valuable insights into vertical deformation rates at selected points of interest. These points were identified through InSAR processing using RADAR imagery from Sentinel-1 and ALOS PALSAR, which offered finer spatial resolution. While Sentinel-1 imagery was acquired and processed in both the ascending and descending nodes, ALOS PALSAR imagery was solely processed in the ascending node due to dataset availability constraints. In the Sentinel-1 SBAS analysis, temporal and perpendicular baselines were constrained to 60 days and approximately 200 metres, respectively. For ALOS PALSAR imagery, the temporal and perpendicular baselines were constrained to 875 days and 2500 metres, respectively.

Furthermore, to discern the most probable causes of deformation, a range of factors were considered. These encompassed precipitation data, which was critical in assessing the role of rainfall in triggering landslides. Additionally, geomorphological factors, such as slope, aspect, and surface roughness, extracted from SRTM Arcsecond DEM were incorporated. Land Use Land Cover data spanning from 1973 to 2022 were analysed to understand the impact of human activities and land cover changes on the occurrence of landslides. The amalgamation of these datasets and analyses facilitated a comprehensive examination of the factors contributing to deformation and landslides in the study area.

Results reveal distinctive deformation patterns over the study area from various datasets. Sentinel-1 Ascending imagery indicates varying uplift rates from 19.8 to 189.3 mm/yr and varying subsidence rates from -169.4 to -63.8 mm/yr over the area of study. Sentinel-1 Descending data corroborates these trends, with varying uplift rates from 59.5 to 209.9 mm/yr, and varying subsidence rates from -200.8 to -90.7 mm/yr. Results from the ALOS PALSAR dataset contributes additional complexity but with lower values than Sentinel -1 data, probably due to data gaps. The rates of uplift observed from ALOS PALSAR dataset vary from 16.5 to 100.8 mm/yr, while the rate of subsidence vary from -715.9 to -60.8 mm/yr. GRACE/GRACE-FO and GLDAS datasets provide smaller values of uplift and subsidence at a larger scale, devoid of large deformations at smaller scales captured by InSAR.

Among investigated possible causes of landslides, geomorphological factors emerge as prominent influencers of deformation patterns, while changes in land use and land cover, high and extreme rainfall events and lithology and soil properties also play pivotal roles. Crucially, this thesis underscores that landslides and deformation are rarely attributed to single causative agents; rather, they result from an intricate interplay of various factors, often occurring simultaneously.

Acknowledgements

The completion of this thesis would not be possible without the input of various people and entities.

I acknowledge my heavenly Father for carrying me thus far in my academic journey. He has continously been with me and shone His face upon me. I would not be crossing the finish line without His grace.

I would like to extend my profound gratitude to my supervisor, *Assoc Prof. Patroba Achola Odera*, for his knowledge, support, guidance and constructive feedback during the execution and writing of this thesis. His office always remained open for consultation.

My father, *Josephat Kinyele*, has selflessly invested in my education. I acknowledge, with thanks, not only his efforts and sacrifices but also his unwaivering support and faith in me.

I also would like to offer my graditude to my mother, *Angela Musyoka*, for her prayers, words of motivation and general support. Her thoughts and words always seemed to be heaven sent during hard times.

To my younger sister, *Natasha Yumbu*: you motivate me to pave the path and be a model older sibling. I am thankful for all the light moments we shared when you called to either check on me or just chat.

I am grateful to my extended family for their understanding and support during the time it took to conduct and finalise my research.

I would like to apprecite the Geomatics teaching stuff, *Prof. Jennifer Whittal*, *Assoc Prof. Patroba Odera*, *Assoc Prof. Julian Smit* (former staff member), *Assoc Prof. Simon Hull*, *Dr. Moreblessings Shoko*, *Dr. Siphiwe Mphuti*, *Mr. Kaveer Singh*, for providing me with tutoring and teaching opportunities. These opportunities enabled me to consolidate the knowledge gained during my undergraduate studies while enabling me to pursue my passion of mentorship.

I would also like to extend my gratitude to the Geomatics technical staff. *Ms. Mignon Wells*, provided technical support when it came to setting up my personal workspace and the installation of software. She was available when I needed to run ideas past her during my data processing and analysis. *Ms. Suleiga Schröder* provided me with the opportunity to get hands on experience with various Geomatics

related instrumentation during testing of various equipment and tutorial preparation. *Mr. Dirk Matthee* provided advice on the technical aspect of conducting field work when the need arose.

Special thanks to the *UCT HPC* centre and its team led by *Andrew Lewis.* The computing resources provided enabled me to gain ground especially when processing InSAR data.

To my colleagues, *Epie Njume* and *Dianah Abeho*, I appreciate the camaraderie and all the light momments we shared in the lab as we worked. I wish you the best in your future endeavours.

To *McDonald and Jacqui Nzuwa*, I am forever indebted to your kindness, support and comforting words during the period in which I conducted this research. You went out of your way to check on me and even make me meals whenever you could. I am thankful for your friendship and companionship.

Kipusa, though our worlds are separated by miles and cultures, fate orchestrated a chance encounter that brought us together for a mere glimpse in the grand scheme of life. You have been a reminder that connections can transcend borders and cultures, even when circumstances dictate otherwise. Your support during this journey has been like a ray of sunshine on a cloudy day – simple, yet profoundly uplifting. Your unwavering faith and encouragement were constants in a sea of uncertainties. Though your presence in my life was brief, its impact was unquestionably significant and substantial. You were the muse that inspired me to persevere, the motivation that propelled me forward, and the solace that provided respite from the rigours of academic pursuit. You were the unexpected but welcome guest at the table of my endeavours, and I am thankful for the moments we shared. As our paths diverge, please know that your contribution to my academic pursuits will always be remembered. I will carry the memory of your encouragement, the echoes of your laughter, and the enduring sarcasm you brought to my life. You may be leaving, but your support will forever remain a part of my journey.

There are numerous other people who contributed to the completion of this research, I cannot name all of you by name, my apologies. I am grateful for the role you played in helping me get to this point.

Dedication

"Her thoughts were all so full of us,
She could never forget!
And so I think that where she is
She must be watching yet." (Anne Widdemer)

To my grandmother, ***Jullianah Makasi Musyoka****, who passed away during the writing of this dissertation. Your memory inspires me daily. Continue resting in peace until we meet again on that beautiful shore.*

Contents

List of Tables

List of Figures

List of Abbreviations

1D One-Dimensional

3D Three-Dimensional

ADM Areal Deformation Measurement

ALOS Advanced Land Observtion Satellite

ASF Alaska Space Facility

BU Built-up index

CLSM Catchment Land Surface Model

CNES Centre National d'Etudes

CORS Continually Operating Reference Stations

CSR Centre for Space Research

DAAC Distributed Active Archive Center

DEM Digital Elevation Model

DORIS Doppler Orbitography and Radiopositioning Intergrated by Satellite

EGM2008 Earth Gravitational Model 2008

EM Electromagnetic

Envisat Environmental Satellite

ERS European Remote sensing Satellite

EWT Equivalent Water Thickness

GB-InSAR Ground Based InSAR

GF Gaussian Filter

GFZ German Research Center for Geosciences

GLDAS Global Land Data Assimilation System

GNSS Global Navigation Satellite System

GPS Global Positioning System

GRACE	Gravity Recovery and Climate Experiment
GRACE-FO	Gravity Recovery and Climate Experiment Follow On
ICEGEM	International Center for Global Earth Models
IGiK	Instytut Geodezji i Kartografii
InSAR	Interferometric Synthetic Aperture RADAR
JAXA	Japan Aerospace Exploration Agency
LoS	Line of Sight
LULC	Land Use Land Cover
MNDWI	Modified Normalized Difference Water Index
MTI	Multi-Temporal InSAR
NASA	National Aeronautics and Space Administration
NDBI	Normalized Difference Built-up Index
NDVI	Normalized Difference Vegetation Index
NIR	Near Infrared
PALSAR	Phased Array type L-band Synthetic Aperture Radar
PSI	Permanent Scatterer Interferometry
RADAR	Radio Detection And Ranging
SAR	Synthetic Aperture RADAR
SBAS	Small Baseline Subset
SLR	Satellite Laser Ranging
SRTM	Shuttle Radar Topography Mission
STAMPS	Stanford Method for Persistent Scatterers
SWIR	ShortWave Infrared
TAMSAT	Tropical Applications of Meteorology using SATellite data
TVGMF	Temporal Variations of Gravity/Mass Functional
USGS	United States Geological Survey
VLBI	Very Long Baseline Interferometry
VLF-EM	Very Low Frequency ElectroMagnetics

List of Variables

Variable	Representation	Units
θ	Angular distance from point mass load	rad
r, ϕ, λ	Spherical geocentric coordinates of computation point	m, rad
Φ	Phase values of SAR images	rad
$\Phi_{def,j}$	Deformation phase values between times t_B and t_A	rad
$\Phi_{atm,j}$	Atmospheric phase error	rad
$\Phi_{orb,j}$	Residual errors due to orbit inaccuracies	rad
$\Phi_{\Theta,j}$	Residual phase due to look angle error	rad
$\Phi_{noise,j}$	Random noise phase	rad
$\delta_{\Delta,A}$	Standard deviation of the amplitude difference between master and slave images	arbitary units
$\mu_{\Delta,A}$	Mean amplitude	arbitary units
$\psi_{x,1}$	Wrapped phase	rad
$\tilde{\psi}_{x,1}$	Spatially uncorrelated term	rad
$\varDelta\tilde{\phi}_{\theta,x,i}$	Spatially correlated term	rad
a	Equitorial radius/Semi-major axis length	m
ρ_{ave}	Average density of the Earth's crust	kg/m^3
ρ_w	Water density	kg/m^3
C^W_{nm}, S^W_{nm}	Normalised Spherical harmonic coefficients of degree n and order m	dimensionless
C^T_{nm}, S^T_{nm}	Topographic potential spherical harmonic coefficients of degree n and order m	dimensionless
$C^\sigma_{nm}, S^\sigma_{nm}$	Surface density spherical harmonic coefficients of degree n and order m	dimensionless
h_n, k_n	Load love numbers of degree n	dimensionless
$j - th$	Interferogram number/position	N/A
M	Earth's mass	kg
m_i	Amplitude of master image	arbitary units
P_{nm}	Normalised Legendre functions	N/A
R	Earth's radius	m
s_i	Amplitude of slave image	arbitary units
x, r	Azimuth and Range pixel coordinates	m
t_A, t_B	Acquisition times of SAR images ($t_B > t_A$)	N/A

Chapter 1

Introduction

1.1 General Background

Landslides are natural hazards that pose significant threats to human lives, infrastructure, and the environment (Maina et al. 2013, Ngecu et al. 2004, Zhou et al. 2020). The devastation caused by landslides has increased in recent times. Globally landslide induced deaths have totalled 32 322 between the years 2004 and 2010 (Zhou et al. 2020).

Even though landslides are a prehistoric issue, landslide events continue to plague the world. Advances in technology have done little to alleviate the brunt borne by humans when landslides occur. In fact, as our population grows and societies becomes more intricate these events will become more rampant (Maina et al. 2013). As a result, the costs associated with the effects of landslides will also increase.

In Kenya, an increase in the population has led to the encroachment of settlements onto steep slopes and mountainous areas. These areas are landslide hazards and form a serious threat to both the well-being of the inhabitants and their assets (Davies 1996). Human activities, like farming on steep slopes, deforestation, overgrazing and moving large earth quantities i.e., through excavations, further increase the risk of landslides in these areas (Ngecu et al. 2004).

Landslides in Kenya exhibit spatial variability, as shown in Figure 1, primarily influenced by geological, topographic, and climatic factors (Davies 1996, Maina et al. 2013, Ngecu et al. 2004, Ngecu & Mathu 1999). The country's geological setting is characterised by a variety of rock types, including volcanic, metamorphic, and sedimentary formations, which contribute to varying slope stability conditions (Ngecu et al. 2004). Additionally, Kenya experiences a wide range of rainfall patterns, with intense and prolonged rainfall events acting as triggers for landslide events (Ngecu & Mathu 1999).

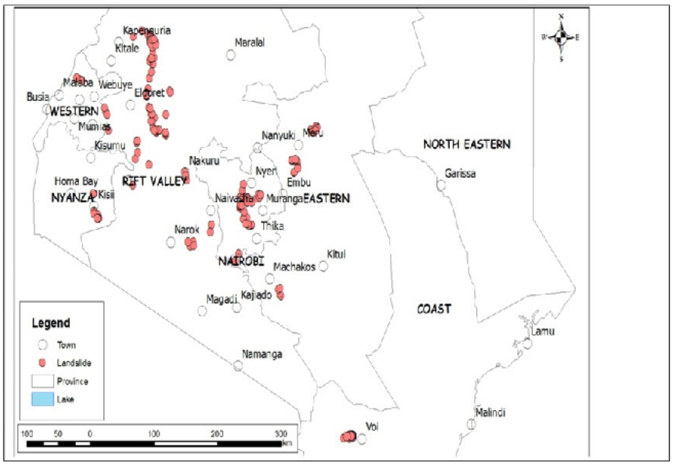

Figure 1: Distribution of landslide events in Kenya. Source: (Maina et al. 2013)

The Western region, including areas around Mount Elgon, is prone to landslides due to its steep slopes, young volcanic formations, and heavy rainfall (Knapen et al. 2006). The Rift Valley region, especially areas such as Nakuru, Baringo, and Narok counties, is also prone to landslides due to its complex tectonic activity, steep escarpments, and intermittent heavy rainfall (Zhou et al. 2020).

In addition to the Western and Rift Valley regions, other areas such as parts of the Central highlands, including Murang'a and Nyeri counties as seen in Figure 2, have experienced recurrent landslides due to their steep slopes, geologically complex formations, and rainfall patterns(Maina et al. 2013). These regions have been subjected to significant socio-economic losses as a result of landslides. Additionally, the recurrent landslides pose ongoing threats to local communities and infrastructure.

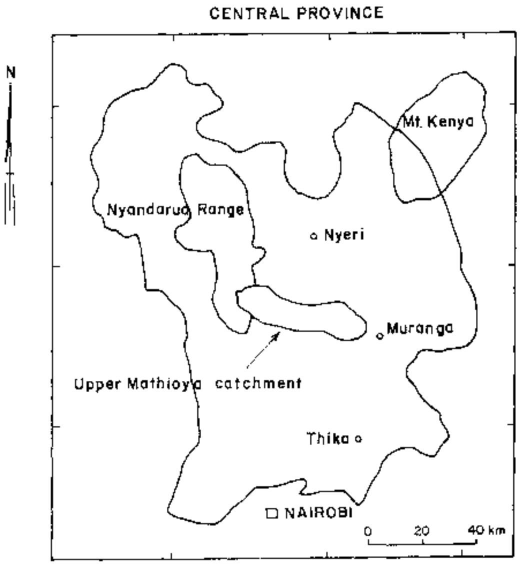

Figure 2: The major landslide areas in the now defunct Central province. Source: (Davies 1996)

These areas are fertile and highly populated. As these areas contribute to the food security of the country, landslides are a bother to the farmers and the government as well (Ngecu et al. 2004). Constructing and maintaining infrastructure in these areas has proven to be not only cumbersome but also expensive due to the damage left in the wake of landslides (Murang'a County Government 2021)

Murang'a and Nyeri counties, as illustrated in Figure 3, have been discerned as regions inherently susceptible to recurrent landslides, warranting their selection as the primary focus of this research. Further justifications for the choice of the study area are expounded upon in Section 1.2.

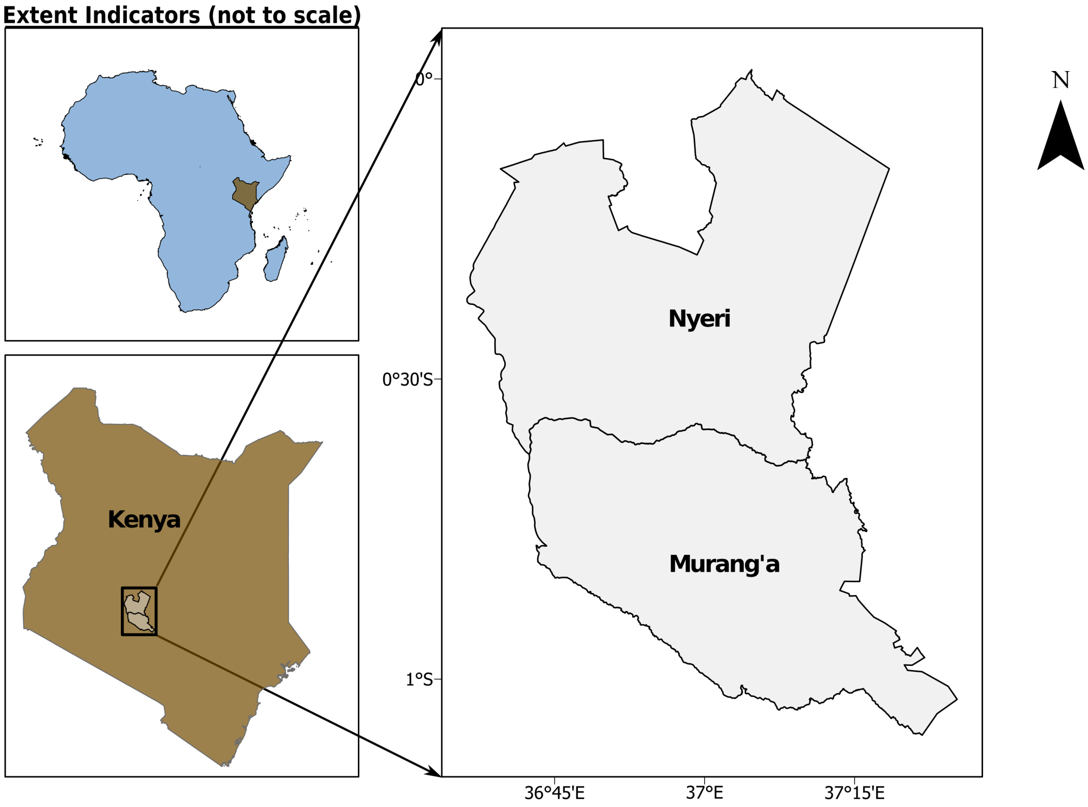

Figure 3: Murang'a and Nyeri Counties

Murang'a county, situated in the central highlands, features steep slopes, deep valleys, and elevated plateaus (Murang'a County Government 2021), while Nyeri county has a rugged topography with mountain ranges, gorges, and undulating hills (Nyeri County Government 2022). Both counties experience moderate to high rainfall, making landslides a significant threat to local populations, who rely heavily on agriculture (Murang'a County Government 2021, Nyeri County Government 2022). These counties are highly susceptible to landslides in part due to their unique geography and climate.

Nyeri County, situated approximately between the longitudes 36° 38' E and 37° 20' E, and between the equator and the latitude 0° 38' S, encompasses an area of approximately 3337.2 km^2 (Nyeri County Government 2022). It shares borders with Laikipia, Kirinyaga, Murang'a, Nyandarua, and Meru counties to the North, East, South, West, and North-East respectively. The county's topography varies, with the highest elevation point being Mount Kenya, rising to approximately 5000 m above mean sea level in the East. The Western region of the county is relatively flat, while the Southern part is characterised by rugged terrain, consisting of steep ridges, valleys, and hills (Nyeri County Government 2022).

Being located within the highland region, Nyeri experiences equatorial rainfall. The long rainy season from March to May brings rainfall ranging between 1200 mm to 1600 mm, while the short rainy season from October to December receives precipitation between 500 mm to 1500 mm (Nyeri County Government 2022). The combination of elevation, geology, and heavy rainfall makes the county susceptible to landslides, compounded by changes in land use due to population growth.

Murang'a County, positioned approximately between the longitudes 36° 30'E and 37° 27' E, and between the latitudes 0° 34' S and 1° 7' S, spans an area of approximately 2558.8 km^2 (Murang'a County Government 2021). It shares borders with Nyeri, Kiambu, Nyandarua, and Kirinyaga counties to the North, South, West, and East respectively, as well as Embu and Machakos counties to the East. The elevation in Murang'a ranges from approximately 1000 m above mean sea level in the West to 3353 m above mean sea level in the East (Murang'a County Government 2021).

The county exhibits three distinct climatic regions, including equatorial, sub-tropical, and semi-arid conditions in the West, Central, and East respectively. Similar to Nyeri, Murang'a experiences a long rainy season from March to May and a short rainy season from October to December (Murang'a County Government 2021). The county's topography is rugged, contributing to its vulnerability to landslides. Factors such as changing land use patterns and population growth further increase the landslide risk in the area.

Figure 4 illustrates the geomorphological and lithological characteristics, along with soil properties, of the study area. Spanning an elevation range from 1048 m to 4960 m above sea level, the region exhibits distinct topographical variation. The lower lying areas, situated in the South-East, sharply contrast with the elevated terrain in the North-East and West, hosting Mount Kenya and the Aberdare ranges, respectively. The slope inclination varies from zero degrees to a maximum of 72 degrees, with the steepest slopes apparent in the North-Eastern and Western sections. The prevailing aspect in the study area is South-East facing, while the Western slopes exhibit either North-East or Eastward orientations, and the Eastern slopes face South-West or Westward. Surface roughness, a measure of terrain ruggedness, ranges from zero to 0.29, indicating a spectrum from smooth landscapes to densely forested or vegetated areas. The predominant geological composition comprises igneous volcanic formations, with smaller sections of precambrian proterozoic formations and sedimentary rocks in the southwest. Clayey soils dominate the region, with pockets of loamy and sandy soils in the Northern portions, reflecting the diverse soil composition within the study area.

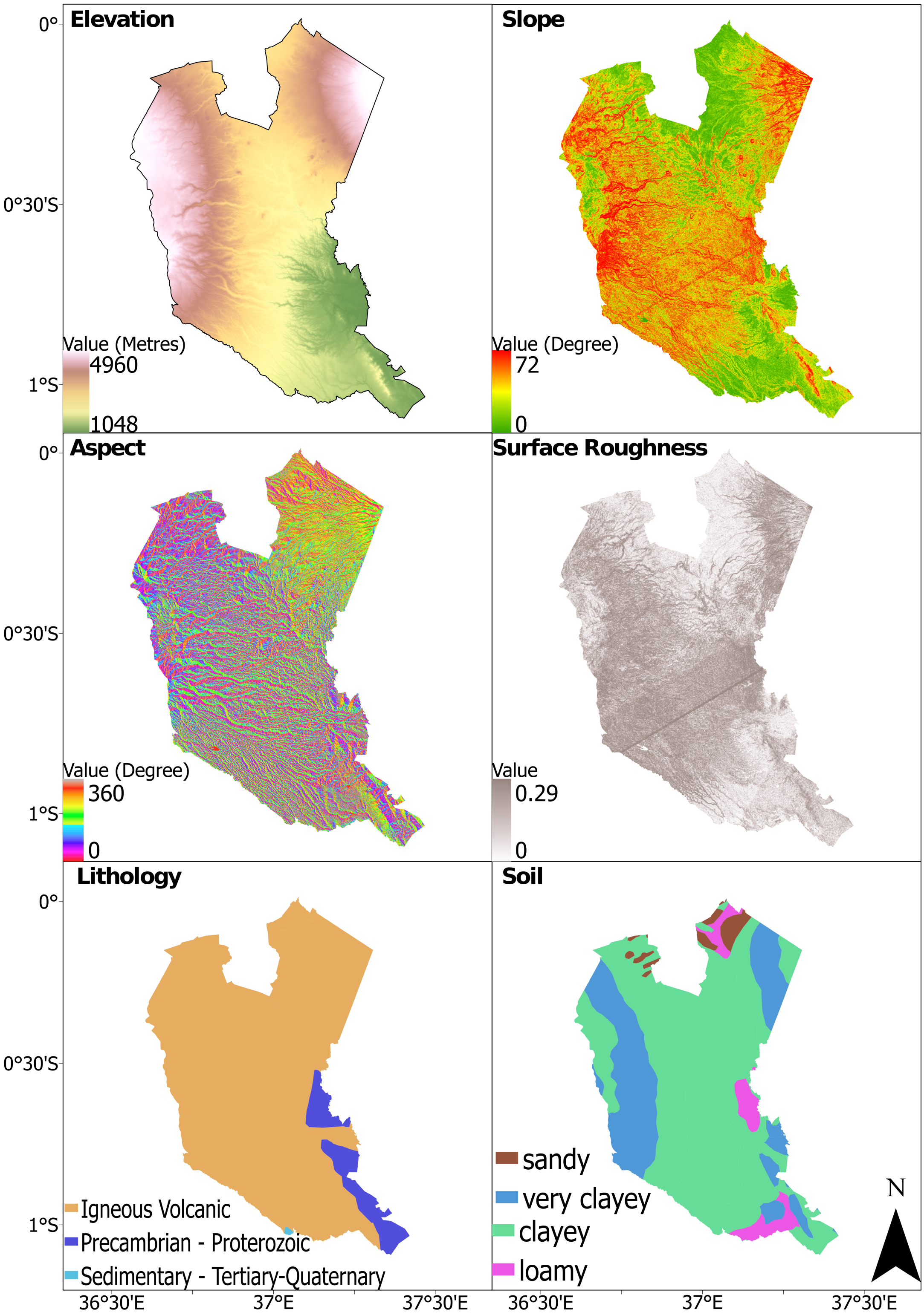

Figure 4: Murang'a and Nyeri's geomorphological factors

Understanding the dynamics and deformation patterns of landslides is crucial for effective hazard assessment, mitigation, and land management strategies (Zhou et al. 2020). Geospatial tools, such as, Geographic Information System (GIS), Global Navigation Satellite Systems (GNSS), Interferometric Synthetic Aperture RADAR (InSAR), hydrological models, and sensors on board satellites like Gravity Recovery and Climate Experiment (GRACE) and its successor Gravity Recovery and Climate Experiment Follow-On (GRACE-FO), are powerful tools for monitoring and analysing land deformation associated with landslides. By integrating these techniques with field investigations and geotechnical data, a comprehensive understanding of the spatial and temporal characteristics of landslide movements can be achieved.

This research project determined and analysed land deformation in major landslide areas within the Murang'a and Nyeri counties of Kenya, by utilising a range of geospatial techniques, including InSAR, hydrological modelling data, and satellite-based observations from sensors aboard GRACE and GRACE-FO data. These techniques offer unique capabilities for monitoring and quantifying various aspects of landslide-induced deformation, enabling a comprehensive assessment of the landslide processes and their impacts on the landscape.

The primary focus was investigating the extent, magnitude, and patterns of land deformation associated with landslides, with the goal of improving our understanding of the underlying mechanisms and potential triggers. InSAR, a RADAR-based technique, was employed to measure surface displacements with high precision, providing insights into the deformation patterns over time.

Moreover, the application of satellite-based techniques such as GRACE and GRACE-FO enabled the assessment of mass redistribution and gravitational changes in Kenya as a whole. These missions utilise the variations in Earth's gravity field to infer mass movements, including the displacement of soil and water caused by landslides (Chen et al. 2022). By analysing the temporal changes in gravity signals, valuable information about the extent and magnitude of land deformation can be obtained (Chen et al. 2022, Godah 2019, Wouters et al. 2014).

Hydrological models played a crucial role in this research project by simulating the behaviour of water in the study area. By integrating rainfall data, soil moisture, and terrain characteristics, hydrological models can provide insights into the hydrological conditions leading to increased pore pressure and slope instability, contributing to landslide occurrence and deformation(Bogaard & Greco 2015, Greco et al. 2023).

Through the comprehensive utilisation of geospatial techniques, including InSAR, GRACE and GRACE-FO, and hydrological models, this research project aimed to contribute to an enhanced understanding of land deformation in major landslide areas of Murang'a and Nyeri counties. The findings will not only advance the scientific understanding of landslides but also provide valuable information for effective landslide hazard assessment, land-use planning, and the development of targeted mitigation strategies in landslide-prone regions.

1.2 Problem Statement

Despite the vulnerability of Murang'a and Nyeri counties to landslides, there is a research gap regarding the deformation induced by these events. Previous studies in Kenya (Davies 1996, Maina et al. 2013, Ngecu & Mathu 1999, Ngecu et al. 2004, Njiraini et al. 2022) have focused on landslide occurrence and triggering factors, without thoroughly investigating land deformation. Moreover, deformation studies have primarily concentrated on the Rift Valley (Biggs et al. 2009, Dindi 2015, Kirui et al. 2023, Koros & Agustin 2017) and Nairobi (Kirui et al. 2022, Sahadevan & Pandey 2021) neglecting the central highlands.

The techniques utilised in these studies include Very Low Frequency Electromagnetics (VLF-EM), magnetics, gravity methods, survey data and InSAR. VLF-EM is a geophysical method that can be utilised in detection of subsidence zones. This method determines deformation due to changes in conductivity in minerals contained in the earth's crust. VLF-EM systems utilise radiation in the VLF band of the electromagnetic spectrum (Dindi 2015). Magnetometers measure the magnetic field strength while gravimeters measure gravity anomalies at a point. Dindi (2015) used the above-mentioned methods to identify potential subsidence zones in Nakuru.

Although these methods showed promise in identifying deformation zones, they are limited to point measurements and they are not only labour intensive but also time consuming if large areas are to be studied. As a result they are uneconomical. Biggs et al. (2009) and Koros & Agustin (2017) carried out deformation and subsidence studies respectively using the InSAR technique. Biggs et al. (2009) determined the deformation due to inflation and deflation of volcanoes, as a result of plate tectonics, in the Kenyan Rift Valley system. SAR images in different temporal periods from the satellites ERS1, ERS2 and EnviSat were utilised in the study.

In Koros & Agustin (2017) EnviSat SAR images were used to determine subsidence due to geothermal extraction in Olkaria. InSAR determines displacement through stacking two or more SAR images (Koros & Agustin 2017). The displacement determined is usually in the Line of Sight (LoS) of the satellite. The temporal resolution of the SAR images used in the mentioned studies was coarse i.e., it sometimes spanned various months between two image acquisitions. Although this technique allows for large areas to be studied, it is computationally intensive and requires specialised software. The availability of historic precise levelling data was constrained to a single epoch, thereby impeding the feasibility of constructing a comprehensive time series for the study.

In both Kirui et al. (2022) and Sahadevan & Pandey (2021) the Small Baseline Subset (SBAS) algorithm was employed to process Synthetic Aperture RADAR (SAR) images, generating both time series deformation for the greater Nairobi region. The algorithm prioritised pairs of short spatial and temporal baselines exhibiting high coherence, leading to the creation of interferograms. Subsequently, the time series displacement output was derived from these interferograms, and linear deformation rates were computed through the fitting of lines to the deformation time series.

Although the analyses from both studies focused on Line of Sight (LOS) measurements, Sahadevan & Pandey (2021) considered them as vertical deformations while assuming minimal horizontal motion influence. Sahadevan & Pandey (2021) also validated the ground deformation estimates obtained through Differential Interferometric SAR (DInSAR) using GNSS data from a station located in the North-Eastern part of Nairobi. The data was collected over the period 2008 to 2018. The GNSS data provided precise 3D point positioning measurements, enhancing the reliability and comprehensiveness of the deformation analysis.

Although geospatial techniques like InSAR, GNSS, and levelling surveys and geophysical techniques like VLF-EM, magnetic and gravity surveys have been used independetly to quantify deformation in the various deformation studies in Kenya, their application has been limited to specific regions, with minimal research in the central highlands, particularly Murang'a and Nyeri counties.

Therefore, there is a significant need for comprehensive studies on landslide induced deformation in Murang'a and Nyeri counties.

1.3 Research Aims

The main aims of this research are to:

i. Investigate and quantify land deformation in the landslide-prone regions of Murang'a and Nyeri.

ii. Identify the underlying causal factors of these mass movement events in the region.

1.4 Research Questions

i. What are the rates of deformation in the chosen study area according to InSAR processed data?

ii. What are the rates of deformation in the study area according to GRACE/GRACE-FO and Hydrological model processed data?

iii. How do the rates obtained in i and ii compare?

iv. What is the general trend of deformation in the study area?

1.5 Research Objectives

The objectives of this research are to:

i. Quantify the deformation in the study area.

ii. Determine the main causes of surface mass movements in the chosen area of study.

iii. Investigate correlation between various causative factors and deformation in the study area.

1.6 Scope and Limitations of Study

Scope of the Study: This dissertation confines its focus to the geographical regions of Murang'a and Nyeri. The study meticulously examines surface deformation exclusively in the vertical and Line of Sight (LoS) component within these specified areas.

Limitations:

Absence of Historic Survey Field Data: The primary limitation of this research arises from the absence of historic survey field data in the study area. The unavailability of such data precludes the establishment of a historical baseline for comparative analysis, restricting the ability to discern trends or patterns in surface deformation over time.

Data Validation Constraints: Owing to the absence of historic survey field data and GNSS or levelling observations, the dissertation encounters limitations in terms of data validation. The unavailability of these reference datasets makes it challenging to assess the accuracy and reliability of the determined surface deformations.

Software Constraints: The methodology employed for determining deformation relies on Interferometric Synthetic Aperture RADAR (InSAR) technology. However, due to software constraints, the analysis is confined to LoS deformation. This limitation restricts the comprehensive understanding of three dimensional surface movements, providing only a partial perspective on the deformations detected.

Despite these limitations, the dissertation strives to contribute valuable insights into the vertical component of surface deformation in Murang'a and Nyeri. The outcomes of this study should be interpreted within the specified scope, acknowledging the constraints inherent in the available data and methodology. Recommendations for future research are provided in Chapter 5 to address these limitations and further enhance the understanding of surface deformation in the study area.

1.7 Outline of Chapters

This dissertation is structured to comprehensively investigate the dynamics of surface deformation in the specific study area. The following chapters provide a detailed exploration of various aspects related to mass movements, deformation detection techniques, and the subsequent analysis of results.

Chapter 1: Introduction

The inaugural chapter sets the stage for this research, presenting a broad perspective on the chosen topic while meticulously delving into the study area's particulars. A thorough background is provided, justifying the necessity of this research. Within this context, the chapter explicitly formulates research questions and objectives, establishing the framework for subsequent investigations. The scope and limitations of the study are also transparently outlined, providing a clear boundary for the research.

Chapter 2: Literature Review

Building upon the foundational understanding established in Chapter 1, the second chapter conducts a comprehensive review of existing literature. This includes an in-depth exploration of various mass movement types, their causative factors, and triggers. Furthermore, the chapter critically examines deformation detection techniques and scrutinises previous studies, laying the groundwork for the subsequent chapters.

Chapter 3: Research Design and Methodology

This pivotal chapter intricately details the research design and methodology employed in this study. It elucidates the rationale behind selecting specific techniques to detect, analyse, and determine the causes of surface deformation in the chosen study area. Additionally, the chapter expounds on the datasets utilised, establishing the scientific rigor underpinning the research.

Chapter 4: Results and Analysis

With the research design and methodology in place, Chapter 4 presents the substantive findings of the study. Through a combination of visualisations and textual analysis, this chapter reports and discusses the results obtained. The focus is on providing a comprehensive understanding of the observed surface deformations and their implications.

Chapter 5: Conclusions and Recommendations

The concluding chapter synthesises the research findings in relation to the stated objectives. It draws overarching conclusions that contribute to the broader understanding of surface deformation in the specified study area. Additionally, this chapter formulates practical recommendations based on the results obtained, offering insights for future research and potential applications in relevant fields.

Chapter 2

Literature Review

2.1 Mass movements: An overview

Humans often hold the misconception that the Earth's surface is stable and solid, providing a secure foundation for their settlements (Marshak 2015). However, geologists recognise that the Earth's substrate, particularly on steep slopes consisting of rock or regolith, is inherently unstable and will ultimately succumb to the constant force of gravity. Geologists classify any movement of earth material downslope as mass movement or mass wasting, which encompasses various materials such as rock, regolith, snow, and ice (Guerra et al. 2017, Highland & Bobrowsky 2008, Maina et al. 2013, Marshak 2015). Mass movements are commonly referred to as landslides in popular media and among the general population, emphasising their potential for disastrous consequences (Highland & Bobrowsky 2008).

To effectively understand and address mass movements, geologists and engineers find it crucial to categorise them based on four key aspects: *the type of material involved* (rock or regolith), *the velocity of movement* (fast, slow, or intermediate), *the character of the moving mass* (coherent/chaotic, dry or wet), and *the environmental context in which the movement occurs* such as subaerial or submarine (Marshak 2015, Varnes 1958). This categorisation enables relevant authorities to adequately prepare for and mitigate the risks associated with different types of mass movements, as each category exhibits distinct characteristics and implications.

Creep also known as *soil creep*, is a gradual and slow downslope movement of regolith on a slope (Highland & Bobrowsky 2008, Marshak 2015). This type of mass movement occurs when regolith undergoes continuous expansion and contraction due to processes such as freezing and thawing or wetting and drying (Maina et al. 2013, Marshak 2015). During freezing or thawing, the regolith particles displace outward perpendicular to the slope, and they contract during thawing or drying, subsiding vertically under the influence of gravity and gradually moving downslope (Marshak 2015). Although the process of creep is not immediately noticeable, it can result in long-term effects such as the tilting of structures like fences, walls, and trees downslope (Maina et al. 2013, Marshak 2015) as visualised in Figure 5. In regions with high elevations and in the Arctic Circle, where the regolith may freeze to significant depths, thawing in summer leads to only the upper layers thawing, while the impermeable permafrost causes the melted layer to move downslope under gravity's influence, a phenomenon referred to as *solifluction* (Marshak 2015).

Rock glaciers consist of rock fragments embedded within an ice matrix and represent another form of slow mass movement (Giardino et al. 2011, Marshak 2015). Unlike ice glaciers, which predominantly consist of ice, rock glaciers have a higher proportion of rock fragments relative to ice. They can form through two mechanisms: rainwater percolating into a pile of rock debris above permafrost at the base of a cliff, or as an ice glacier containing sufficient rock debris begins to thaw, resulting in a higher concentration of rock debris compared to ice (Giardino et al. 2011, Marshak 2015). Over time, rock glaciers can experience downslope displacement under the influence of gravity.

Slumps represent another type of slow mass movement, wherein rock and regolith move as a coherent unit known as a slump block (Highland & Bobrowsky 2008, Marshak 2015). The movement occurs along a curved failure surface, resembling the shape of a spoon's bowl, with the exposed upslope edge referred to as the head scarp and the downslope end as the block's "toe" (Highland & Bobrowsky 2008). Slumps, as illustrated in Figure 5, are characterised by the movement of the entire mass without significant separation into debris, differentiating them from other forms of mass movement.

Mudflows or mudslides generally occur in regions with steep slopes and poorly consolidated materials. Heavy rainfall can saturate the regolith, leading to the formation of a slurry of mud that flows downslope as visualised in Figure 5 (Highland & Bobrowsky 2008, Maina et al. 2013). The velocity of mudflows depends on factors such as slope angle and water content, as higher water content and steeper slopes result in faster movement (Marshak 2015). In volcanic regions, mudflows triggered by heavy rains or volcanic eruptions may incorporate volcanic ash and water from melted snow and ice, earning the term *"lahars"*.

Debris flows refer to slurry containing a mixture of mud and larger particles such as pebbles or boulders (Maina et al. 2013, Marshak 2015, Varnes 1958). Debris flows are illustrated in Figure 5.

Rockslides and Debris slides are a type of mass movement characterised by the downward displacement of rock on a sloping surface (Marshak 2015). Rockslides, as displayed in Figure 5, occur when bedrock or regolith becomes detached from a slope, flows downhill along a failure surface, and eventually disintegrates. Debris slides mainly consists of regolith. As a result of these mass movements, a debris pile accumulates at the base of the slope, and a distinct scar forms on the slope.

Rockslides and debris slides are more prevalent in areas where an unconsolidated layer of rock or sediment exists beneath the surface (Varnes 1958). The unconsolidated material often lies parallel to the surface. Rockslides can reach speeds of up to 300 km/h, particularly when there is an air cushion trapped beneath them. The presence of the air cushion reduces the friction that opposes the motion of the slide (Marshak 2015).

Avalanches are characterised by the displacement of a large amount of material mixed with a fluid, either water or air, creating a cloud-like appearance (Maina et al. 2013, Marshak 2015, Varnes 1958). Debris avalanches involve the mixture of regolith or rock material with air, while submarine avalanches occur when the material is mixed with water (Marshak 2015).

Rock Falls and Debris Falls occur when rocks and debris detach from an overhanging cliff and fall downward (Maina et al. 2013, Marshak 2015, Varnes 1958). Rock falls commonly happen when a segment of rock breaks along a joint (Maina et al. 2013, Marshak 2015). These types of mass movements are often observed along roads constructed on or near steep topography, as new cliffs may form during the road construction process.

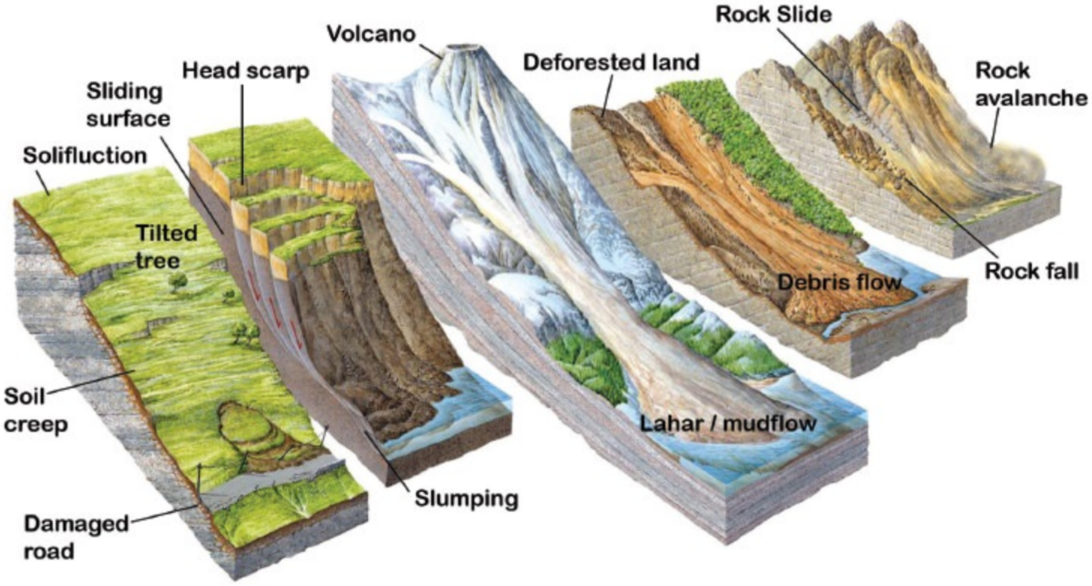

Figure 5: An illustration on the different types of terrestrial mass wasting. Adapted and modified from: (Marshak 2015)

Submarine Mass Movements refer to mass movements that occur underwater. There are three main forms of submarine mass movements: *submarine slumps, submarine debris flows, and turbidity currents* (Marshak 2015). Submarine slumps occur when blocks of sediment are rapidly displaced downslope on weak detachments. These slumps can trigger tsunamis due to the quick displacement of large areas of the seafloor.

In submarine debris flows, the mass disintegrates into a mud-like mixture consisting of sediments. Turbidity currents involve the dispersion of the mass in water, creating a cloud-like sediment mixture that moves downslope similar to an avalanche (Marshak 2015).

2.2 Causes of Mass Wasting

Mass movements occur due to various factors, including fragmentation and weathering of the substrate, slope instability, and triggering events (Marshak 2015).

Fragmentation and Weathering - The Earth's crust is naturally fractured through processes such as jointing and faulting (Marshak 2015). These fractured sections are further weakened through chemical weathering (Varnes 1958). Over time, the combination of weathering and fractures leads to the formation of regolith, which is unconsolidated and prone to breaking away along joints, causing mass movements.

Unweathered bedrock consists of strong chemical bonds that hold its grains together, providing strength. However, weathering weakens these chemical bonds, and the resulting regolith is held together by weaker forces such as friction, electrostatic attraction, and the surface tension of water (Marshak 2015). These weaker forces make the regolith more susceptible to mass movements compared to unweathered material.

Slope Stability - Geologists classify slopes as stable or unstable, with mass movements more likely to occur on unstable slopes (Marshak 2015). Slope failure happens when earth materials are displaced from unstable slopes. The occurrence of mass movements is determined by the balance between the downslope force caused by gravity and the resistance force. If the downslope force exceeds the resistance force, the slope fails, leading to mass movements (Marshak 2015).

The downslope force is greater in steeper slopes for a given mass of earth material. The resistance force often causes debris to pile up, forming the steepest slope before failure, known as the angle of repose (Marshak 2015). This angle typically ranges from 30° to 37° and is influenced by the shape and size of the grains in the earth material, affecting the friction across grain boundaries (Marshak 2015).

In some regions, the magnitude of the resistance force is compromised due to the presence of a weak surface at a certain depth below the ground surface. These weak surfaces, such as wet clay layers, wet unconsolidated sand layers, joints, weak bedding planes, and metamorphic foliation planes, can act as potential failure surfaces during mass movements (Bogaard & Greco 2015, Guerra et al. 2017, Marshak 2015). Weak parallel surfaces beneath the ground or slope surface can also serve as potential failure surfaces.

2.3 Triggers of slope failure

Various factors can disrupt the balance between the downslope force and the resistance force, causing the downslope force to exceed the resistance force. These factors can be natural or man-made triggers (Highland & Bobrowsky 2008).

Shocks, Vibrations, and Liquefaction - Earthquakes and extreme weather conditions, especially heavy rains and strong winds, can trigger mass movements (Guerra et al. 2017, Varnes 1958). The use of explosives in quarries and construction sites, as well as the operation of earth-moving machinery, can also contribute to mass movements. When saturated sediments experience shocks, liquefaction can occur, transforming the wet sediment from a solid state into a slurry (Highland & Bobrowsky 2008, Marshak 2015).

For example, quick clay, which consists of damp clay flakes held together by surface tension, can behave like a solid when undisturbed. However, shaking quick clay separates the flakes, causing it to behave like a fluid slurry. If liquefaction occurs in a layer below the ground surface, it can act as a failure surface triggering mass movements (Highland & Bobrowsky 2008, Marshak 2015).

Changing Slope Loads, Steepness, and Support - Apart from slope stability, other factors can disrupt the balance between the downslope and resistance forces. Changes in slope loads, failure surface strength, slope steepness, and support at the base of the slope can offset this balance (Guerra et al. 2017, Highland & Bobrowsky 2008, Marshak 2015, Varnes 1958).

The slope load can change when the mass of the earth material overlying a failure surface increases. This can occur through the addition of fill during construction, the construction of buildings, or the saturation of earth material from rainwater (Highland & Bobrowsky 2008). Infiltration of water into the ground can lead to the failure of bedrock (Varnes 1958). Slope steepness can vary over time due to natural processes such as river erosion or man-made influences like excavation and construction work (Guerra et al. 2017, Highland & Bobrowsky 2008). If the slope steepness exceeds the angle of repose, the slope becomes unstable and prone to failure (Marshak 2015). Removal of support at the base of a slope can also trigger slope failure, as the material at the base acts as a barrier preventing upslope material from moving down the slope.

Changing Slope Strength - The strength of the slope material plays a significant role in slope stability. Weathering, vegetation cover, and water content influence slope strength (Varnes 1958). Chemical weathering weakens the chemical structure of the material, while physical weathering breaks up rocks. Both processes contribute to the formation of regolith, which can be held together by vegetation roots, increasing slope strength. Vegetation absorbs water from the soil, preventing liquefaction. Deforestation and wildfires can decrease slope strength, making the slope more susceptible to failure (Guerra et al. 2017, Highland & Bobrowsky 2008, Marshak 2015). Heavy rains can saturate burned or deforested areas, leading to liquefaction and slope failure.

Water content in the slope material affects slope strength in various ways. Surface tension due to the water film on slope material grains can help hold regolith in place (Marshak 2015). However, increased water content can push regolith particles apart due to water pressure, potentially causing liquefaction. Water infiltration into the slope material can make underground surfaces slippery or push them apart, reducing friction (Greco et al. 2023, Bogaard & Greco 2015, Guerra et al. 2017).

2.4 Importance of Relief, Climate, Substrate, and Tectonic Setting

The occurrence of landslides is intricately tied to several key environmental factors, each playing a crucial role in determining the susceptibility of a region to mass movements. Relief, which encompasses variations in elevation and slope, holds significant importance as steeper slopes are generally more prone to landslides (Highland & Bobrowsky 2008). The angle of the slope, known as the angle of repose, is a critical factor influencing slope stability (Marshak 2015). Mass wasting, or the movement of earth material down a slope, is fundamentally linked to relief; regions with flatter terrain are less likely to experience mass movements. Conversely, regions with steeper slopes are more susceptible to landslides, emphasising the importance of topographical considerations in landslide susceptibility assessments.

Climate is another pivotal determinant of landslide occurrence. Intense or prolonged rainfall can saturate the ground, increasing the likelihood of landslides. In areas with heavy seasonal rains, the risk of mudflows and slides escalates, particularly if vegetation, a natural stabilizer, has been removed (Guerra et al. 2017, Highland & Bobrowsky 2008, Marshak 2015). In contrast, in deserts and alpine regions where bedrock is typically unweathered, mass movements are less frequent but primarily involve rock falls (Marshak 2015). The freeze-thaw cycles in colder climates contribute to the weakening of slope materials. Furthermore, plate tectonics, which cause faulting and fragmentation of the Earth's crust, add another layer of complexity. Areas near plate boundaries, prone to earthquakes and volcanic activity, are at an elevated risk of landslides (Guerra et al. 2017, Highland & Bobrowsky 2008, Marshak 2015, Varnes 1958). The collective understanding of relief, climate, substrate, and tectonic setting is indispensable for assessing landslide hazards, implementing effective mitigation strategies, and planning sustainable land use in regions susceptible to mass movements.

2.5 Deformation Monitoring and Analysis Techniques

Deformation refers to changes in the position, structure, or size of a deformable object (Ogundare 2015). Deformation monitoring involves detecting the displacement of specific areas on the object, while deformation analysis goes a step further by visualising and modeling the movement of these deformed areas (Ogundare 2015). There are four main categories of deformation monitoring techniques: geodetic, remote sensing, areal deformation measurement, and geotechnical & structural techniques.

2.5.1 Geodetic Techniques

Geodetic techniques involve monitoring a network of points using horizontal and vertical measurements (Erol et al. 2004). It is crucial to have redundant observations to detect errors, and the least squares adjustment is used during the analysis phase (Ogundare 2015). This technique provides information about the global deformation of the object in relation to stable reference points (Erol et al., 2004; Ogundare, 2015).

Geodetic techniques encompass positioning determination methods based on either terrestrial or space-based techniques (Erol et al. 2004). While these techniques offer high precision, they have some limitations. Skilled analysts and observers are required, and the process can be labor-intensive. Without automation, measurements between observation periods are less frequent (Ogundare 2015). However, automated instrumentation can be expensive to procure, install, and maintain. Furthermore, atmospheric refraction, tropospheric delay, intervisibility issues, thermal expansion, and reference point instability can affect the accuracy of measurements (Ogundare 2015).

Here is an overview of the instrumentation used in geodetic techniques:

Optical Collimators - detect displacement in the horizontal plane along the optical line of sight between the setup and a target placed on a point (Scaioni et al. 2018). They provide sub-millimeter or millimeter precision but can be affected by atmospheric refraction and the distance between the setup and the observed point (Scaioni et al. 2018).

Robotic Total Stations (RTS) - measure directions and distances to determine 3D coordinates of the monitored points (Scaioni et al. 2018). They enable automated monitoring, offering nearly real-time 3D coordinate data (Ogundare 2015). However, atmospheric refraction and intervisibility between the setup and reflector can impact measurement accuracy, and this method is limited to discrete points (Ogundare 2015).

Precise Levels - are highly reliable for detecting vertical deformations (Ogundare 2015). It doesn't require direct visibility between the immediate points under observation, making it suitable for complex and confined spaces such as indoor corridors (Scaioni et al. 2018). However, it is time consuming, labour intensive, slow, and provides only 1D information (Ogundare 2015).

Hydrostatic Levels - provides continuous and precise information about 1D deformation (Scaioni et al. 2018). It involves deploying a network of conduits connecting the monitored points, but installation can be challenging and expensive.

Global Navigation Satellite Systems (GNSS) - monitor both slow and fast dynamic deformations (Larson 1995, Ogundare 2015, Omali 2022). This method offers time and cost efficiency, particularly when monitoring a limited number of points compared to other geodetic methods (Scaioni et al. 2018). GNSS provides 3D information in near real-time, and LoS visibility is only required between receivers and satellites, not between deformation points (Ogundare 2015, Scaioni et al. 2018). Expert involvement is mainly needed during the initial design phase of the GNSS ground network.

Each deformation point's analysis involves studying the 3D components between the reference and that point, known as a baseline. Analysing each baseline per observation period reveals the deformation trend of the structure being monitored (Owczarz 2020, Scaioni et al. 2018). Satellite visibility limitations can be overcome by using pseudolites, which offer terrestrial radio ranging to enhance the GNSS satellite constellation in areas with poor satellite geometry or during indoor mapping activities (Erol et al. 2004).

Another limitation of GNSS is its susceptibility to tropospheric retardation of the satellite signals, and multipath errors can also affect the results (Ogundare 2015). While GNSS provides reliable and accurate horizontal measurements, it does not match the precision of precise leveling in the vertical component (Scaioni et al. 2018).

Some commonly used geodetic techniques include:

Levelling - is a technique used to measure the difference in elevation between two or more points on the Earth's surface (Bürgmann & Thatcher 2013, Stefano et al. 2022). This method is particularly valuable in detecting crustal deformation, offering insights into changes in the Earth's surface over time (Zhang et al. 1998).

Levelling begins with the establishment of benchmarks, which are precisely surveyed points with known elevations. These benchmarks act as reference points against which subsequent measurements are compared (El-Ashmawy 2019, Stefano et al. 2022).

A baseline survey is conducted by measuring the elevation differences between benchmarks using levelling instruments (Bürgmann & Thatcher 2013, El-Ashmawy 2019, Stefano et al. 2022). This initial survey provides a baseline understanding of the elevations across the surveyed area.

Levelling is ideally suited for detecting vertical displacements over time (Nie et al. 2023). Repeated levelling surveys are conducted at regular intervals, and the differences in elevation between benchmarks are monitored (Stefano et al. 2022).

As the Earth's crust undergoes deformation due to tectonic forces or other geological processes, changes in elevation occur. Levelling allows the detection of these vertical displacements by revealing shifts in elevation between benchmarks (Bürgmann & Thatcher 2013).

The data collected from levelling surveys is analysed to quantify the amount and direction of vertical crustal deformation (Bürgmann & Thatcher 2013). This information is crucial for understanding the dynamics of the Earth's crust in a specific region.

Levelling is often used in conjunction with other geodetic techniques, such as GNSS measurements and satellite-based observations (Bürgmann & Thatcher 2013). This integrated approach enhances the accuracy and reliability of crustal deformation monitoring.

Triangulation and Trilateration - are techniques that play crucial roles in determining crustal deformation. Triangulation and trilateration methods involve measuring angles and distances respectively, to establish the position of points on the Earth's surface (DiBiase & Dutton n.d.b, Bürgmann & Thatcher 2013). In the context of crustal deformation studies, these techniques provide valuable data for understanding how the Earth's crust is changing over time (Bürgmann & Thatcher 2013).

Triangulation involves forming a network of triangles by measuring angles at selected points (DiBiase & Dutton n.d.a, Jawan et al. 2023). In crustal deformation studies, surveyors select a series of reference points across the terrain. From these reference points, they measure the angles to nearby points and use this angular information to calculate the distances between those points (Bürgmann & Thatcher 2013). The reference points form the vertices of triangles, and the measured angles help establish the sides of these triangles (DiBiase & Dutton n.d.a).

Over time, as the Earth's crust deforms, the distances between the reference points change. Monitoring these changes in distances over a network of triangles provides valuable information about the magnitude and nature of crustal deformation (Bürgmann & Thatcher 2013, Jawan et al. 2023).

Trilateration involves measuring distances between points directly, without necessarily forming triangles (Bürgmann & Thatcher 2013). In trilateration, surveyors measure the straight line distances between selected points using electronic distance measurement devices or other distance measuring techniques (Bürgmann & Thatcher 2013, DiBiase & Dutton n.d.b, Navidi et al. 1998). Unlike triangulation, angles are not directly measured; instead, distances are the primary focus (DiBiase & Dutton n.d.b, Navidi et al. 1998).

For crustal deformation studies, trilateration is particularly useful when precise distance measurements are required (Bürgmann & Thatcher 2013).

Both triangulation and trilateration involve establishing baseline measurements between points (Bürgmann & Thatcher 2013, DiBiase & Dutton n.d.b). In the context of crustal deformation, these baselines act as reference distances. To monitor crustal deformation, surveyors conduct repeated measurements of the same baselines over time. Changes in distances between points indicate how the Earth's crust is deforming. The collected data is analysed to understand the nature of deformation (Bürgmann & Thatcher 2013). It can reveal patterns of strain, identify areas of subsidence or uplift, and contribute to broader studies on seismic activity and tectonic processes.

Trilateration, with its focus on distance measurements, is often more precise than triangulation while triangulation can be more flexible in irregular terrains, where direct LoS measurements may be challenging (Biswas 2019, Bürgmann & Thatcher 2013). Both methods benefit from technological advancements, such as the use of GNSS and electronic distance measurement devices, which enhance accuracy and efficiency (Navidi et al. 1998). The choice between triangulation and trilateration may depend on field conditions, the terrain under study, and the specific objectives of the deformation study. In addition, combining both triangulation and trilateration (triangulateration) techniques allows for the establishment of comprehensive geodetic networks, which can be regularly observed to detect and quantify deformations over time.

Very Long Baseline Interferometry (VLBI) - is a technique that involves measuring the time it takes for radio signals to travel from distant celestial objects, e.g. quasars, to multiple radio telescopes on Earth (Nickola et al. 2023). By analysing the differences in arrival times of these signals, precise measurements of the Earth's rotation and crustal movements can be obtained (Larson 1995, Nickola et al. 2023). VLBI can contribute to monitoring tectonic plate movements, polar motion, and crustal deformations (King et al. 2010, Larson 1995).

Satellite Laser Ranging (SLR) - utilises laser beams to precisely measure the distance between ground based stations and retroreflectors placed on satellites (Botai & Combrinck 2012, Christodoulidis et al. 1985, Larson 1995). By tracking the movement of these satellites over time, SLR can provide highly accurate measurements of Earth's surface deformations, including tectonic plate motions and crustal displacements (Attia et al. 2012, Christodoulidis et al. 1985, Larson 1995). SLR is particularly effective in measuring large scale movements and long-term trends.

Doppler Orbitography and Radiopositioning Integrated by Satellite (DORIS) - is a satellite-based system that uses Doppler shift measurements of signals transmitted by low Earth orbit satellites to precisely determine their positions (Sánchez et al. n.d.). DORIS can contribute to deformation monitoring by providing accurate geodetic measurements, including vertical displacements and crustal movements (Botai & Combrinck 2012, Sánchez et al. n.d., King et al. 2010). DORIS measurements are often combined with other techniques to obtain comprehensive deformation information.

Levelling, Triangulation, trilateration VLBI, SLR and DORIS complement other methods such as GNSS and InSAR, offering additional capabilities for deformation monitoring and analysis. They provide valuable data for understanding geophysical processes, studying tectonic activities, and monitoring the behaviour of Earth's surface over time (Botai & Combrinck 2012).

2.5.2 Areal Deformation Measurement Techniques

Areal Deformation Measurement (ADM) extends deformation monitoring and analysis from a few points to a larger surface (Scaioni et al. 2018). ADM techniques employ the theory of close range photogrammetry (Ogundare 2015). ADM techniques include terrestrial laser scanners (TLS) and terrestrial and aerial photogrammetry (Scaioni et al. 2018).

Photogrammetry – By photographing a deformable object from two or more control points, the position of object points can be computed based on the geometric relationship between the image and object points (Erol et al. 2004). The relative orientation of the cameras should be known for this process to be successful. Aerial photogrammetry can be utilised in ground deformation analysis, while terrestrial photogrammetry is suitable for monitoring engineering structures (Owczarz 2020, Erol et al. 2004).

Advantages of this method are that minimal fieldwork is required, an unlimited number of points can be monitored, and 3D coordinates can be determined simultaneously based on established ground control (Erol et al. 2004). However, this method is limited by the scale of the image (Scaioni et al. 2018).

Terrestrial Laser Scanning (TLS) – TLS is an active sensor that uses a laser to irradiate its targets through a carrier wave (Ogundare 2015). TLS provides a dense 3D point cloud, including point and color information of the targets (Scaioni et al. 2018). Point clouds generated from different epochs can be compared to analyse and determine deformation. However, due to the high density of the observed data, it can be challenging to distinguish deformations from noise (Scaioni et al. 2018).

There is ongoing debate among specialists regarding the calibration and data processing of TLS (Scaioni et al. 2018). Currently, there is no established ”conventional” deformation model based on TLS data collection or processing. TLS is user friendly, making it less labour intensive, enables fast data collection, and is not limited to optical LoS (Ogundare 2015).

2.5.3 Remote Sensing Techniques

Synthetic Aperture RADAR (SAR) is an active sensor system similar to TLS. It is based on the principles of Radio Detection and Ranging (RADAR). SAR systems emit and receive microwave signals in the electromagnetic (EM) spectrum (Ogundare 2015, Owczarz 2020). The radar bands in the EM spectrum range from 108 to 1011 Hz, and Table 1 provides information about the various RADAR bands and their corresponding attributes (Ogundare 2015).

Table 1: Various RADAR bands and their corresponding attributes. Adapted from: (Ogundare 2015)

Frequency Band	Frequency (GHz)	Wavelength (cm)
Ka	40 to 26.5	0.8–1.1
K	26.5 to 18	1.1–1.7
Ku	18 to 12.5	1.7–2.4
X	12.5 to 8	2.4–3.8
C	8 to 4	3.8–7.5
S	4 to 2	7.5–15
L	2 to 1	15–30
P	1 to 0.3	30–100

In this section, ground based and satellite based remote sensing techniques for deformation monitoring and analysis are discussed.

Satellite-based InSAR

Since SAR systems are active sensors, they can acquire data during both day and night. RADAR can penetrate clouds and precipitation, making it unaffected by weather conditions (Ogundare 2015, Omali 2022). Satellite RADAR systems collect data using a single physical antenna over different epochs. SAR systems create repeated RADAR bursts as they move along their orbital path, creating a synthetic aperture, which gives SAR its name (Ogundare 2015). Figure 3 illustrates the basic components of satellite-based SAR.

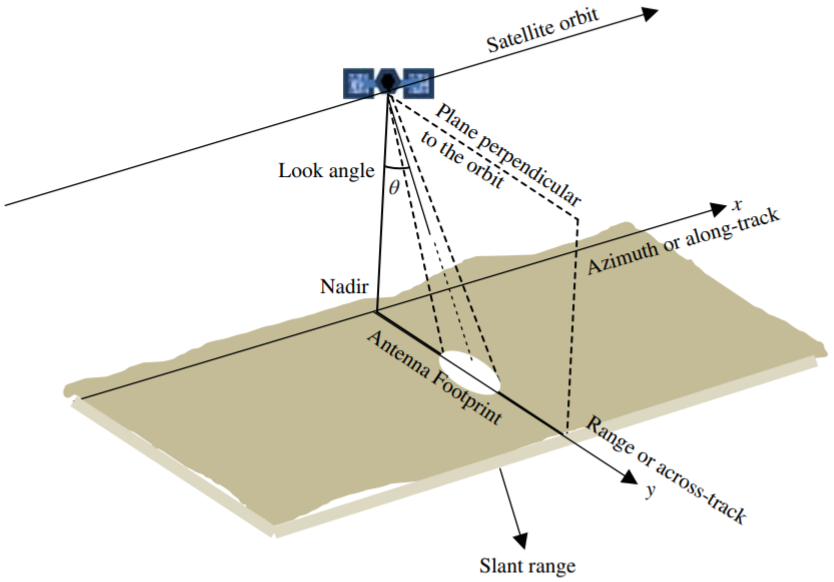

Figure 6: Basic components of satellite SAR systems. Adapted from: (Ogundare 2015)

In Figure 6, the ground coordinates of the radar image are described in the azimuth/along-track direction and the direction of illumination (range) for the x and y coordinates, respectively (Ogundare 2015). The LoS between the satellite and the target is known as the slant range. Deformation from SAR processing is typically observed in the range direction.

InSAR systems consist of either single or dual antennas on the same satellite system (Ogundare 2015). Repeat pass interferometry is an InSAR method where images are acquired from a satellite with a single antenna at different times. Single pass interferometry, on the other hand, uses SAR imagery from a satellite with dual antennas. The images are obtained simultaneously but from different viewing geometries (Ogundare 2015). Both interferometric methods can determine deformations in the centimeter and sub-centimeter range (Erol et al. 2004, Omali 2022).

Advantages of this deformation monitoring method include cost-effectiveness, no fieldwork requirement, and the ability to detect deformations over large areas (Scaioni et al. 2018). However, a limitation of this method is the coherence between SAR images obtained at different epochs. Temporal decorrelation plays a significant role in affecting coherence between images. InSAR also detects deformations in the LoS direction of the satellite, potentially missing deformations perpendicular to this direction (Ogundare 2015, Scaioni et al. 2018). Some sensors that produce SAR imagery suitable for the interferometric process include ALOS PALSAR, Cosmo-Skymed, EnviSat, ERS1, ERS2, RADARSAT-1, RADARSAT-2, Sentinel-1, and TerraSAR-X. These sensors operate in the C, L, or X microwave bands of the EM spectrum (Ogundare 2015).

Ground-Based InSAR (GB-InSAR)

GB-InSAR is a deformation monitoring technique that employs the SAR concept discussed in 2.5.3. The distinction lies in mounting the system on a mechanical track that travels forward and back to map deformation (Ogundare 2015, Scaioni et al. 2018). This method allows almost real time monitoring with sub-millimeter precision. Another advantage is that no targets need to be installed, as in geodetic methods.

Deformations detected using GB-InSAR are in the LoS of the sensor, resulting in the projection of 3D deformations into 1D (Ogundare 2015, Scaioni et al. 2018). Atmospheric effects pose a limitation to this method, as variations in relative humidity affect the measurements obtained from the systems (Scaioni et al. 2018).

Satellite gravimetry and altimetry are other remote sensing techniques used in deformation monitoring and analysis. These techniques are discussed in the following section.

Satellite Gravimetry

Satellite gravimetry involves measuring the Earth's gravitational field using dedicated satellite missions equipped with sensitive instruments (Chen 2019, Chen et al. 2022, Zulkifli et al. 2018). These satellites can detect small changes in the gravitational field caused by mass redestribution within the Earth system. This can be as a result of changes in the distribution of water, ice and solid Earth material.

By analysing the data obtained from satellite gravimetry, it is possible to infer information about deformations occurring in the Earth's crust, such as subsidence, uplift, and horizontal displacements (Chen et al. 2022). These measurements can be particularly useful for monitoring tectonic activity, volcanic eruptions, and the movement of glaciers and ice sheets (Chen 2019).

Satellite gravimetry provides a comprehensive and global view of the Earth's deformations, allowing scientists to monitor large-scale processes and study their long-term behaviour. It complements other deformation monitoring techniques and contributes valuable data for understanding geological phenomena and assessing associated hazards (Chen et al. 2022, Zulkifli et al. 2018).

As an example of the application of satellite gravimetry in deformation monitoring and analysis, variations in GRACE/GRACE-FO Equivalent Water Thickness (EWT) data was processed to probe areas in Kenya that may exhibit high deformation rates through variations in EWT. The analysis focused on eleven three-degree by three-degree mascon grids covering Kenya, as shown in Figure 7.

Among the eleven mascon grids studied, grid 1, 2, 3, 5, and 6 exhibited the most pronounced variations in EWT and hence deformation, with annual trends of 9.3 mm/yr, 11.0 mm/yr, 11.3 mm/yr, 9.3 mm/yr, and 9.0 mm/yr respectively. These grids were identified as areas of possible pronounced deformation rates, characterised by an overall subsidence trend. Deformation in the up component supports the aformentioned hypothesis as all the points exhibit defomation rates of -0.5 mm/yr as illustrated in Figure 8. The analysis of EWT data revealed a clear correlation between the computed mass functional and surface deformation in the up component. Higher variations in EWT were consistently associated with greater deformation values and vice versa. This suggests that regions with significant changes in EWT are experiencing vertical movements in the Earth's crust, which can have implications for geological hazards and hydrological processes.

The study area was selected within mascon grid 6, strategically chosen to investigate potential subsidence or uplift in the region. The observed mass variation in the other grids may be attributed to tectonic processes, particularly in the Kenyan Rift valley, which is known for its geological activity.

To ensure a continuous and comprehensive analysis, interpolation was conducted to fill in the approximate six-month gap between the decommissioning of the GRACE satellite and the commissioning of GRACE-FO. This enabled the creation of a seamless dataset, allowing for a more accurate assessment of the temporal variations in EWT and associated deformation rates.

Results obtained contribute valuable insights into the surface deformation and water mass distribution in Kenya. The identification of areas with high deformation rates through GRACE/GRACE-FO data highlights the significance of continuous satellite monitoring for understanding deformation and hydrological processes in Kenya.

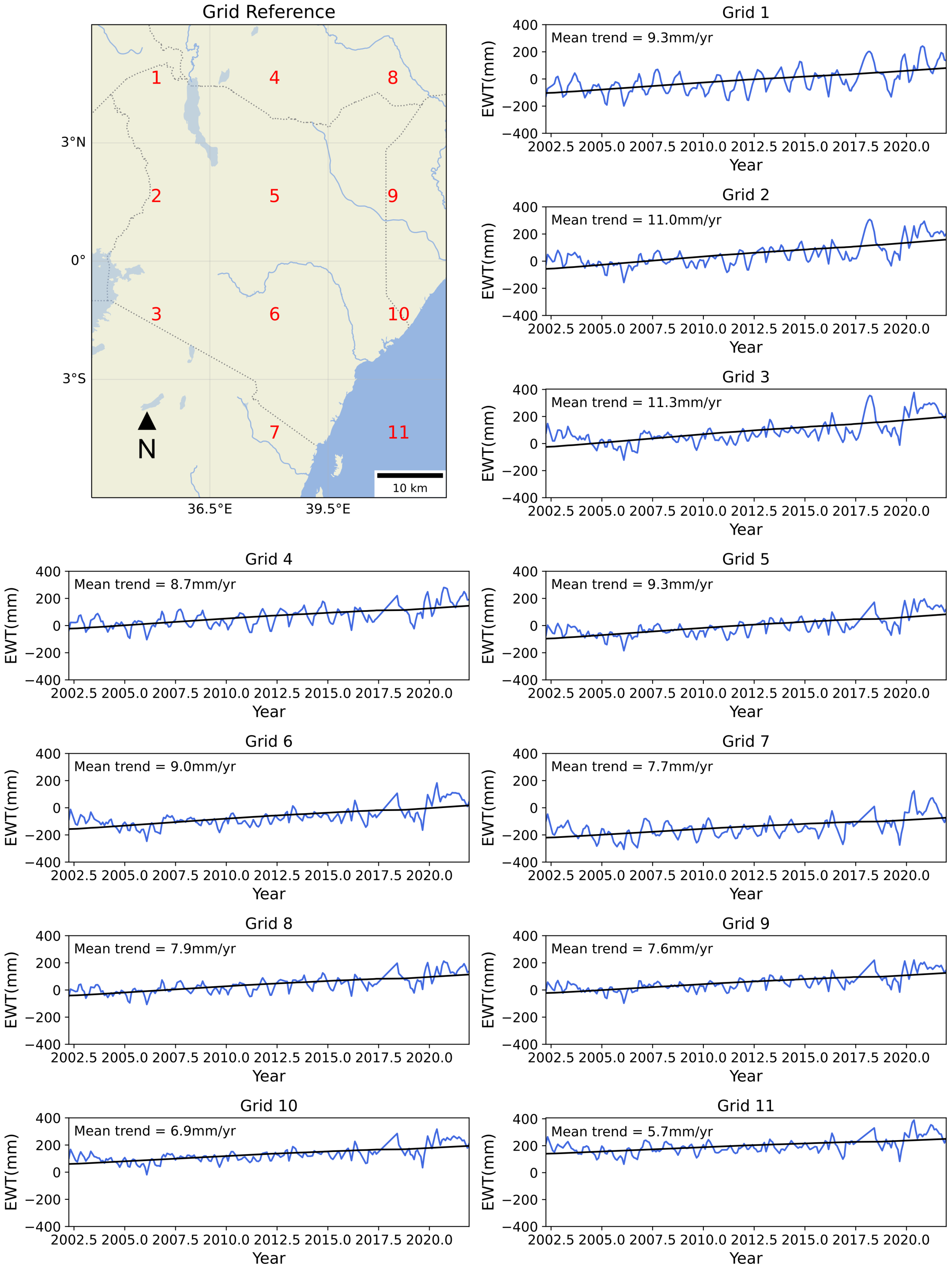

Figure 7: Variation in the Equivalent Water Thickness in Kenya

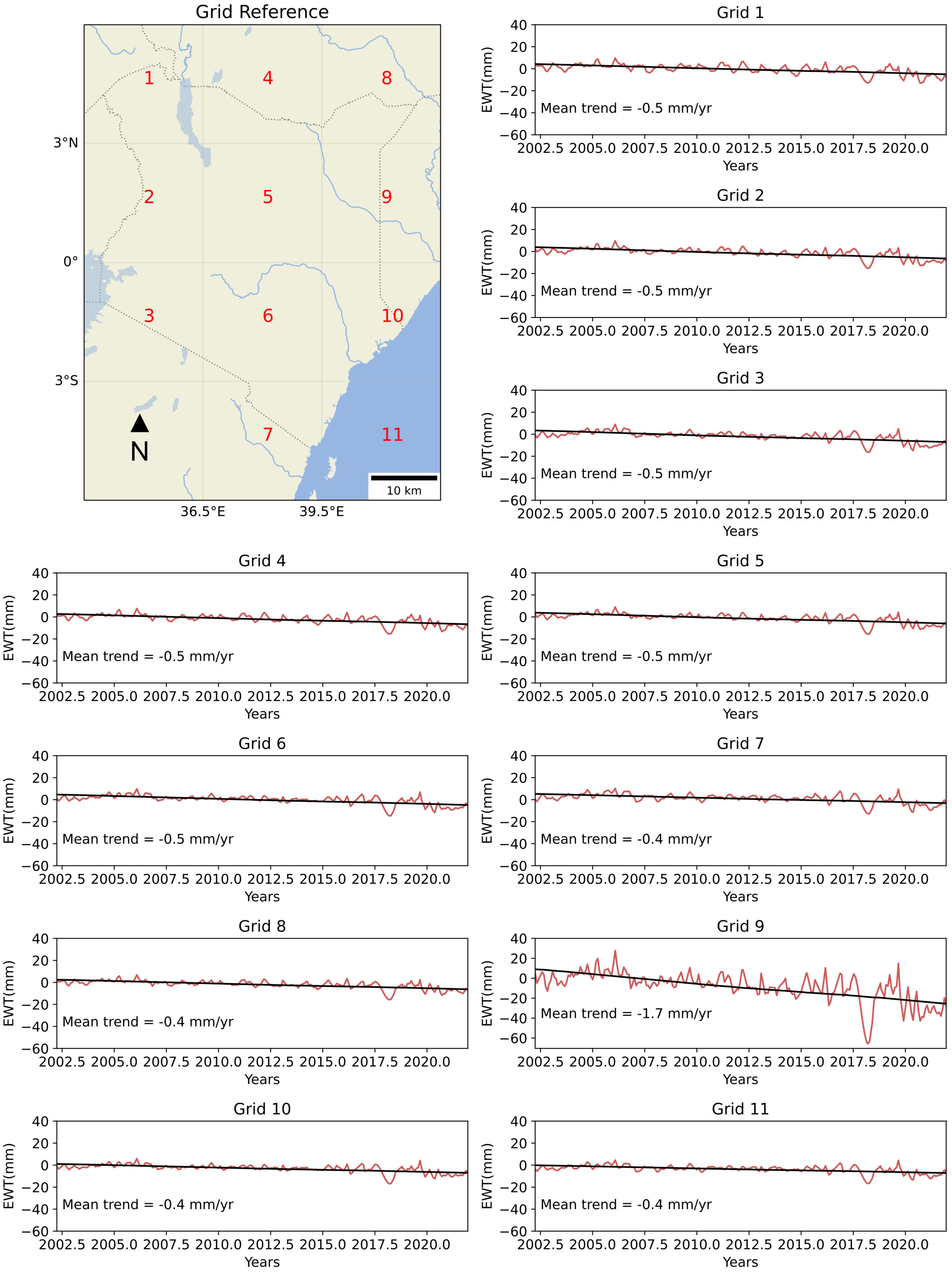

Figure 8: Variation in the surface deformation in Kenya

Satellite Altimetry

Satellite altimetry can be used in deformation monitoring to some extent, although it is not the primary technique employed for this purpose. Satellite altimetry primarily focuses on measuring variations in the height of the Earth's surface, particularly the ocean surface, with high accuracy (Grgić & Bašić 2021, Zulkifli et al. 2018). It is widely used to monitor sea level changes, ocean currents, and the topography of ice sheets and the sea floor.

Satellite altimetry can be used in deformation monitoring to detect large scale vertical displacements, primarily in areas close to water bodies (Grgić & Bašić 2021, Zulkifli et al. 2018). However, it has limitations for precise and localised deformation monitoring. Its spatial resolution is generally too coarse for capturing small scale deformations, and it is more suitable for long-term monitoring rather than immediate changes (Grgić & Bašić 2021). Factors like atmospheric conditions and instrument errors can introduce uncertainties in the data. While satellite altimetry provides valuable insights into vertical displacements, it is not the primary technique used for land based deformation monitoring, which typically relies on GNSS, InSAR, and terrestrial measurements for more accurate and localised results (Grgić & Bašić 2021, Hwang et al. 2016).

2.5.4 Geotechnical and Structural Sensors

Geotechnical and structural sensors are commonly used to measure various quantities such as deformation, load, stress, and groundwater pressure (Ogundare 2015). These sensors provide discrete information similar to geodetic sensors. However, they have limitations compared to geodetic techniques, as they do not provide a global deformation trend of the monitored structure. Additionally, geotechnical and structural sensors are often expensive to install and maintain.

Here is an overview of some geotechnical and structural sensors:

Extensometers - These instruments measure the extension between pairs of points in a deformable structure over time, providing relative deformations (Ogundare 2015).

Four-Pin Gauges - Four-pin gauges are used to measure 3D deformations of a crack's border in relation to the other border (Ogundare 2015).

Joint Meters - Similar to four-pin gauges, joint meters are used to measure the deformation of cracks or joints.

Plumb Lines - Plumb lines serve as a reference for the vertical plane and are used to determine deviations from this vertical reference line. They can be used to measure deformation in the horizontal plane (Erol et al. 2004). Deviations in the vertical plane are referred to as inclination, while deviations in the horizontal plane are called tilt (Ogundare 2015).

Inclinometers - Inclinometers act as probes to determine subsurface displacement, specifically measuring inclination along the vertical plane of a borehole

(Ogundare 2015).

These geotechnical and structural sensors play a crucial role in monitoring the behaviour and deformation of structures. However, it's important to consider their limitations and the specific requirements of each monitoring scenario.

2.5.5 Hydrological Modelling

Hydrological modeling can be used as a valuable tool in deformation monitoring and analysis, particularly in relation to the assessment of groundwater dynamics and their potential influence on deformation processes. Hydrological models simulate the movement and distribution of water within a hydrological system, including surface water, groundwater, and interactions with the atmosphere (Ajami 2021, Xue et al. 2021).

Hydrological modeling plays a crucial role in deformation monitoring and analysis, particularly for assessing groundwater dynamics and their impact on deformation (Li et al. 2017, Xue et al. 2021). It enables the simulation of groundwater flow, changes in storage, and their influence on subsurface stress distribution (Ajami 2021) Hydrological models also help identify areas prone to land subsidence due to excessive groundwater extraction. Additionally, these models assist in evaluating surface water induced deformation caused by water loading effects (Li et al. 2017). Integrating hydrological models with geodetic measurements and ground based sensors improves our understanding of deformation mechanisms and aids in hazard assessment, groundwater management, and infrastructure planning (Li et al. 2017, Xue et al. 2021).

2.6 Review of previous studies

Shafiei Joud et al. (2017) conducted a study on the rate of uplift in the Fennoscandia region. The authors used GRACE data in conjunction to historical GPS data of the area. The GPS records used in the study date as far back as August 1996. The analysis of the GPS velocity data was from 150 permanent stations mounted in Sweden, Finland, Norway and Northern Europe that have provided more than 3-year worth of measurements (Shafiei Joud et al. 2017).

The GRACE gravity anomaly data used by Joud et al. span over 13 years. The study utilised spherical harmonic coefficients from three sources. These sources are the Centre for Space Research (CSR) at the University of Austin Texas and the German Research Centre for Geosciences (GFZ) and Centre National d'Etudes Spatiales (CNES) (Shafiei Joud et al. 2017). A Gaussian Filter (GF) and various anisotropic filters were applied to the GFZ and CSR data before the land uplift rate was determined.

The root mean square error (RMSE) of the difference between the uplift data obtained from GPS and GRACE data was then computed. The RMSE for the difference between the GPS data and: CNES data, GFZ data (with applied anisotropic filter), CSR data (with applied anisotropic filter), GFZ (with applied GF), CSR (with applied GF) was 0.88 ± 1.23 mm/yr, 2.03 ± 0.94 mm/yr, 0.77 ± 0.67 mm/yr, 2.02 ± 1.70 mm/yr and 0.28 ± 1.62 mm/yr respectively (Shafiei Joud et al. 2017).

Steckler et al. (2010) modelled the deformation due to seasonal monsoonal flooding of the Ganges-Brahmaputra delta in Bangladesh. GRACE, GPS and hydrographic data was utilised in modelling the deformation in this study. Daily data from 18 Continually Operating Reference Stations (CORS) were processed to determine the deformation rate. Time series of monthly GRACE data that was regularised to spherical harmonic degree 120, was used in the study.

The last dataset utilised in this study was data from 304 river gauge obtained from the Bangladesh water development board (Steckler et al. 2010). The gauge data was from January 2003 to December 2007. The authors determined the water load on the Earth's surface in Bangladesh by using a fitted gridded surface using the river gauge data for the study period. The computed load was compared to GRACE monthly estimates. The data was consistent within statistical limits (Steckler et al. 2010). The GPS data displayed seasonal variations of up to 6 cm.

Yang et al. (2019) determined the deformation in Central Taiwan as a result of seasonal ground water extraction. The authors used Sentinel-1A InSAR analysis using the Small Baseline Subset Method (SBAS). 14 CORS were used to calibrate the initial InSAR result while 406 levelling benchmarks were used to validate the final calibrated InSAR result (Yang et al. 2019). The authors also compared the wet and dry season rate of surface displacement. The study ascertained that the results obtained from both GPS and InSAR processing were similar with some outliers. The calibrated InSAR data did seem to agree with the levelling data with a difference of only 2.6% (Yang et al. 2019). The dry season contributed to about 60-74% of the surface deformation due to ground water extraction.

Gido et al. (2020) determined localised zones of subsidence in Gävel city in Sweden. The authors' processing used Persistent Scatter Interferometry (PSI) as well as historic levelling data to identify significant subsidence zones in the city. Sentinel-1 datasets were obtained from January 2015 to May 2020 and used in processing. The levelling records used in the study covered the period from 1974 to 2019 (Gido et al. 2020).

The underlying geology of various parts of the city was also considered in relation to the deformation rates obtained from both PSI and levelling data analysis. The centre of the city was determined to be stable with deformations rates of – 2 ± 0.5 mm/yr and 2 ± 0.5 mm/yr, in the vertical and East-West directions respectively (Gido, et al., 2020). A higher rate of subsidence was detected in the North-East section of the city with a deformation rate of – 6 ± 0.46 mm/yr. The common points between the PSI and levelling data analysis revealed an agreement between the detected rates of deformations (Gido et al. 2020)

Njiraini et al. (2022) explored the triggers of landslides in Murang'a county through indigineous knowledge collected from primary data through household questionnaires, key informant interviews, and focus group discussions. A total of 336 household questionnaires were successfully completed and returned, with an average response rate of 86% (Njiraini et al. 2022). The questionnaires included both structured and open ended questions related to the understanding of landslide causal and trigger factors. The respondents for the questionnaires were the heads of each household or any other person above 18 years of age in cases where the head was unavailable.

In addition to the household questionnaires, 8 key informant interviews and 7 focus group discussions were conducted. Key informants were individuals with knowledge of indigenous people's understanding of landslide causal and trigger factors. The focus group discussions involved small cohorts of the population focusing on specific areas of study to yield valuable information (Njiraini et al. 2022).

Njiraini et al. (2022)'s findings revealed that indigenous people understood the factors causing or triggering landslides and their contribution to landslide occurrences. The identified factors were rainfall, elevation, slope, soils, land-use land-cover, vegetation cover, infrastructural development, and population. These factors were considered to have a significant degree of causality in landslides.

2.7 Review of Satellites used in study

2.7.1 Sentinel-1 Mission

The Sentinel-1 mission stands as a cornerstone within the Copernicus program, a collaborative effort spearheaded by the European Commission (EC) and the European Space Agency (ESA) (EoPortal 2023, Potin et al. 2016). This mission is exemplified by the deployment of two identical satellites, Sentinel-1A and Sentinel-1B, both launched in April 2014 and April 2016, respectively (EoPortal 2023, Potin et al. 2016). Representing a critical component of the Earth observation initiative, Sentinel-1 is tailored for all weather, day and night observations, with a particular emphasis on RADAR imaging capabilities (EoPortal 2023, Potin et al. 2016, Torres et al. 2012). This strategic deployment ensures continuity and long term data acquisition for Earth observation, positioning it as a linchpin for a multitude of scientific, environmental, and societal applications (EoPortal 2023).

The European Space Agency shoulders the responsibility for managing and operating the Sentinel-1 mission comprehensively (EoPortal 2023, Potin et al. 2016). This spans the entire spectrum of activities, from technical design, satellite construction, and launch, to mission control and data management. In parallel, the European Commission assumes the overarching stewardship of the Copernicus program, of which the Sentinel missions are integral components (EoPortal 2023, Potin et al. 2016). This holistic approach is geared towards providing open, free, and timely access to Earth observation data, fostering a diverse array of applications across industries and disciplines.

The versatility of the Sentinel-1 mission is epitomised by its radar sensor, which operates across various data acquisition modes to meet diverse user requirements and optimise efficiency in data collection. The Interferometric Wide Swath (IW) mode is designed for large scale mapping and monitoring applications, covering expansive areas with a swath width of up to 250 km (EoPortal 2023, Potin et al. 2016, Torres et al. 2012). The Extra Wide Swath (EW) mode extends this capability with a swath width of up to 400 km, facilitating rapid coverage of extensive regions—particularly beneficial for emergency response and disaster monitoring scenarios (EoPortal 2023). In Stripmap (SM) mode, the RADAR narrows its focus, acquiring higher resolution images tailored for detailed imaging of smaller areas (EoPortal 2023, Torres et al. 2012). Furthermore, the Wave (WV) mode is specifically engineered for monitoring ocean and coastal areas, contributing critical data for the study of waves, currents, and marine activities (Torres et al. 2012). Figure 9 depicts the various acquisition modes of Sentinel-1 and their corresponding characteristics.

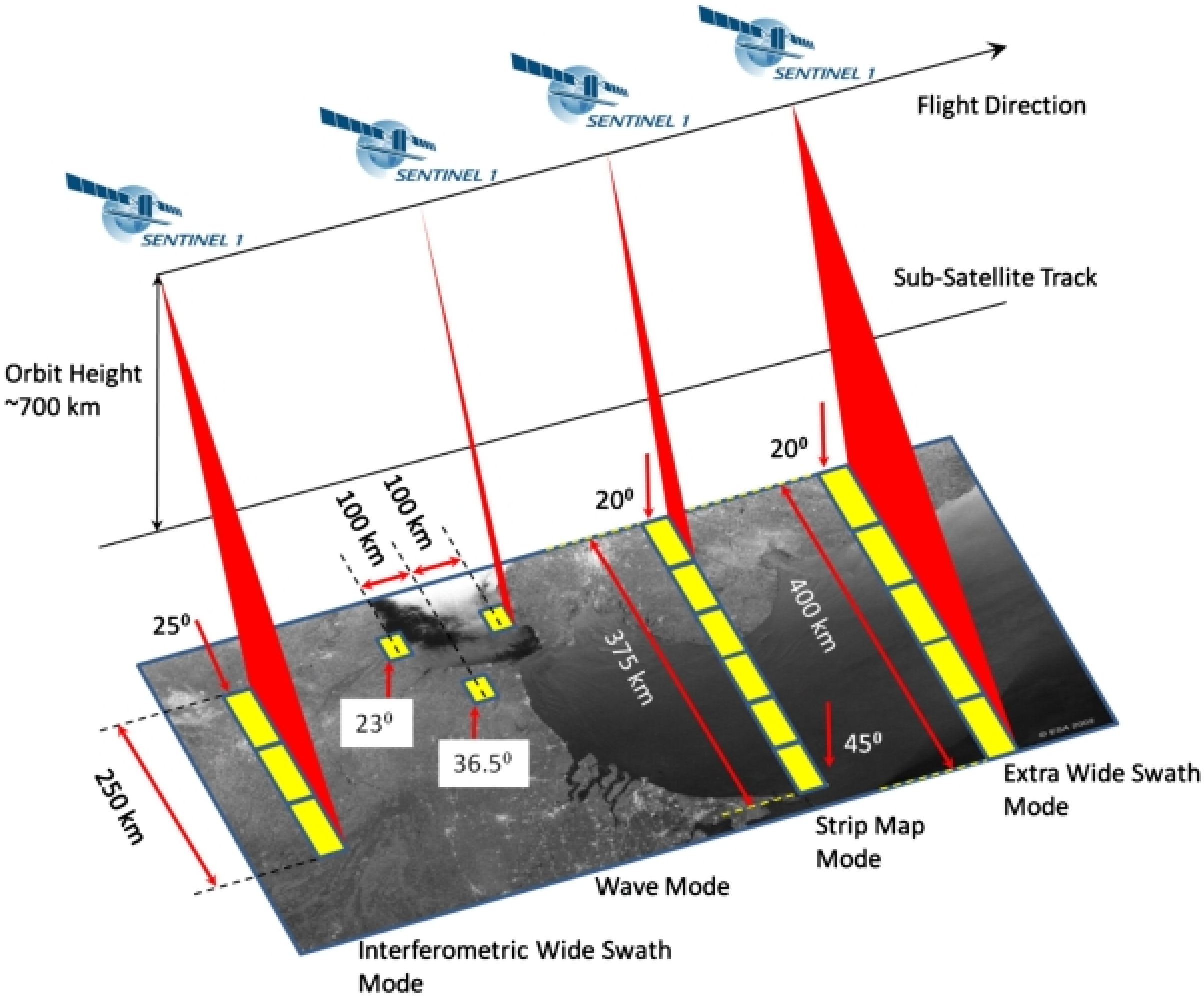

Figure 9: Sentinel-1 acquisition modes and their corresponding attributes. Adapted from: (Torres et al. 2012)

The Sentinel-1 satellites are equipped to capture RADAR data in dual polarisation mode, incorporating both horizontal (HH) and vertical (VV) polarisation for all acquisition modes (EoPortal 2023, Potin et al. 2016, Torres et al. 2012). This dual polarisation capability broadens the spectrum of applications, encompassing agriculture, forestry, land subsidence monitoring, and disaster management (EoPortal 2023). The Sentinel-1 mission's global coverage, coupled with its frequent revisit times and commitment to an open data policy, has positioned it as an invaluable asset for numerous scientific, environmental, and societal applications (EoPortal 2023). The continuous flow of high quality RADAR images facilitates a deep understanding and monitoring of Earth's dynamic processes, significantly contributing to the advancement of our knowledge of the planet and supporting decision making processes across diverse sectors.

2.7.2 ALOS PALSAR Mission

The Advanced Land Observation Satellite Phase Array type L-band Synthetic Aperture RADAR (ALOS PALSAR) mission, integral to the ALOS program spearheaded by the Japan Aerospace Exploration Agency (JAXA), embarked on its mission on January 24, 2006, marking a significant chapter in Japanese Earth observation (Shimoda & Kimura 2018). This satellite, which operated tirelessly for approximately five years until April 2011, played a pivotal role in advancing our capabilities for high resolution radar imagery with diverse applications, ranging from disaster monitoring to environmental assessment and natural resource management.

The primary thrust of the ALOS PALSAR mission was to provide a wealth of high resolution radar imagery to meet a spectrum of observational needs (Shimoda & Kimura 2018). Operating in multiple modes, the satellite demonstrated versatility in capturing data for different applications. The Fine Beam Single Polarity (FBS) mode and the Fine Beam Dual Polarity (FBD) mode were tailored to deliver high resolution single and dual-polarisation imagery, respectively (Rosenqvist et al. 2004, Shimoda & Kimura 2018). These modes were particularly suited for detailed land cover classification and change detection, providing crucial insights into the dynamics of Earth's surface (Shimoda & Kimura 2018).

Adding to its repertoire, the ScanSAR mode exhibited the capability to cover wider areas, a functionality highly valuable for regional mapping and disaster monitoring (Shimoda & Kimura 2018). This operational mode allowed for a broader perspective, facilitating a comprehensive understanding of large scale environmental changes and natural disasters. Meanwhile, the Polarimetric mode, another feature of the ALOS PALSAR mission, enriched the mission's offerings by providing multi-polarization data (Rosenqvist et al. 2004). This capability was instrumental in studying scattering mechanisms and land surface properties, contributing to advancements in our understanding of Earth's diverse landscapes.

The ALOS PALSAR mission significantly contributed to global Earth observation endeavors and scientific research throughout its operational tenure. The rich repository of RADAR data it provided has left an indelible mark on various fields, from environmental sciences and disaster management to geology and forestry (Shimoda & Kimura 2018). The mission's legacy lies not only in the wealth of data it produced but also in its role as a pioneering endeavor that pushed the boundaries of RADAR imaging technology. The mission's multifaceted modes of observation, coupled with its dedication to delivering high-resolution and polarimetric data, underscore its importance as a valuable asset in the realm of Earth observation.

2.7.3 LandSat Mission

The Landsat program stands as an enduring testament to the success and longevity of Earth observation satellite missions, jointly managed by the United States Geological Survey (USGS) and the National Aeronautics and Space Administration (NASA) (USGS n.d.b, Wulder et al. 2019). Launched with the primary objective of providing a continuous and comprehensive record of global land surface observations, the program has evolved since the inauguration of its inaugural satellite, Landsat 1, on July 23, 1972 (USGS n.d.b). Over the decades, the Landsat program has seen the deployment of multiple satellites, each equipped with increasingly advanced sensors and capabilities, marking significant milestones in the field of Earth observation (Wulder et al. 2019).

The genesis of the Landsat program was the launch of Landsat 1, a historic event that marked the initiation of the first civilian Earth observation satellite dedicated explicitly to monitoring land resources (USGS n.d.b). The subsequent missions, including Landsat 2 (1975), Landsat 3 (1978), Landsat 4 (1982), Landsat 5 (1984), and Landsat 7 (1999), represented successive advancements, with each satellite incorporating improved sensors and technological capabilities (Wulder et al. 2019). While Landsat 6 faced the unfortunate setback of failing to achieve orbit in 1993, the subsequent missions, Landsat 8 (2013) and Landsat 9 (2021), continued the legacy of the program, ensuring the continuity of high quality Earth observation data (Wulder et al. 2019). Figure 10 show the evolution and timeline of the LandSat mission and satellites.

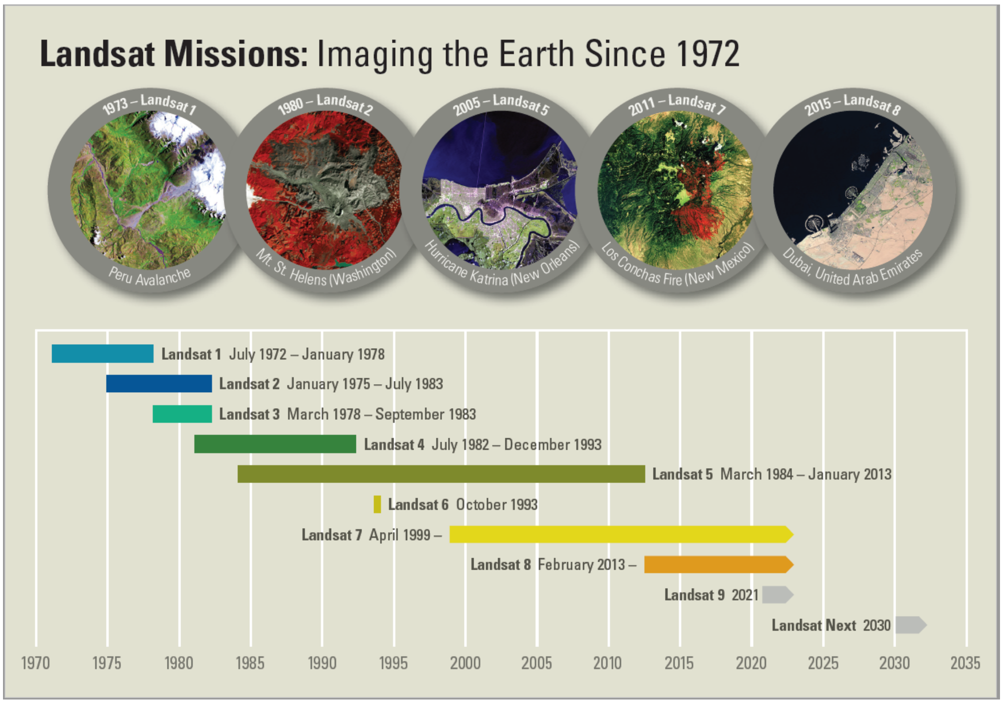

Figure 10: The evolution of the LandSat mission and the timelines of the satellites. Adapted from: (USGS n.d.b)

Orbiting the Earth in a sun-synchronous polar orbit, Landsat satellites collectively form a vanguard that comprehensively images the entire Earth's surface over a 16-day repeat cycle (USGS n.d.b, Wulder et al. 2019). This strategic orbiting pattern enables consistent and systematic coverage, providing a wealth of multispectral and multitemporal imagery. The sensors on Landsat satellites are designed to capture data across various spectral bands, encompassing visible, near-infrared, short-wave infrared, and thermal infrared regions (USGS n.d.b, Wulder et al. 2019). This multispectral capability empowers scientists and researchers to delve into a myriad of studies, including changes in vegetation, land cover, water bodies, urban areas, and natural resources over time.

The significance of Landsat extends beyond the sheer volume of data it collects; it lies in its role as a foundational resource for global Earth observation (Wulder et al. 2019). The continuous, decades-long dataset created by Landsat facilitates a profound understanding of dynamic Earth processes and ecosystems. This wealth of information has become an invaluable asset for addressing critical environmental and societal challenges, from monitoring deforestation and urban expansion to managing water resources and assessing the impacts of climate change.

2.7.4 GRACE/GRACE-FO Mission

The Gravity Recovery and Climate Experiment (GRACE) and its successor, the Gravity Recovery and Climate Experiment Follow-On (GRACE-FO), represent pioneering missions in the study of Earth's gravity field and its dynamic variations over time (Chen et al. 2022, Chen 2019, Wouters et al. 2014). These joint ventures between NASA and the German Aerospace Center (DLR) have significantly contributed to our understanding of global water distribution, ice melting, and other mass movements, offering crucial insights into Earth's changing climate (Wouters et al. 2014).

The GRACE mission marked its initiation with the launch of two identical satellites, GRACE-1 and GRACE-2, on March 17, 2002 (Chen et al. 2022, Chen 2019, Wouters et al. 2014). These satellites were strategically positioned in a polar, low Earth orbit, forming a tandem mission that revolutionised the field of Earth observation. The primary objective of GRACE was to precisely measure variations in Earth's gravity field, and in doing so, unravel the complex dynamics of water movement across the planet (Chen 2019).

The mechanism employed by GRACE was elegant in its simplicity yet groundbreaking in its potential impact. The twin satellites, separated by a precise distance, essentially acted as a highly sensitive gravitational sensor (Chen et al. 2022, Chen 2019, Wouters et al. 2014). As they orbited the Earth, variations in the gravitational pull caused minute changes in the distance between them (Wouters et al. 2014). By precisely measuring these changes, using the High Accuracy Inter-satellite Ranging System (HAIRS) on board the satellites, scientists could construct detailed maps of Earth's gravity field, offering a dynamic and comprehensive view of how mass is distributed across the globe. Figure 11 illustartes the operational principle of GRACE/GRACE-FO satellites.

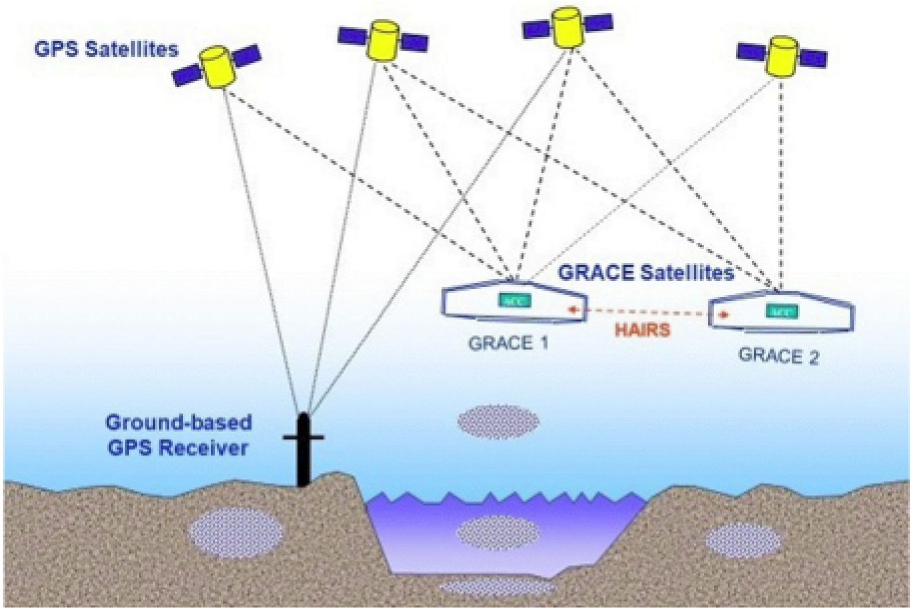

Figure 11: An infographic of GRACE Satellites and their operational principle. Adapted from: (Flechtner et al. 2021)

The applications of GRACE data extended across diverse domains. One of the key contributions was in the realm of hydrology, where GRACE data provided critical information about the distribution of water, tracking variations in underground aquifers, soil moisture, and surface water bodies (Chen et al. 2022). In addition, GRACE played a crucial role in monitoring the mass balance of ice sheets and glaciers, offering insights into the contribution of melting ice to sea-level rise (Chen 2019).

Despite the resounding success of GRACE, its mission concluded after nearly 15 years of operation. However, recognizing the immense scientific value and the need for continued observations, the GRACE Follow-On (GRACE-FO) mission was initiated (Chen et al. 2022). Launched on May 22, 2018, GRACE-FO mirrors its predecessor in design and purpose. The mission comprises two identical satellites, continuing the tandem approach that proved so effective in the original GRACE mission. The goal remains consistent—to observe and quantify variations in Earth's gravity field with exceptional precision (Chen et al. 2022).

GRACE-FO, like its predecessor, employs the same fundamental principle of satellite-to-satellite ranging (Chen et al. 2022). The continuity provided by GRACE-FO is crucial for building on the legacy of GRACE and extending the gravity field data record. This extended dataset is invaluable for understanding long-term trends, particularly in the context of climate change and its implications for Earth's water resources and sea-level dynamics.

Chapter 3

Research Design and Methodology

Within this thesis, a comprehensive inquiry into the mechanisms governing deformation induced by landslides within our specified study area is conducted. The research design and methodology herein are structured to systematically unravel the multifaceted interactions influencing these processes. A central guiding element is the data flow diagram as seen in Figure 12, delineating the flow of information to distinct analytical nodes.

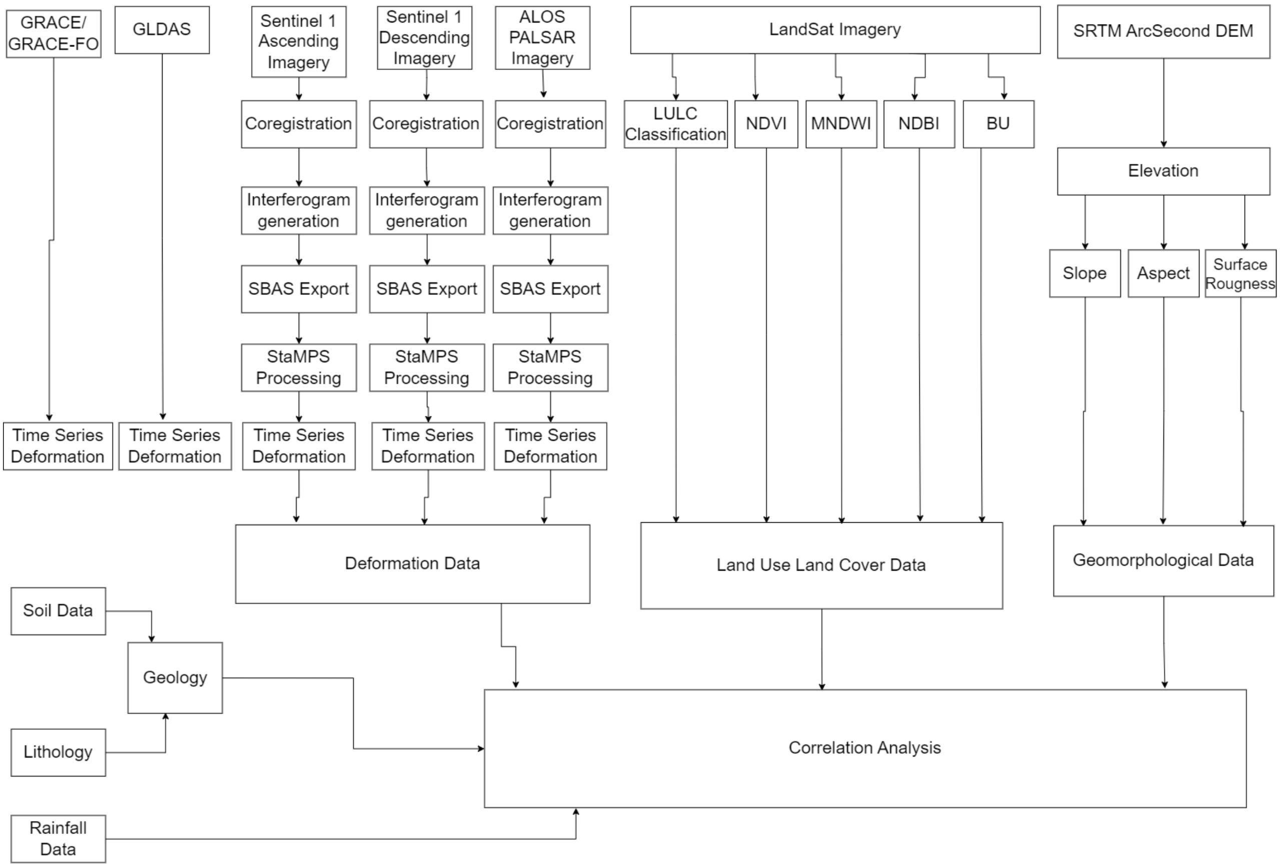

Figure 12: The Research design Methodology flow diagram

This visual representation serves as a methodical roadmap, expounding on the sequential processing of data, commencing from satellite-based observations and hydrological modelling to the extraction of crucial geomorphological and land cover parameters. The accompanying Table 2 systematically catalogues the heterogeneous datasets pivotal to this research, enumerating their respective sources. Subsequent sections expound upon the intricacies of the research design and the deployment of diverse methodologies, underscoring the synergistic integration of satellite data, hydrological models, and geospatial analyses to advance the scientific understanding of these intricate geomorphic phenomena.

Table 2: Datasets used in this research and their corresponding sources

Dataset	**Source**	**Citation**
GRACE/GRACE-FO	ICGEM	(Ince et al. 2019)
GLDAS	GIOVANNI	(Li et al. 2019)
Sentinel-1	ASF DAAC	(ASF DACC n.d.)
ALOS PALSAR	ASF DAAC	(JAXA/METI n.d.)
LandSat	USGS	(USGS n.d.a)
SRTM ArcSecond DEM	OpenTopography	(Farr & Kobrick 2000)
Soil	ICPAC Geoportal	(ICPAC 2017)
Lithology	IGRAC	(Africa Groundwater Atlas 2019)
Rainfall	TAMSAT	(Maidment et al. 2017, Maidment et al. 2014, Tarnavsky et al. 2014)

3.1 GRACE Data Processing

The methodology for analysing the Earth's gravity field variations and computing different mass functionals relies on data downloaded from the International Center for Global Gravity Field Models (ICEGEM). Specifically, spherical harmonic data from both the GRACE and GRACE-FO missions were obtained from ICEGEM. Monthly solutions for German Research Centre for Geosciences (GFZ) Release 05 and Release 06 were utilised in the analysis. The spherical harmonic data provided crucial information about the Earth's gravity field through the examination of variations in mass distribution over time. By combining data from different GRACE and GRACE-FO releases, various mass functionals that provided insights into changes in regional water storage and hence the elastic deformation of the earth's surface were computed. The use of ICEGEM data ensures the reliability and accuracy of the conducted analysis, contributing to the robustness of the results presented in this thesis.

The computation and analysis of the gravity/mass functionals were carried out using the MATLAB package IGiK-TVGMF developed by Godah (2019). This software package is specifically designed for processing and interpreting spherical harmonic data from gravity missions like GRACE and GRACE-FO. The IGiK-TVGMF package efficiently handles the complex data provided by ICEGEM, allowing for the extraction of relevant gravity/mass functionals. The software's robust algorithms and functionalities enabled the computation of quantities such as the Equivalent Water Thickness (EWT), which provided valuable insights into variations in Earth's water storage. Additionally, the IGiK-TVGMF package facilitated the analysis of other mass-related phenomena, such as solid Earth deformations.

Variations in two essential mass functionals were chosen to investigate specific Earth processes: Equivalent Water Thickness, ΔEWT and surface deformation in the up component, Δh. The formulation of both functionals are given in Equations 1 and 2. EWT provides crucial information about changes in global water storage, including variations in surface water, groundwater, and soil moisture. Surface deformation in the up component allows for the study of vertical ground movements, such as subsidence or uplift, which are indicative of tectonic activities or changes in mass distribution. The formulas used to compute EWT and surface deformation in the up component were based on the methodology presented in Godah (2019), where the relationships between spherical harmonic coefficients and gravity/mass functionals are thoroughly described. The implementation of these formulas, alongside other gravity/mass functional formulas, ensured the accuracy and consistency of our analysis. For detailed formulas and further references, interested readers can refer to Godah (2019), which served as a fundamental resource for this research.

$$\Delta EWT_{(r,\phi,\lambda)} = \frac{a \times \rho_{ave}}{3} \sum_{n=0}^{n_{max}} \sum_{m=0}^{n} P_{nm}(\sin\phi) \frac{2n\ +\ 1}{1\ +\ k_n} [\Delta C^{T}_{nm} \cos m\lambda\ +\ \Delta S^{T}_{nm} \sin m\lambda] \tag{1}$$

$$\Delta h_{(r,\phi,\lambda)} = \frac{3 \times a \times \rho_w}{\rho_{ave}} \sum_{n=0}^{n_{max}} \sum_{m=0}^{n} P_{nm}(\sin\phi) \frac{h}{2n+1} [\Delta C^{\delta}_{nm} \cos m\lambda\ +\ \Delta S^{\delta}_{nm} \sin m\lambda] \tag{2}$$

$$\Delta C^{T}_{nm} = C^{W(GRACE)}_{nm}\ -\ C^{U(GRACE)}_{nm}\ -\ (C^{W(EGM2008)}_{nm}\ -\ C^{U(EGM2008)}_{nm}) \tag{3}$$

$$\begin{Bmatrix} \Delta C^{\sigma}_{nm} \\ \Delta S^{\sigma}_{nm} \end{Bmatrix} = \frac{\rho_{ave} \times 2n\ +\ 1}{3 \times \rho_w \times\ +\ k_n} \begin{Bmatrix} \Delta C^{T}_{nm} \\ \Delta S^{T}_{nm} \end{Bmatrix} \tag{4}$$

Where:

a represents the equitorial radius/semi-major axis length of the ellipsoid

ρ_{ave} represents the average density of the Earth's crust

ρ_w represents water density

C^{W}_{nm}, S^{W}_{nm} represent normalised spherical harmonic coefficients of degree n and order m

C^{T}_{nm}, S^{T}_{nm} represents topographic potential spherical harmonic coefficients of degree n and order m

$C^{\sigma}_{nm}, S^{\sigma}_{nm}$ represent surface density spherical harmonic coefficients of degree n and order m

h_n, k_n represent load love numbers of degree n

3.2 Hydrological Data Processing

The Global Land Data Assimilation System (GLDAS) Catchment Land Surface Model (CLSM) L4 daily 0.25 x 0.25 degree GRACE-Data Assimmilation (DA1) V2.2 was another tool employed for determining elastic deformation of the Earth's crust in the study area. The GLDAS CLSM is an integrated land surface model that combines satellite and ground based observational data with advanced numerical techniques to simulate land surface processes at a global scale. Specifically, the model incorporates data from the Global Land Data Assimilation System (GLDAS), which includes satellite remote sensing data, weather station measurements, and atmospheric data from numerical weather prediction models (Li et al. 2019).

By assimilating these diverse set of inputs, the GLDAS CLSM generates comprehensive and accurate land surface datasets, such as soil moisture, temperature, and snowpack, which are crucial for studying Earth's surface deformation. Additionally, the incorporation of GRACE data, with its precise measurements of gravity field changes, further enhances the model's ability to estimate elastic deformation of the Earth's crust. Equation 5 leverages the synergy between GLDAS CLSM and GRACE data, enabling the derivation of valuable insights into variations in crustal deformation, $\Delta L(\tilde{r})$. The GLDAS CLSM is managed and maintained by a collaborative effort involving organisations such as NASA's Goddard Space Flight Center, the National Centers for Environmental Prediction (NCEP), the Hydrological Sciences Laboratory (HSL), and the Global Modeling and Assimilation Office (GMAO).

$$L(\tilde{r}) = \rho_w \iint G(|\tilde{r} - r'|).\Delta EWT(r').dA \tag{5}$$

G represents the integrated Green's function as presented in Farrell (1972)'s work. The Green's function is evaluated between a reference point $\tilde{r}$ and the load application point r'.

The integrated Green's function can be simplified as (Farrell 1972):

$$G_{u_r} = \frac{R}{M} h_{\infty} \sum_{n=0}^{\infty} P_n(\cos\theta) + \frac{R}{M} \sum_{n=0}^{\infty} (h_n - h_{\infty}) P_n(\cos\theta) \tag{6}$$

Where:

θ represents angular distance from point mass load

M represents the Earth's mass

R represents the Earth's radius

P_{nm} represents normalised Legendre functions

h_n represents Load love number of degree n

3.3 SBAS Processing

In this study, the Small Baseline Subset (SBAS) method of InSAR processing was utilised to derive line of sight deformation in the study area. Specifically, the modified SBAS method proposed by Hooper (2008) was employed to process the RADAR imagery from three different sensors: Sentinel-1A, Sentinel-1B, and ALOS PALSAR. The modified SBAS method was chosen due to its ability to generate more scatterers with a low signal-to-noise ratio (Hooper 2008). This method also combines both persistent scatterer and small baseline approached used in interferometry (Hooper 2008).

Preprocessing was conducted using the Sentinel Application Platform (SNAP) software (Foumelis et al. 2018) and the SBAS analysis was conducted using the Stanford Method for Persistent Scatterers/Multi-Temporal InSAR (StaMPS/MTI) MATLAB package (Hooper et al. 2012). The Toolbox for Reducing Atmospheric InSAR Noise (TRAIN) (Bekaert et al. 2015a, Bekaert et al. 2015b) was applied in STAMPS processing to mitigate errors induced by atmospheric effects on the signal propagation.

For the Sentinel-1A imagery, data in the ascending acquisition node were used, and the time series analysis was conducted over the period from 22nd October 2017 to 13th November 2021. Conversely, the descending node a mixture of Sentinel-1A and Sentinel-1B imagery was acquired in the descending acquisition node, and the time series analysis covered the period from 15th January 2015 to 21st November 2021. The study area was divided into a single path with two frames each for the Sentinel acquisition nodes. Path 57 and frames 1175 and 1180 for the ascending node and path 79 and frames 592 and 597 for the descending node as shown in Figures 13 and 14.

As for the ALOS PALSAR imagery, data in the ascending acquisition node were employed, and the time series analysis spanned from 2nd July 2007 to 27th July 2010. The study area was divided into two paths, denoted as Path 565 and Path 569, with each path covering three rows (7160, 7170, and 7180) as depicted in Figure 15. All the ALOS PALSAR images used in this analysis were in the ascending node.

For the first path, path 565, the chosen master date was set to the 19th of May 2009. For the second path, path 569, the selected master date was the 8th of September 2009. It is important to note that ALOS PALSAR data is characterised by scarcity, which presented certain limitations in the analysis. To maximise the available data, temporal and perpendicular baselines were extended to as far as 875 days and 2500 metres, respectively.

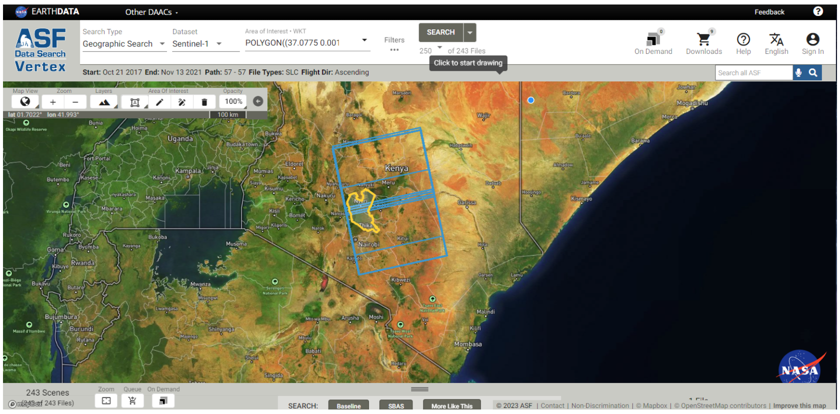

Search Type: Geographic Search
Dataset: Sentinel-1
Area of Interest • WKT: POLYGON((37.0775 0.001
250 of 243 Files
Start: Oct 21 2017 End: Nov 13 2021 Path: 57 - 57 File Types: SLC Flight Dir: Ascending
lat 01.7022° lon 41.993°
243 Scenes (243 of 243 Files)

Figure 13: Sentinel-1 Ascending node image footprints over the study area. Source: Alaska Space Facility (ASF)

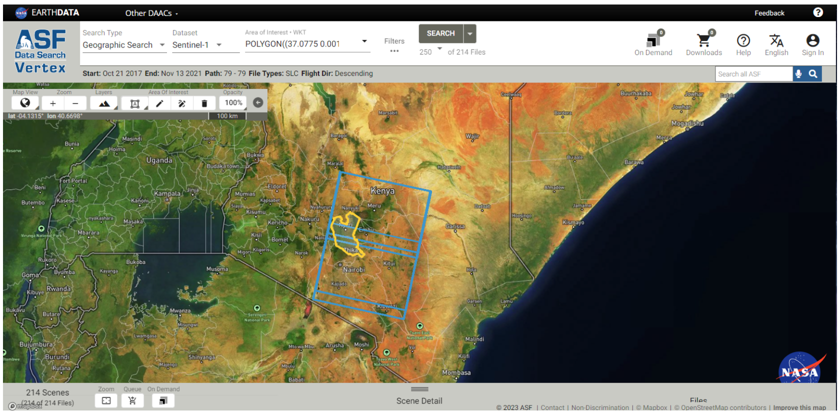

Search Type: Geographic Search
Dataset: Sentinel-1
Area of Interest • WKT: POLYGON((37.0775 0.001
250 of 214 Files
Start: Oct 21 2017 End: Nov 13 2021 Path: 79 - 79 File Types: SLC Flight Dir: Descending
lat -04.1315° lon 40.6698°
214 Scenes (214 of 214 Files)

Figure 14: Sentinel-1 Descending node image footprints over the study area. Source: Alaska Space Facility (ASF)

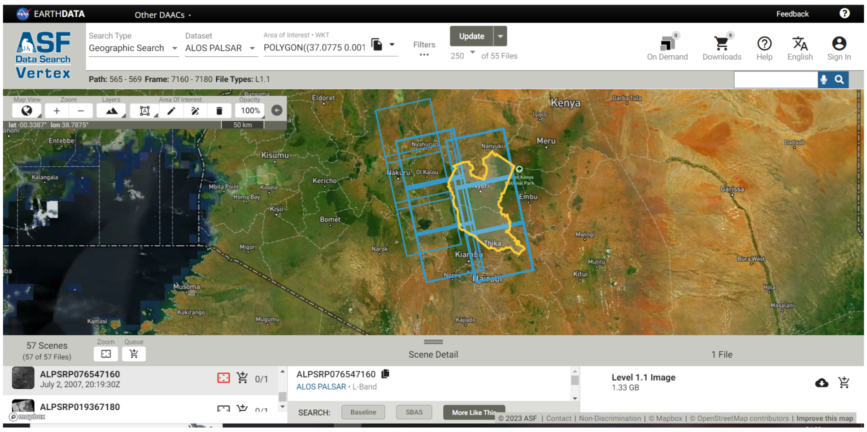

Search Type: Geographic Search
Dataset: ALOS PALSAR
Area of Interest • WKT: POLYGON((37.0775 0.001
250 of 55 Files
Path: 565 - 569 Frame: 7160 - 7180 File Types: L1.1
lat -00.3387° lon 38.7875°
57 Scenes (57 of 57 Files)
ALPSRP076547160 July 2, 2007, 20:19:30Z 0/1
ALPSRP019367180 0/1
ALPSRP076547160
ALOS PALSAR • L-Band
Level 1.1 Image 1.33 GB

Figure 15: ALOS PALSAR Image footprints over the study area. Source: Alaska Space Facility (ASF)

By applying the modified SBAS method to these RADAR datasets, we were able to accurately estimate the line of sight deformation in the study area, providing valuable insights into ground subsidence and related geomorphic phenomena.

SBAS is an advanced technique in InSAR processing that aims to mitigate the temporal decorrelation issues associated with traditional InSAR methods (Gong et al. 2016). In traditional InSAR, coherence between RADAR images acquired at different times can be affected by factors such as vegetation growth, atmospheric disturbances, and temporal changes in the target area. The SBAS method overcomes these limitations by selecting pairs of RADAR images with small temporal baselines, i.e., images acquired close in time, to ensure a higher coherence level (Chang et al. 2022). By carefully choosing a subset of RADAR images with minimal temporal decorrelation, SBAS creates a robust and coherent interferogram stack, allowing for precise and consistent measurements of ground surface deformations over long periods. The interferometric phase of the j-th interferogram, $\delta_{j(x,r)}$, is derived as shown in Equation 7 (Chang et al. 2022, Guo et al. 2016). Initial selection of permanent scatterers depends on amplitude dispersion, $D_{\Delta,A}$, computed as shown in Equation 8 (Hooper 2008, Kirui et al. 2022). The final permanent scatterers are chosen based on their temporal coherence, γ_x, computed as shown in Equation 9 (Hooper 2008, Kirui et al. 2022).

$$\begin{aligned}\delta_{j(x,r)} &= \Phi(t_B, x, r) - \Phi(t_A, x, r) \\ &\approx \Phi_{def,j}(x,r) + \Phi_{atm,j}(x,r) + \Phi_{orb,j} + \Phi_{\Theta,j}(x,r) + \Phi_{noise,j}(x,r)\end{aligned} \tag{7}$$

$$D_{\Delta,A} = \frac{\sqrt{\frac{\sum_{i=1}^{N}(|m_i|-|s_i|)^2}{N}}}{\frac{1}{2N}\sum_{i=1}^{N}|s_i|} = \frac{\delta_{\Delta,A}}{\mu_{\Delta,A}} \tag{8}$$

$$\gamma_x = \frac{1}{N}\left|\sum_{i=1}^{N} \exp\sqrt{-1}(\psi_{x,1} - \tilde{\psi_{x,1}} - \Delta\tilde{\phi}_{\theta,x,i})\right| \tag{9}$$

Where:

Φ represents phase values of SAR images

$\Phi_{def,j}$ represents deformation phase values between times t_B and t_A

$\Phi_{atm,j}$ represents atmospheric phase error

$\Phi_{orb,j}$ represents residual errors due to orbit inaccuracies

$\Phi_{\Theta,j}$ represents the residual phase due to look angle error

$\Phi_{noise,j}$ represents the random noise phase

m_i represents the amplitude of the master image

s_i represents the amplitude of the slave image

$\delta_{\Delta,A}$ represents standard deviation of the amplitude difference between master and slave images

$\mu_{\Delta,A}$ represents mean amplitude

$\psi_{x,1}$ represents wrapped phase

$\tilde{\psi}_{x,1}$ represents the spatially uncorrelated term

$\Delta\tilde{\phi}_{\theta,x,i}$ represents the spatially correlated term

x, r represent the azimuth and range pixel coordinates

This method is particularly valuable for monitoring slow ground movements, such as subsidence and uplift, which occur over months to years. SBAS has proven to be an effective and widely used technique in various geodetic and geomorphic studies, providing valuable information for understanding surface displacements and geomorphic processes in areas of interest. Its ability to tackle temporal decorrelation challenges makes it a powerful tool for analysing long term InSAR time series data and extracting valuable deformation information from RADAR imagery.

3.4 Auxiliary Datasets

Landsat imagery was utilised as a key component of the methodology to investigate the causes of landslides in the study area. Imagery from both the wet and dry seasons was acquired to capture seasonal variations in land surface conditions as shown in Table 3 which provides an overview of the acquired imagery dates, the LandSat satellite used, and the corresponding wet or dry season.

Table 3: LandSat Imagery Information

Imagery Date	**Landsat Satellite**	**Season**
21st December 1973	1	Wet
27th August 1984	5	Dry
17th December 1984	5	Wet
6th June 1992	4	Dry
13th December 1994	5	Wet
10th February 2002	7	Dry
2nd June 2002	7	Wet
23rd May 2013	8	Wet
28th September 2013	8	Dry
24th May 2022	9	Wet
29th September 2022	9	Dry

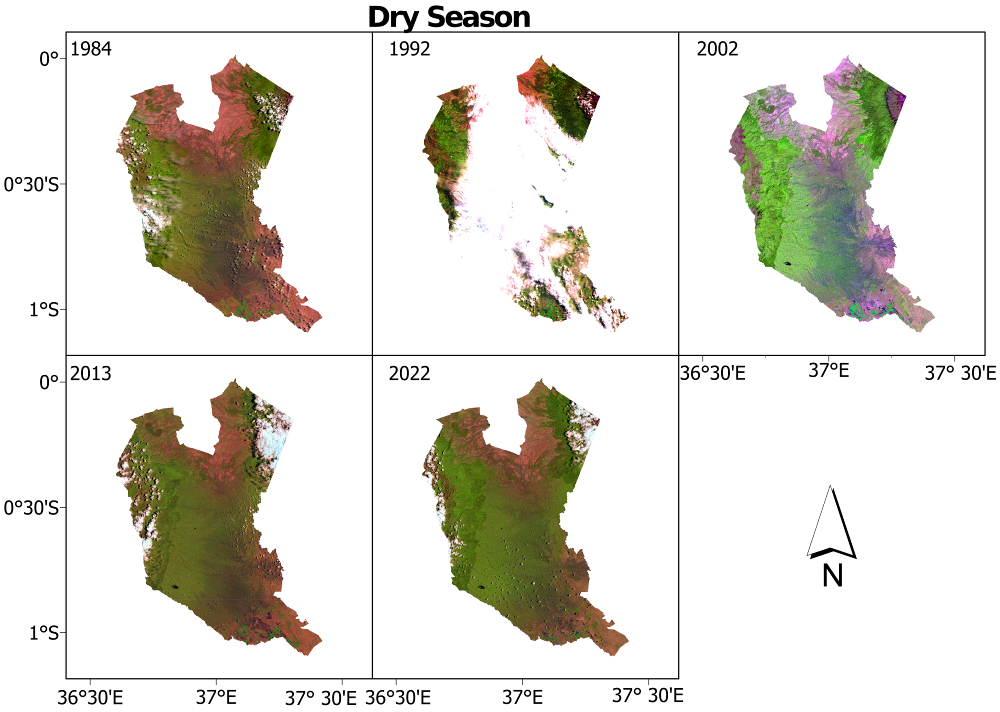

Figure 16: LandSat Imagery of the study area during the Dry Season

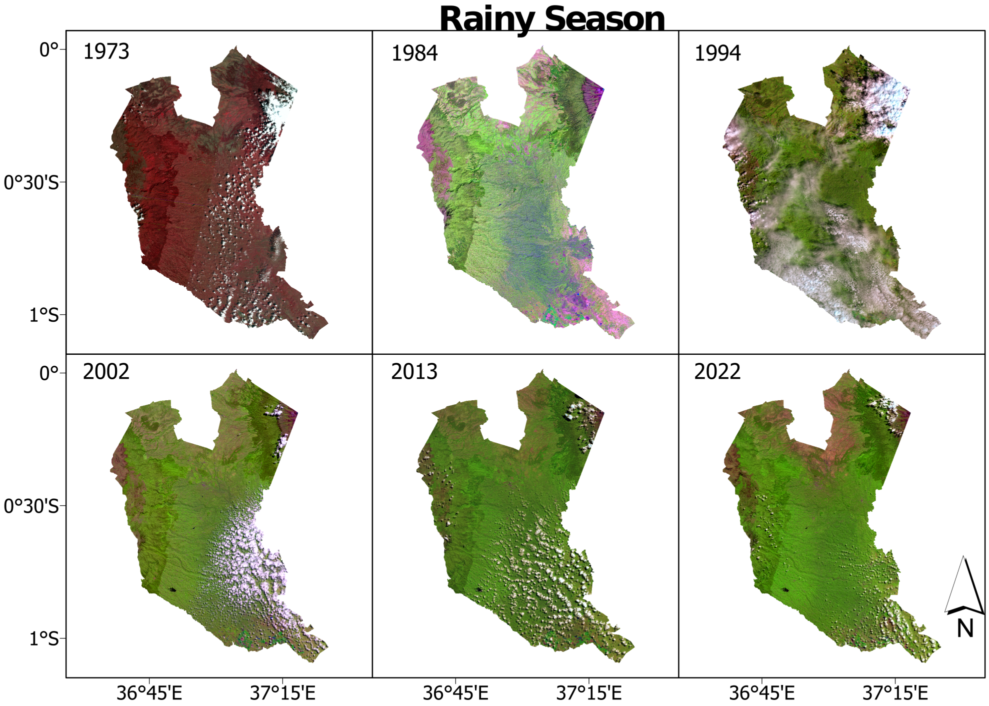

Figure 17: LandSat Imagery of the study area during the Wet Season

However, it is crucial to acknowledge that while the LandSat mission has been operational since the 1970s, data availability can be sporadic over certain areas. This posed a challenge during the analysis, making it difficult to obtain imagery for specific wet or dry months. Consequently, in some epochs, imagery was chosen from months slightly before or after the target season.

Cloud cover also presented challenges during the analysis, as observed in Figures 16 and 17. In some cases, epochs had to be discarded due to extensive cloud cover, notably the wet season imagery in 1992 and dry season imagery in 1994.

Various spectral indices as shown in Equations 10, 11, 12 and 13 including the Normalized Difference Vegetation Index (NDVI), Modified Normalized Difference Water Index (MNDWI), Built-up Index (BU), and Normalized Difference Built-up Index (NDBI), were computed from the Landsat data. These spectral indices are crucial for assessing vegetation health, water presence, and urban development, which are relevant factors contributing to landslide occurrences.

Furthermore, the acquired imagery was subjected to classification techniques to derive land use land cover changes over time. Where applicable, land use and land cover changes were analysed from as early as 1973 up to 2022, providing valuable insights into long term trends that may have influenced the occurrence and spatial distribution of landslides in the study area. The integration of Landsat imagery processing, spectral indices computation, and land use land cover classification allows for a comprehensive and multi-temporal analysis, aiding in understanding the drivers of landslides and their spatio-temporal dynamics.

$$BU = NDBI - \ NDVI \tag{10}$$

$$NDBI = \frac{SWIR - \ NIR}{SWIR + \ NIR} \tag{11}$$

$$NDVI = \frac{NIR - \ Red}{NIR + \ Red} \tag{12}$$

$$MNDWI = \frac{Green - \ SWIR}{Green + \ SWIR} \tag{13}$$

Where the following are bands in the ElectroMagnetic (EM) spectrum:

$Red, Green, Blue$ represents the bands in the visible portion

NIR represents the Near Infrared band

$SWIR$ represents the Shortwave Infrared band

The accuracy of the classified Landsat imagery was rigorously evaluated using two essential metrics: the kappa coefficient, $\hat{K}$ and the confusion matrix. The kappa coefficient, as computed in Equation 14, provided a comprehensive assessment of the classification accuracy, considering the agreement between the classified results and the training data. This statistical measure quantified the level of agreement, producing a value between -1 and 1, where higher values indicated better classification accuracy. Additionally, the confusion matrix was utilised to analyse the specific types of errors made during classification, such as false positives and false negatives, for each land cover category. The combination of these evaluation methods allowed for a robust assessment of the classification results, providing valuable insights into the reliability and performance of the classification process. These accuracy assessment techniques ensured the validity of the classified Landsat imagery, enhancing the credibility of the research findings and facilitating informed decision-making for land use and land cover applications.

$$\hat{K} = \frac{T \sum_{i=1}^{\hat{r}} m_{i,i} - \sum_{i=1}^{\hat{r}} (G_i C_i)}{T^2 - \sum_{i=1}^{\hat{r}} G_i C_i} \tag{14}$$

Where:

i is the class number

T is the total number of classified values compared to truth values

$m_{i,i}$ is the number of values belonging to the truth class i that have also been classified as class i

C_i is the total number of predicted values belonging to class i

G_i is the total number of truth values belonging to class i

3.4.1 SRTM Arcsecond DEM

The Space Shuttle Endeavour's Shuttle Radar Topography Mission (SRTM) Arcsecond Digital Elevation Model (DEM) played a crucial role in extracting important geomorphological factors, including slope, aspect, surface roughness, in the study area. The SRTM DEM is a globally available dataset acquired during the SRTM in February 2000. It provides high resolution elevation data for most of the Earth's surface at approximately one arc-second resolution (around 30 meters) (Farr et al. 2007, Farr & Kobrick 2000, Kobrick 2006).

The selection of the SRTM Arcsecond DEM for this study was motivated by its compatibility with automated processing in InSAR, ensuring seamless integration into the workflow. Furthermore, the vertical accuracy of the SRTM Arcsecond DEM has been validated through various studies, attesting to its reliability as a robust elevation dataset for precise and accurate geospatial analyses.

Leveraging the SRTM DEM, the study successfully extracted geomorphological parameters, such as slope, aspect, and surface roughness, which are essential in characterising the terrain and landforms in the region of interest.

Elevation and Slope : Elevation and slope steepness are key topographic factors that influence landslide susceptibility. Steeper slopes are generally more prone to landslides, while elevation can affect factors such as precipitation patterns and soil moisture.

Aspect : Aspect refers to the direction in which a slope faces. It can influence the amount of solar radiation received and, consequently, affect factors like temperature and soil moisture, which in turn can influence landslide susceptibility.

Surface Roughness : Surface roughness is a measure of terrain variation. Areas with high surface roughness may have a complex topography, which can affect the movement of water and the stability of slopes.

These extracted geomorphological factors were then utilised in correlation analyses in relation to the derived deformation from InSAR processing. By linking the InSAR-derived deformation with the geomorphological characteristics, the study aimed to gain insights into the potential relationships and influences between surface characteristics and deformation phenomena in the study area.

3.4.2 Rainfall Data

Tropical Applications of Meteorology using SATellite data (TAMSAT) is a research initiative co-led by the University of Reading and the National Centre for Atmospheric Science (NCAS) in the United Kingdom that focuses on providing reliable and accurate rainfall estimates for tropical regions of Africa (Maidment et al. 2017, Maidment et al. 2014, Tarnavsky et al. 2014). It was established to address the challenges of limited and often unreliable rainfall data in many African countries, where agriculture and livelihoods heavily depend on precipitation patterns. It was for this reason that TAMSAT was chosen over other existing global models.

TAMSAT utilises satellite data, particularly from geostationary and polar-orbiting satellites, to develop high quality rainfall products and monitor rainfall variability across the African continent (Maidment et al. 2017, Maidment et al. 2014). The initiative employs state of the art algorithms and data assimilation techniques to improve the accuracy and spatial coverage of its rainfall estimates. Over the years, TAMSAT has become a valuable resource for meteorologists, hydrologists, agricultural researchers, and policymakers, providing essential rainfall data for drought monitoring, crop yield forecasting, and climate resilience planning in the region.

The availability of TAMSAT's rainfall time series data makes it a valuable asset for studies investigating the impacts of rainfall on natural hazards, such as landslides and surface deformations, as well as various other environmental and socio-economic applications in Africa. Studies such Dubache et al. (2021) and Maidment et al. (2014), as have carried out validation of the TAMSAT dataset and found it to perform well over some parts of Africa.

Rainfall data played a significant role in understanding the relationship between rainfall patterns and occurrences of landslides and surface deformations. The rainfall time series data was sourced from TAMSAT. Rainfall is a critical environmental factor that can trigger landslides and influence surface deformation processes. It plays a fundamental role in soil saturation, which is a major factor leading to landslides in hilly and mountainous regions. Excessive or prolonged rainfall can increase pore pressure in the soil, reducing its shear strength and potentially triggering slope failures.

By incorporating rainfall data from TAMSAT, this study aimed to explore the correlation between rainfall events and the occurrences of landslides and deformation phenomena identified through InSAR processing and geomorphological analysis. The inclusion of rainfall data in the correlation analysis is essential for a comprehensive understanding of the driving forces behind slope instability and surface deformations.

3.4.3 Lithology and Soil

To comprehensively investigate the causality of deformation in our study area and its potential correlation with landslide occurrence, we recognised the significance of considering not only climatic variables and geomorphological factors but also the lithology and soil properties of the study area. The interplay of geological, geomorphological, and climate-related factors with deformation patterns is essential for a holistic understanding of landslide susceptibility. As a result, we incorporated the lithology and soil of the study area into our correlation analysis.

Lithology characteristics and soil properties play a fundamental role in landslide occurrence. Different types of rocks and soil have varying levels of susceptibility to erosion and instability. The integration of these factors alongside climatic data in our correlation analysis allows for a more comprehensive assessment of the drivers of deformation and landslide occurrence. It enables us to explore the combined influence of both climatic, geomorphological variables and not only the lithology but also soil properties on the observed deformation patterns.

The results of these analyses, which examine the relationships between deformation, precipitation, geomorphological factors and lithology and soil properties, are discussed in subsequent sections. By considering both climatic, geomorphological variables and lithology and soil properties, this research aimed to provide a more holistic understanding of the complex factors contributing to deformation and landslide susceptibility in the study area.

Chapter 4

Results and Analysis

4.1 Derived Deformation

In this study, the analysis of InSAR imagery was conducted using data acquired from two different sensors: ALOS PALSAR and Sentinel-1. The ALOS PALSAR imagery was acquired in the ascending node, while Sentinel-1 imagery was acquired in both the ascending and descending nodes. The analysis involved the generation of interferograms to study the deformation trends in the study area.

From the processing of ALOS PALSAR imagery, a total of approximately 24 interferograms were generated. For Sentinel-1 imagery, about 69 interferograms were generated from the ascending node acquisitions and 80 interferograms from the descending node acquisitions. These interferograms were crucial for tracking surface deformation over time and understanding the spatial distribution of deformation in the study area.

To visualise the LoS deformation across the study area, Figure 18 displays the distribution of LoS deformation values obtained from the analysis. The LoS deformation map provides a spatial representation of the surface displacement patterns, highlighting areas of subsidence and uplift as derived from the different sensors utilised in the research.

The deformation trends derived from the Sentinel-1 acquisitions nodes exhibited consistent patterns. In the Northern part of the study area, a general subsidence trend was observed, while in the Southern part, a general subsidence trend was also evident. This agreement in deformation trends between the two Sentinel-1 acquisition nodes reinforces the robustness of the findings. The minimum rate of subsidence derived from the Sentinel-1 acquisitions is -201 mm/yr while the maximum rate of uplift is 210 mm/yr.

However, the deformation trend derived from the ALOS PALSAR imagery contradicted the trends observed in the processed Sentinel-1 data. The ALOS PALSAR-derived deformation exhibited antagonistic patterns compared to the Sentinel-1 trends with a minimum subsidence rate of -716 mm/yr and a maximum uplift rate of 101 mm/yr as seen in Figure 18. This discrepancy could be attributed to several factors, including the limited availability of data from the ALOS PALSAR sensor and the longer temporal baselines used for coregistration, which extended up to 875 days. The longer temporal baselines can introduce more complex phase changes due to additional environmental and anthropogenic factors, leading to potential inaccuracies in the derived deformation patterns as summarised in Table 4.

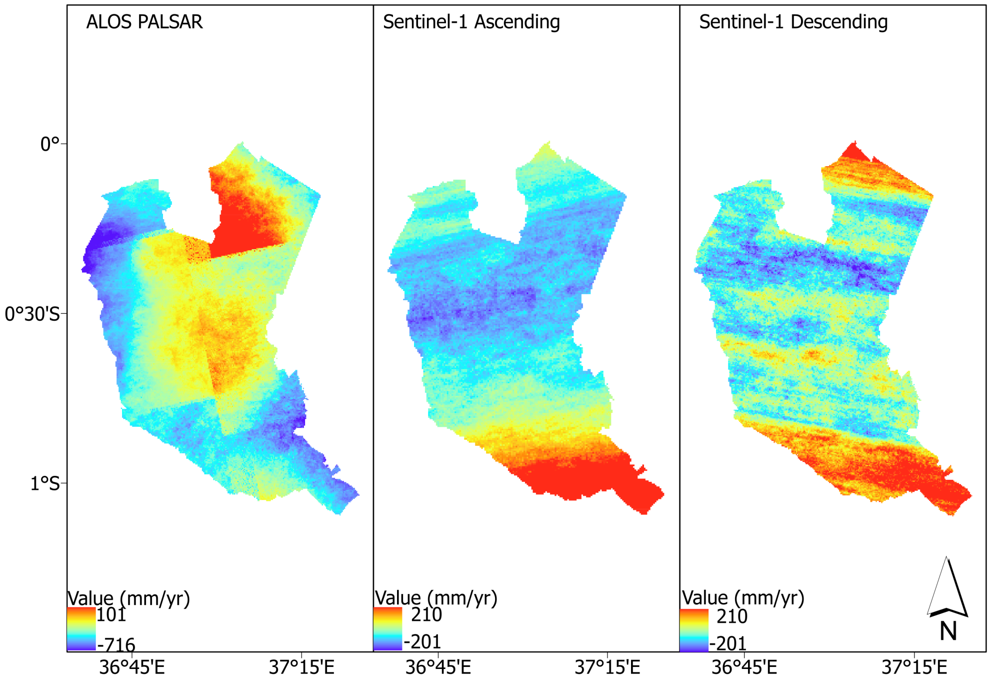

Figure 18: LoS deformation derived by processing RADAR imagery acquired by different sensors

To gain further insight into the deformation patterns observed in the study area, specific points of interest were selected for detailed analysis. These points were identified based on the processed interferograms generated from Sentinel-1 imagery acquired in the descending node. This choice was motivated by the fact that the descending node data provided the longest time series, enabling a more comprehensive assessment of deformation trends over an extended period.

The selection process of these points of interest was driven by the identification of unstable areas through Permanent Scatterer (PS) analysis conducted during the STAMPS/MTI processing. Permanent Scatterers are coherent reflectors that remain coherent over time and can be used as reliable indicators of ground deformation.

Points of interest were strategically chosen to include unstable regions experiencing both pronounced uplift and subsidence rates to capture a comprehensive representation of the high deformation patterns within the study area. The spatial distribution of these selected points of interest is depicted in Figure 19, which provides a visual representation of their locations across the study area. The selection of these points is expected to provide valuable insights into the spatial variation of deformation, aiding in the characterisation of subsidence or uplift patterns.

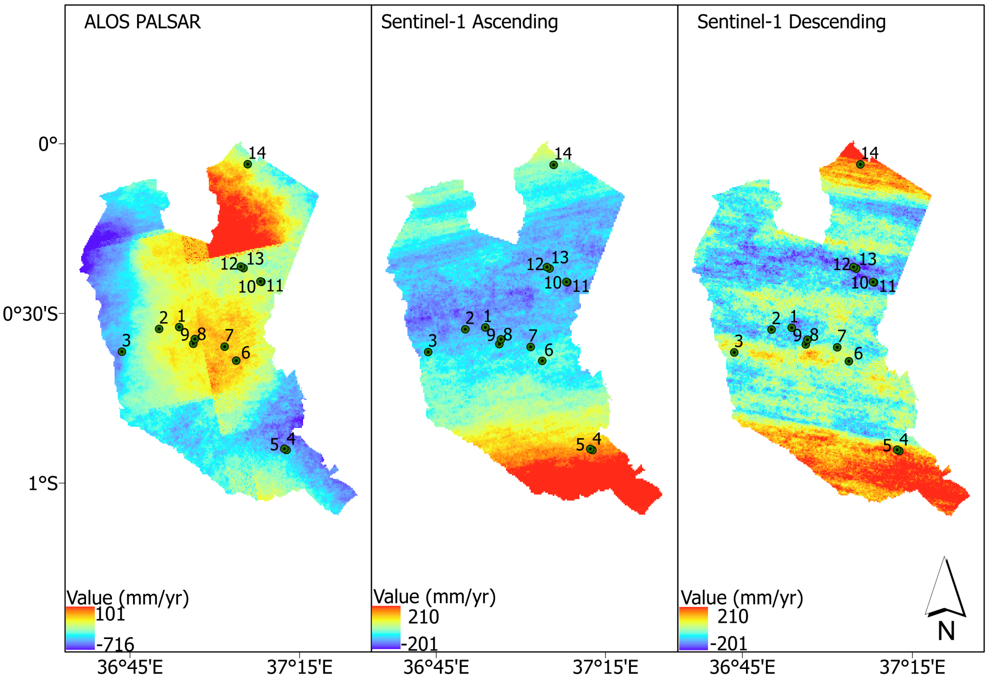

Figure 19: Identified points of interest overlaid on the LoS deformation derived by processing RADAR imagery acquired by different sensors

Table 4: Deformation rates derived from different sensors for the points of interest in the study area (Units: mm/yr)

Point	ALOS PALSAR (2007 - 2010)	S1 Ascending (2017 - 2021)	S1 Descending (2015 - 2021)
1	-715.9	-135.4	77.9
2	-715.9	-169.4	72.0
3	-715.9	-129.9	81.8
4	-68.6	108.3	207.0
5	-60.8	172.6	209.9
6	100.4	19.8	59.5
7	92.5	-63.8	62.5
8	-715.9	-106.6	70.9
9	-715.9	-90.7	71.2
10	16.5	-154.0	-178.8
11	43.0	-172.4	-176.8
12	78.8	-129.5	-199.6
13	80.9	-163.6	-200.8
14	100.8	-72.6	-90.7

4.1.1 Sentinel-1 Ascending

For this analysis, the chosen master image's date was set to the 3$^{\text{rd}}$ of July 2019, allowing for the investigation of deformation trends over time with reference to this specific date. Additionally, to optimise data quality, temporal and perpendicular baselines were confined to 60 days and 200 metres, respectively.

From the processed Sentinel-1 imagery, several points of interest were identified based on the analysis of time series data. Among these points, four locations, specifically points 4, 5, 12, and 13, were found to exhibit the most unstable behaviour. These points were characterised by notable variations in their LoS deformation rates when compared to the chosen master image.

Points 4 and 5 displayed an uplifting trend with respect to the master image, with mean deformation rates of 108.3 mm/yr and 172.7 mm/yr, respectively. These findings suggest that the ground at these locations is rising over time. Conversely, points 12 and 13 exhibited a subsiding trend, with mean deformation rates of -129.5 mm/yr and -163.6 mm/yr, respectively. This indicates that the ground at these points is undergoing a downward displacement relative to the master image date.

The time series deformation behaviour of these points is visually represented in Figure 20, providing a clear illustration of the fluctuations in LoS deformation over the selected time period.

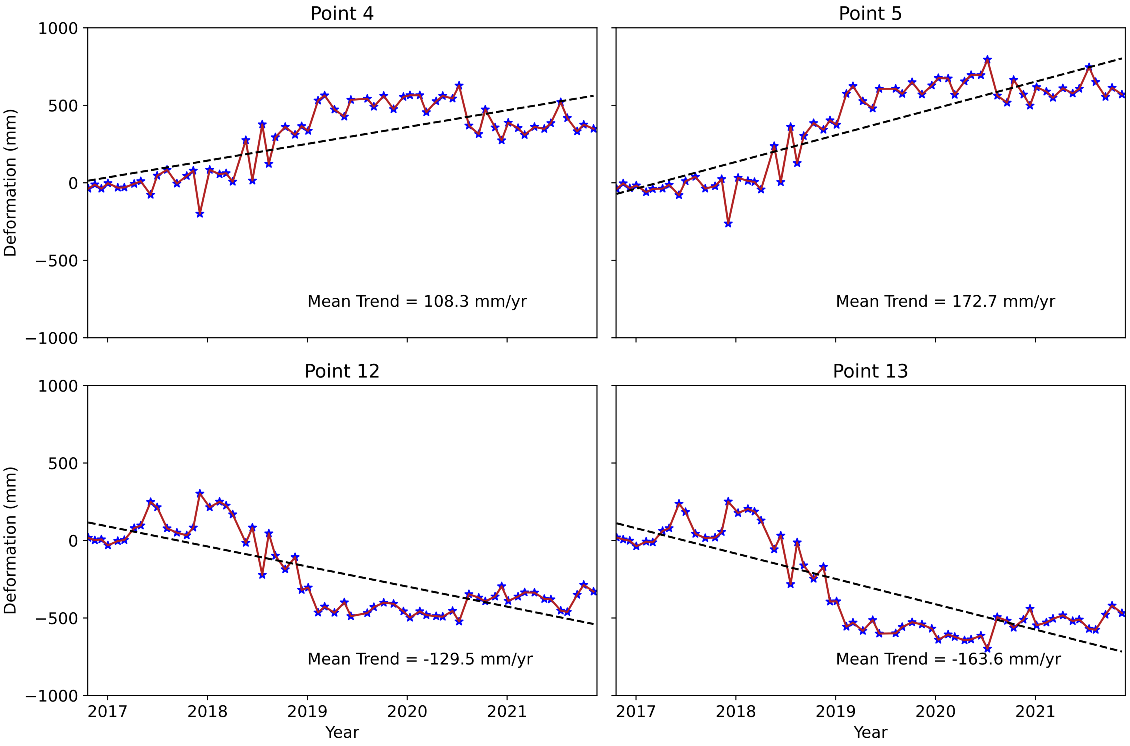

Figure 20: Sentinel-1 Ascending LoS deformation of selected points in the study area

4.1.2 Sentinel-1 Descending

The analysis of Sentinel-1 descending imagery data offered a comprehensive understanding of deformation patterns within the study area. To ensure consistency with previous analyses, the selected master image date was set to the 24th of May 2019. Similarly, temporal and perpendicular baseline constraints were maintained at 60 days and 200 metres, respectively, as in the processing of Sentinel-1 ascending imagery.

Notably, the deformation trends observed in the Sentinel-1 descending imagery closely matched those derived from the processed Sentinel-1 ascending imagery. Specifically, points 4, 5, 12, and 13 exhibited deformation trends that were consistent with their behaviour in the ascending imagery dataset.

Points 4 and 5 continued to display an uplifting trend in relation to the chosen master image date, with mean deformation rates of 207.0 mm/yr and 209.9 mm/yr, respectively. Conversely, points 12 and 13 maintained their subsiding trends, with mean deformation rates of -199.6 mm/yr and -200.8 mm/yr, respectively. These findings reinforce the stability of the observed deformation patterns, which are consistently corroborated by both ascending and descending Sentinel-1 imagery.

Figure 21 provides a visual representation of the time series deformation behaviour of these points, enabling a clear understanding of the temporal fluctuations in LoS deformation over the specified time period.

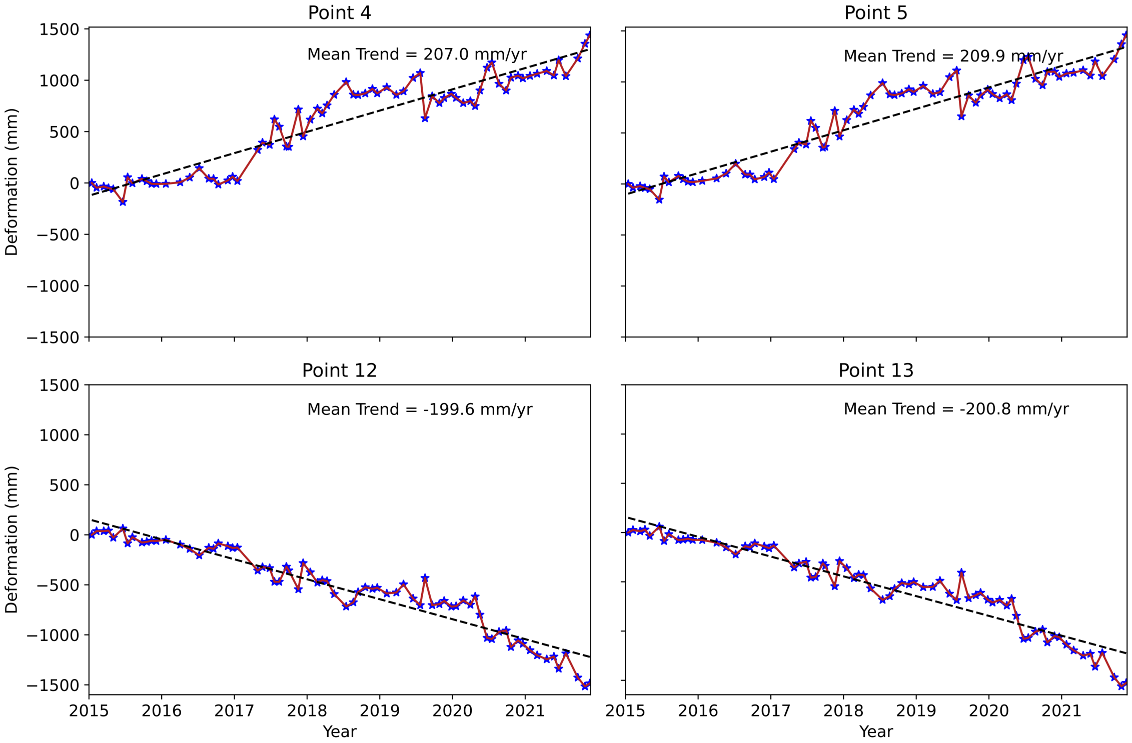

Figure 21: Sentinel-1 Descending LoS deformation of selected points in the study area

4.1.3 ALOS PALSAR

The results obtained from the ALOS PALSAR time series LoS deformation analysis revealed intriguing patterns within the study area. These patterns displayed antagonisic behaviour in comparison to the deformation trends derived from the processed Sentinel-1 ascending and descending imagery.

Points 4 and 5 exhibited subsiding trends with mean deformation rates of -68.6 mm/yr and -60.8 mm/yr, respectively. Conversely, Points 12 and 13 displayed an uplift trend with mean deformation rates of 78.8 mm/yr and 80.9 mm/yr.

Figure 22 visually represents the time series LoS deformation behaviour of these points, providing a clear illustration of the temporal fluctuations in LoS deformation over the specified time period.

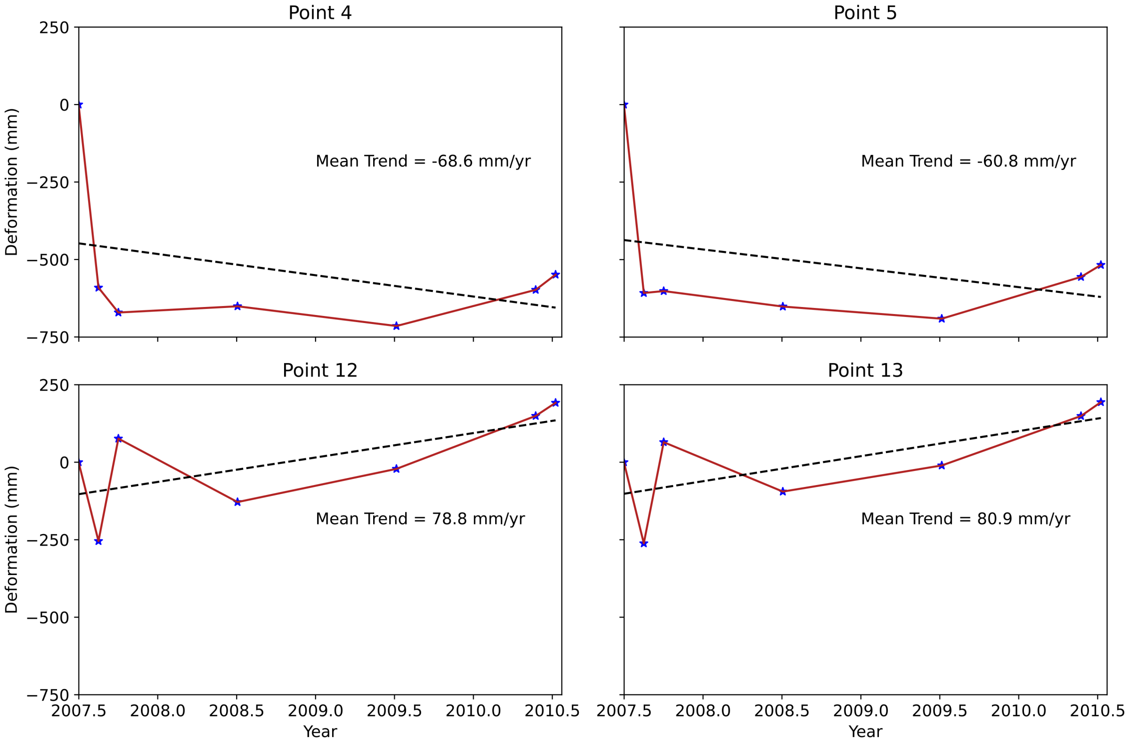

Figure 22: ALOS PALSAR LoS derived deformation of selected points in the study area

4.1.4 GRACE/GRACE-FO and GLDAS

The results obtained from the analysis of GRACE/GRACE-FO data and GLDAS CLSM data are presented in this section. It's worth noting that the spatial resolution of these datasets is coarser compared to the processed InSAR datasets; however, they offer the convenience of deriving vertical deformation of points of interest. The time series for GRACE/GRACE-FO data was from April 2002 to November 2021 while that for GLDAS was from March 2003 to November 2021.

Points 4, 5, 12, and 13, which were previously identified as significant in the InSAR analysis, were used to visualise the time series deformation for both the GRACE/GRACE-FO and GLDAS datasets, as shown in Figures 23, 24, and 25.

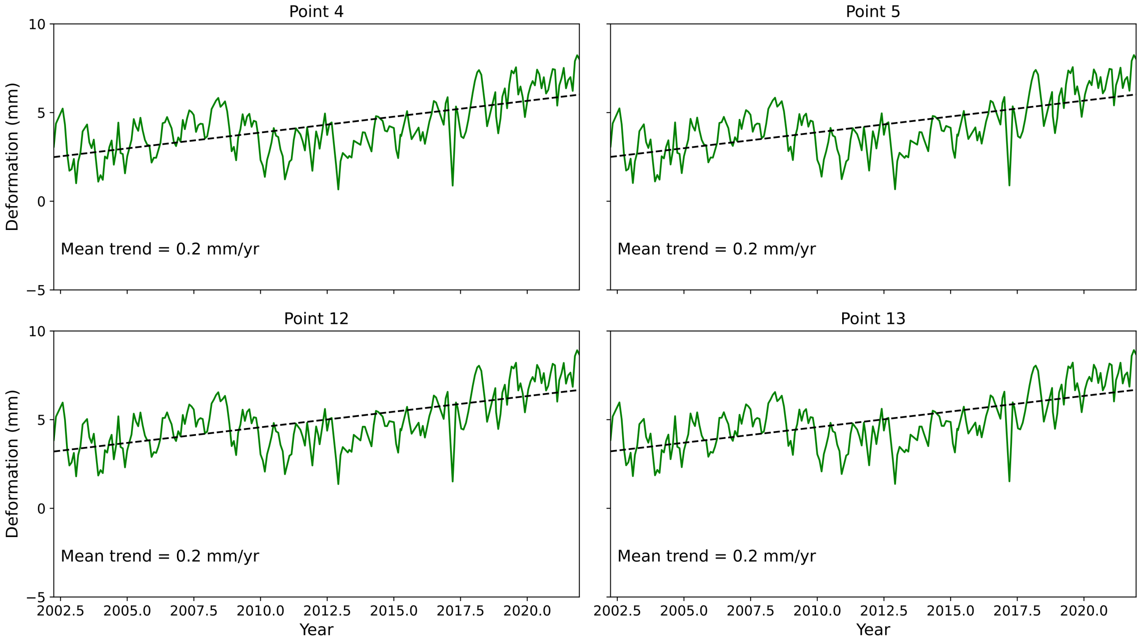

Figure 23: GRACE derived deformation of selected points in the study area

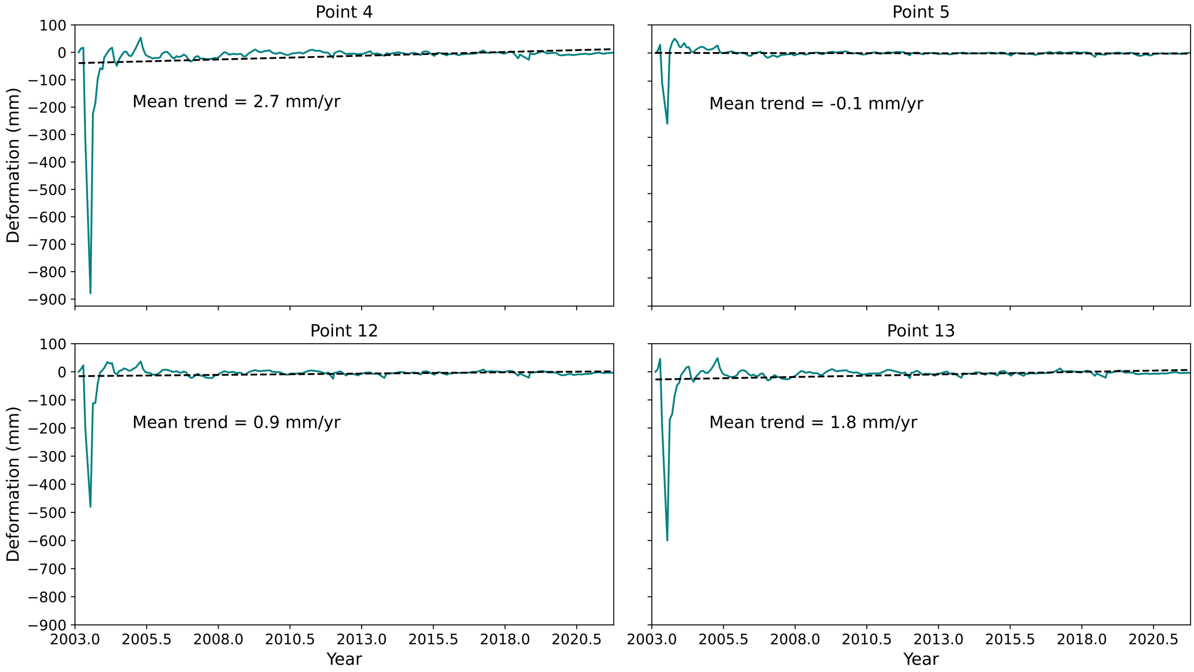

Figure 24: GLDAS derived deformation of selected points in the study area

From the GRACE/GRACE-FO data, the deformation rates for the aforementioned points were found to be relatively small, with values of 0.2 mm/yr for all points. In

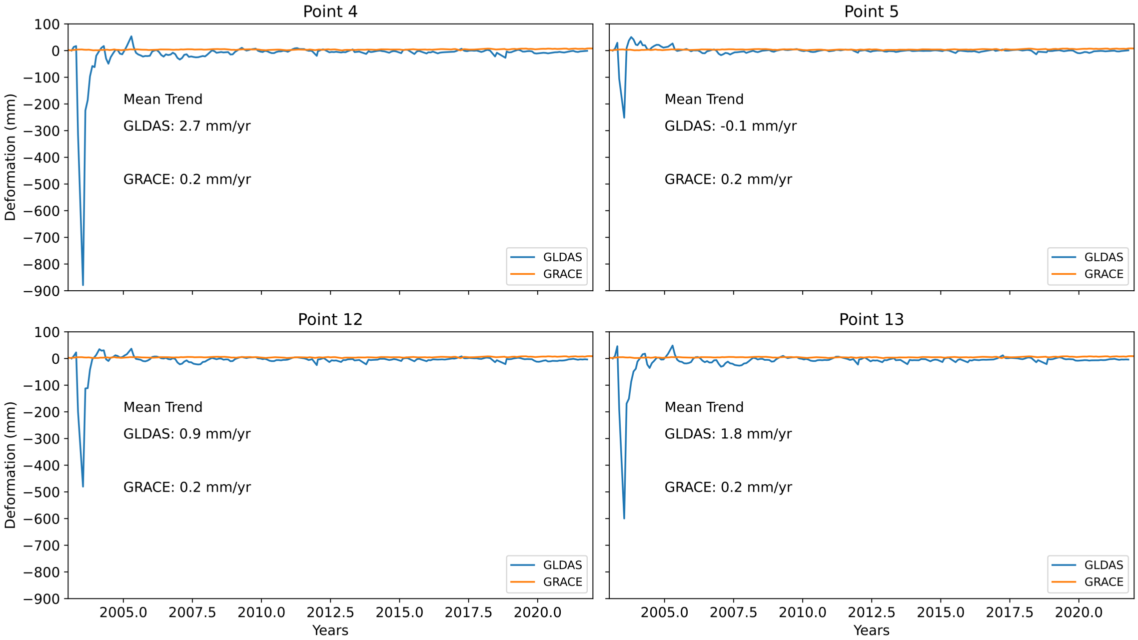

Figure 25: Comparing GRACE/GRACE-FO and GLDAS derived deformation of selected points in the study area

contrast, the GLDAS data yielded more pronounced deformation rates for the same points. According to GLDAS, the deformation rates for points 4, 5, 12, and 13 were 2.7 mm/yr, -0.1 mm/yr, 0.9 mm/yr, and 1.8 mm/yr, respectively.

However, during the analysis of the GLDAS data, potential outliers were detected in the time series deformation, which warranted further investigation. To confirm if these values were true outliers, statistical testing was conducted, leading to the removal of the outlier data points. After this removal, the time series deformation of the points was re-plotted as shown in Figures 26 and 27.

The mean deformation rates for point 4 changed to 0.3 mm/yr while point 5's deformation remained at -0.1 mm/yr, while for points 12 and 13, they changed to -0.2 mm/yr and 0.1 mm/yr. These revised mean deformation rates are more consistent with the GRACE/GRACE-FO data.

To assess the differences between the two datasets over their common time period, Figures 28 and 29 illustrate the changes in deformation rates before and after outlier removal. Before outlier elimination, the mean differences and their corresponding standard deviations for points 4, 5, 12, and 13 were -21 mm ± 69 mm, -8 mm ± 21 mm, -14 mm ± 38 mm, and -18 mm ± 47 mm, respectively.

After outlier elimination, the mean differences and standard deviations, although still significant, reduced significantly with the exception of point 5's mean difference which remain the same even though its standard deviation reduced. The mean differences and their standard deviations were computed as -12 mm ± 9 mm, -8 mm ± 4 mm, -11 mm ± 6 mm, and -12 mm ± 7 mm, for points 4, 5, 12 and 13 respectively. This adjustment reflects a closer alignment between the GRACE/GRACE-FO and

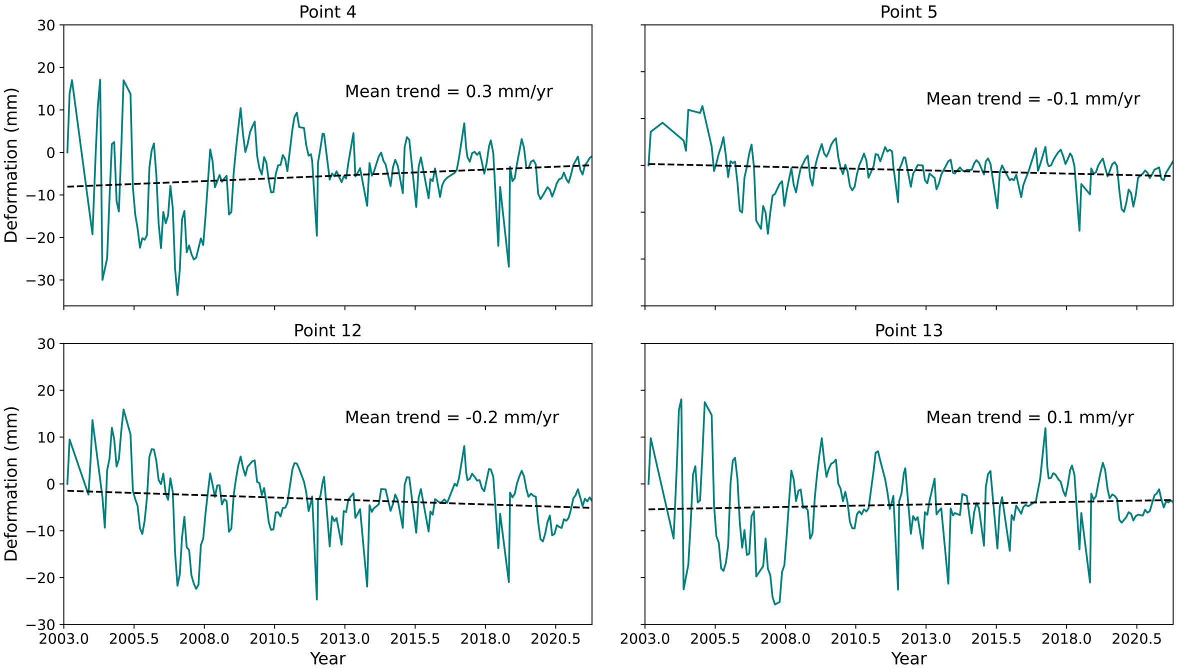

Figure 26: GLDAS derived deformation of selected points in the study area after eliminating outliers

Figure 27: Comparing GRACE/GRACE-FO and GLDAS derived deformation of selected points in the study area after eliminating outliers

GLDAS datasets, suggesting improved agreement in their estimates of vertical deformation rates.

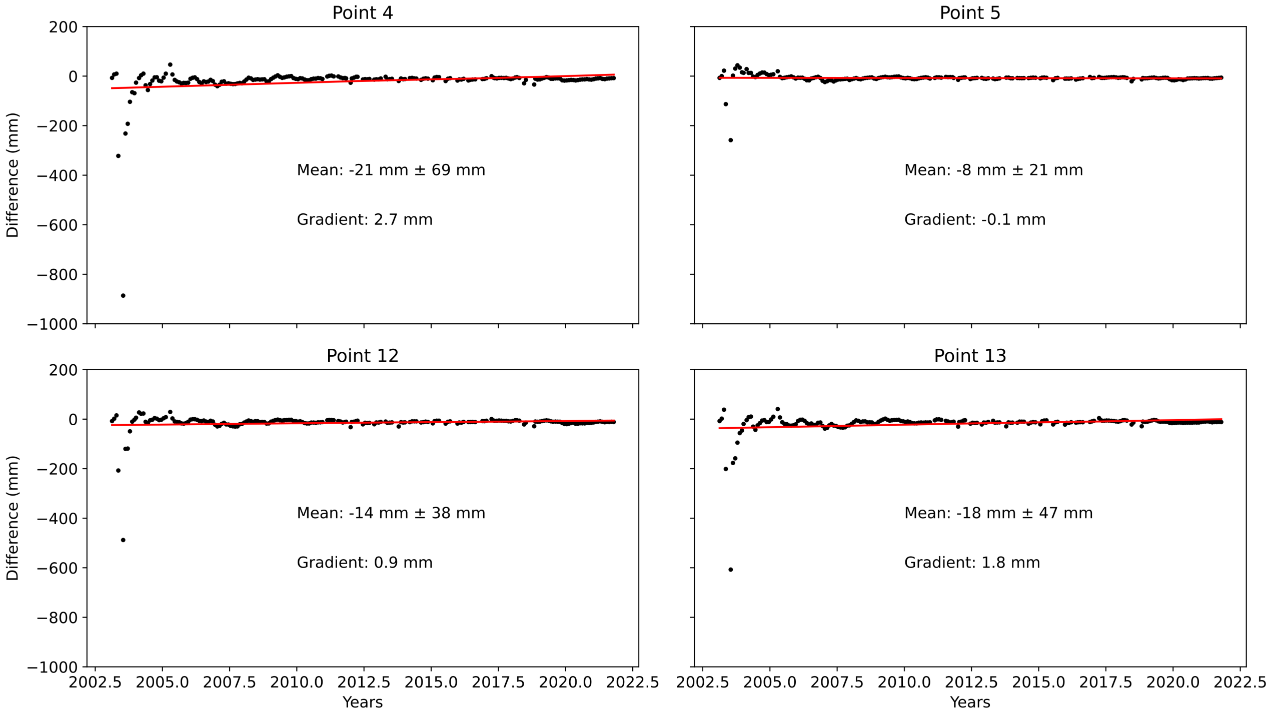

Figure 28: Comparing GRACE/GRACE-FO and GLDAS derived deformation of selected points in the study area

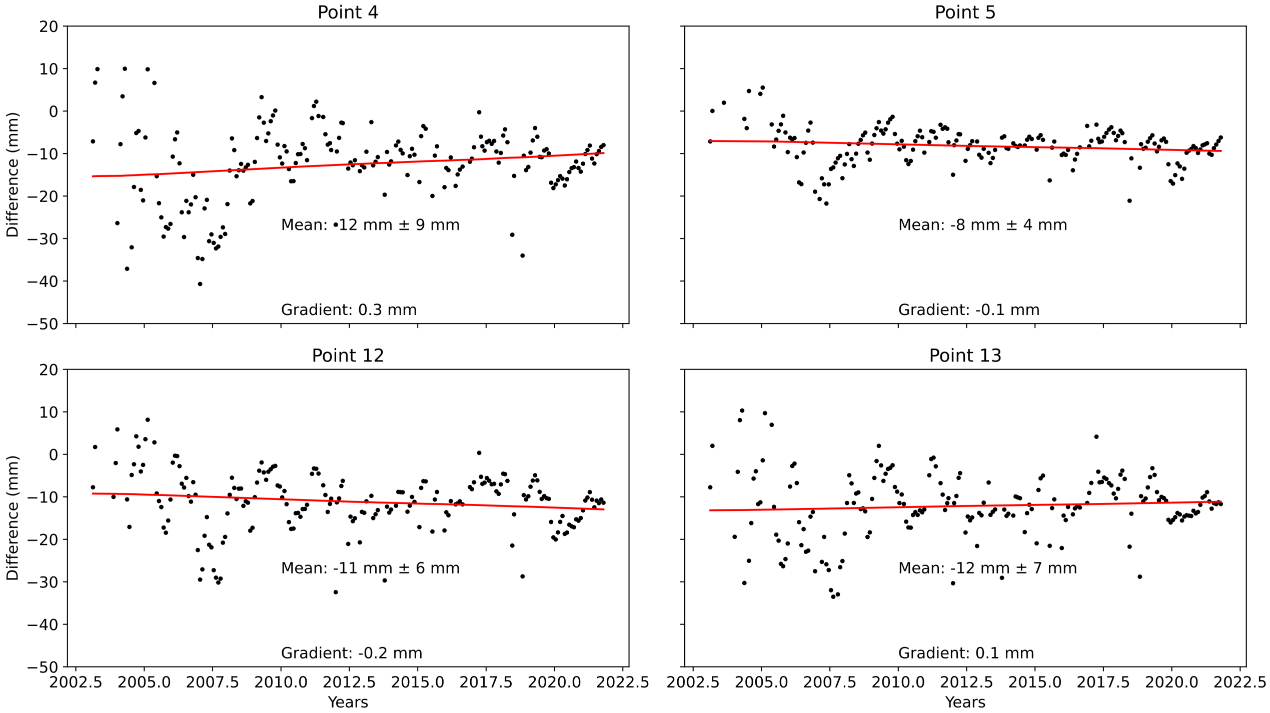

Figure 29: Comparing GRACE/GRACE-FO and GLDAS derived deformation of selected points in the study area after outlier elimination

4.1.5 Deformation Rates Comparison

A comparative analysis of deformation rates obtained from various datasets, including GRACE/GRACE-FO, GLDAS Hydrological Model, and InSAR processed data from ALOS PALSAR, Sentinel-1 Ascending, and Sentinel-1 Descending, is presented in Table 3 below. It is crucial to highlight that InSAR-derived deformation is in the LoS, while the deformation from other datasets is in the vertical direction. This table provides a comprehensive overview of the diverse deformation rates observed through different measurement techniques, facilitating a holistic understanding of the deformation patterns in the study area.

Table 5: Comparison of derived deformation rates derived from all processed datasets

	Deformation Rates (mm/yr)			
Sensor	Point 4	Point 5	Point 12	Point 13
Sentinel-1 Ascending	108.3	172.7	-129.5	-163.6
Sentinel-1 Descending	207.0	209.9	-199.6	-200.8
ALOS PALSAR	-68.6	-60.8	78.8	80.9
GRACE/GRACE-FO	0.2	0.2	0.2	0.2
GLDAS	0.3	-0.1	-0.2	0.1

4.2 Landslide Causative Agents

4.2.1 Change in LULC

In this section, we present the results of our land use and land cover classification analysis, which was conducted to determine the causes of landslides in the study area. LandSat imagery was chosen for this analysis due to its longevity and availability for several decades. The study area, encompassing Murang'a and Nyeri, experiences a wet season from mid-October to mid-May, making it essential to investigate land use and land cover trends during both the wet and dry seasons.

For the land use and land cover classification, the Maximum Likelihood (ML) method was chosen. The results of the classification are displayed in Figures 30 and 32, providing insights into the distribution of land cover classes across the study area.

To assess the accuracy of the classification, confusion matrices are provided in Appendix C. These matrices offer a detailed evaluation of the classification performance for each epoch.

One notable trend observed in the analysis is the variation in the area of the four broad chosen classes: Bare Land, Built-up Area, Vegetation, and Water, as illustrated in the bar graphs in Figures 31 and 33. It is evident that during the dry season, the Vegetation cover decreases, while Bare Land increases. Conversely, during the wet season, the trend is opposite, with Vegetation cover increasing, and Bare Land decreasing.

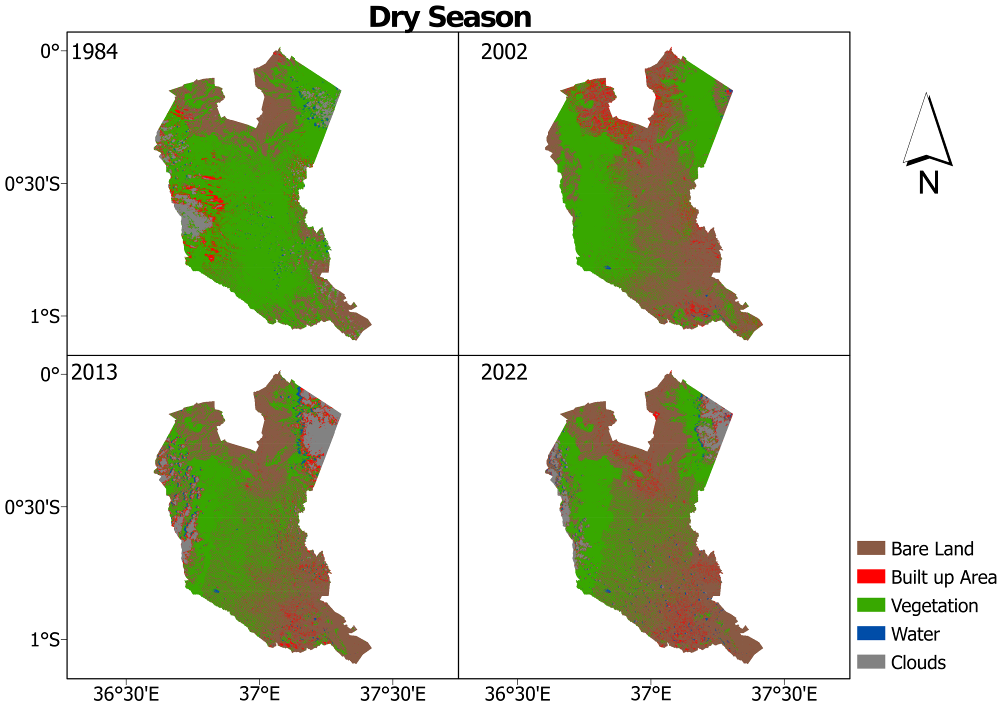

Figure 30: Variation in LULC in the study area during the Dry Season

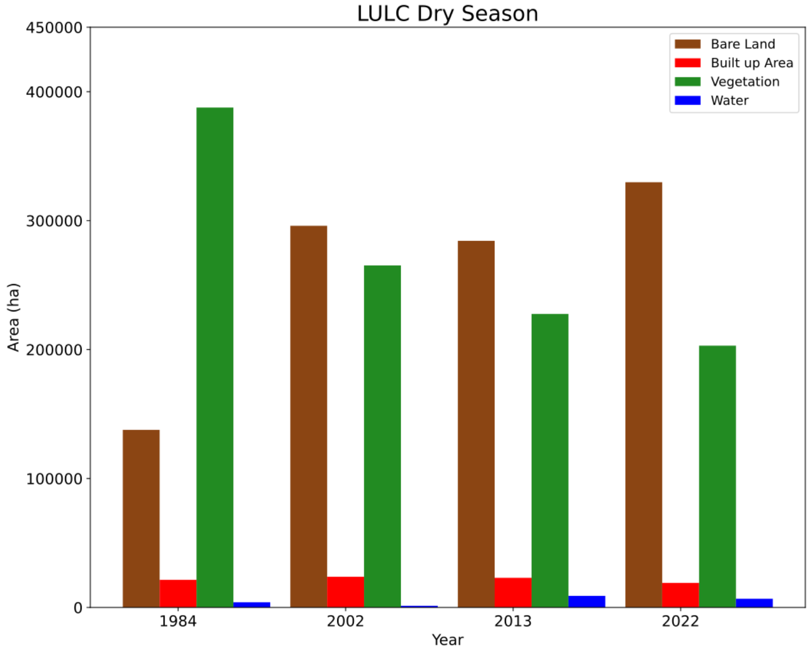

Figure 31: Variation in LULC area changes in the study area during the Dry Season

Another significant trend is observed in the percentage change of Built-up Areas, particularly during the wet season. The data suggests an increase in Built-up Areas over the years, indicating rising population growth and infrastructure development within the study area.

For a more detailed breakdown of the percentage changes in land use and land cover, the reader is referred to Tables 6 and 7.

Table 6: LULC Percentage Change during the Dry Season

Class	**1984-2002**	**2002-2013**	**2013-2022**
Bare Land	115%	-4%	16%
Built up Area	11%	-4%	-17%
Vegetation	-32%	-14%	-10%
Water	-69%	615%	-25%

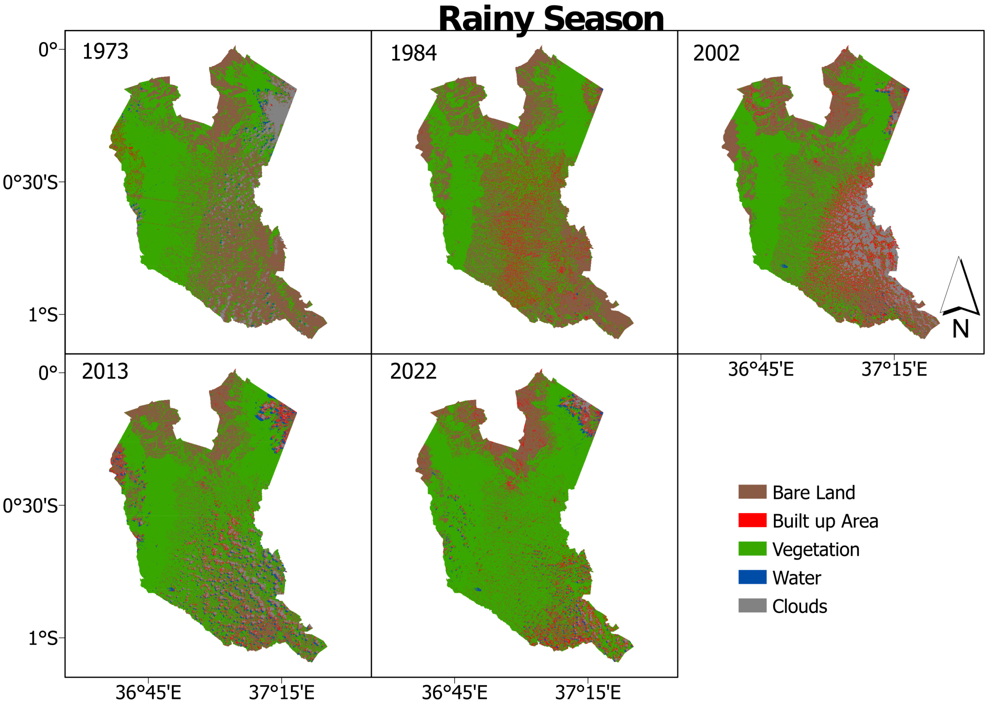

Figure 32: Variation in LULC in the study area during the Wet Season

Table 7: LULC Percentage Change during the Wet Season

Class	**1973-1984**	**1984-2002**	**2002-2013**	**2013-2022**
Bare Land	8%	-20%	-33%	-17%
Built up Area	594%	34%	-33%	16%
Vegetation	-2%	-8%	33%	15%
Water	-84%	170%	815%	-54%

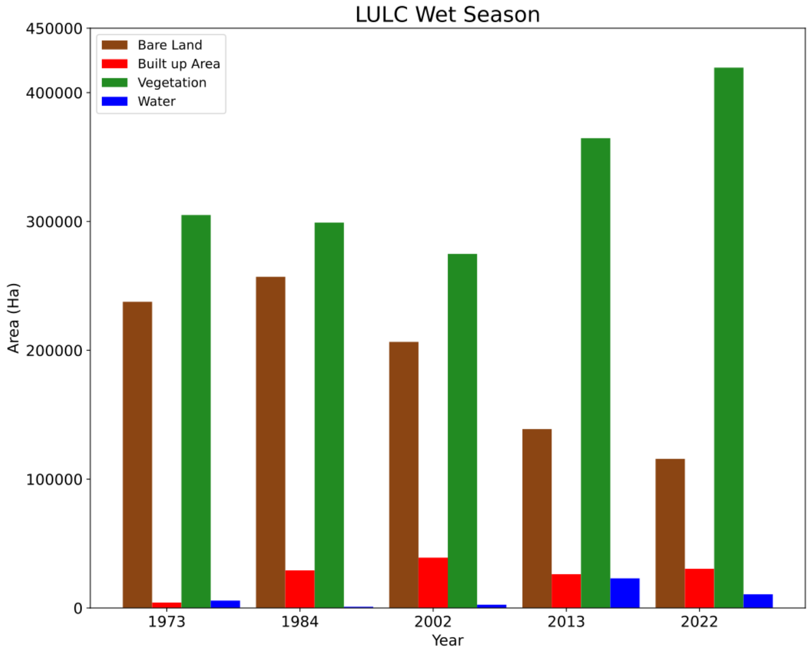

Figure 33: Variation in LULC area changes in the study area during the Wet Season

4.2.2 Trends in Vegetation Cover

NDVI was utilised in the analysis to detect changes in vegetation cover within the study area over both the wet and dry seasons. NDVI is a widely used vegetation index that is derived from image band math, based on the visible and near-infrared reflectance of vegetation. It provides a quantitative measure of vegetation health and density.

As expected, the analysis revealed that the wet season had the highest greenery in the scene compared to the dry season. NDVI analysis quantitatively visualised these differences in vegetation cover during different epochs within the study area, as displayed in Figures 34 and 35. These figures offer a clear representation of the seasonal variations in vegetation density.

To complement the NDVI analysis, we also employed MNDWI, which emphasises water bodies within the study area. MNDWI was chosen for its ability to discriminate between built-up areas and water features, as these can sometimes be conflated in other indices.

Figures 36 and 37 present the visualisations of MNDWI results. It's noteworthy that MNDWI values are antagonistic to the NDVI results in the study area. In areas with high vegetation density, MNDWI values are generally low, indicating a lower occurrence of open water bodies. Conversely, where there is a higher probability of open water bodies, MNDWI values are higher, suggesting a lower vegetation density.

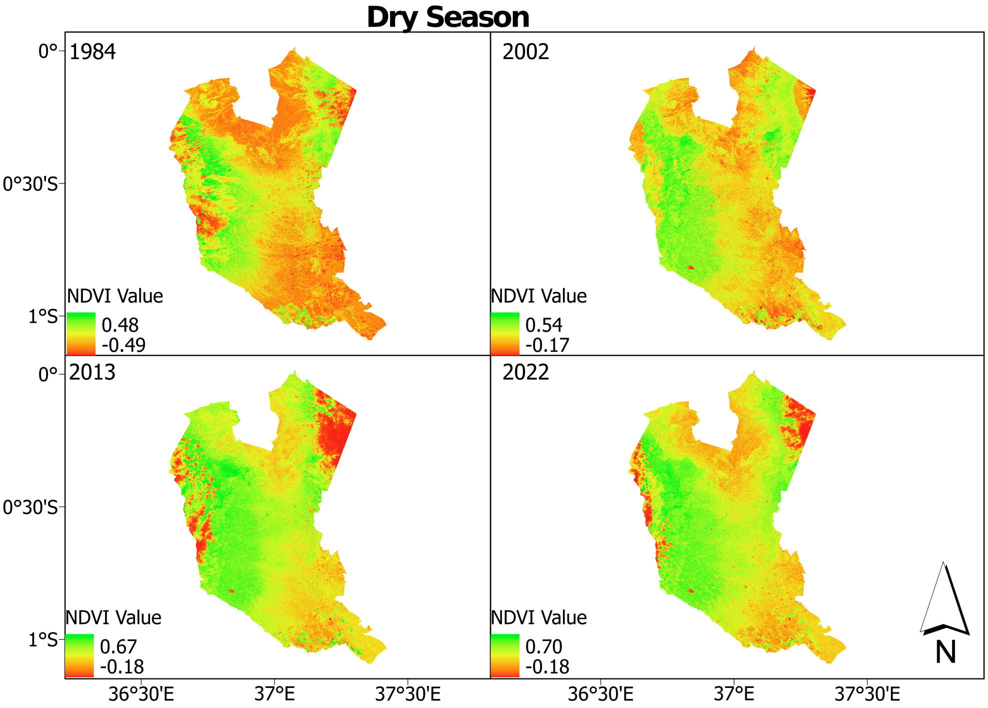

Figure 34: Variation in NDVI in the study area during the Dry Season

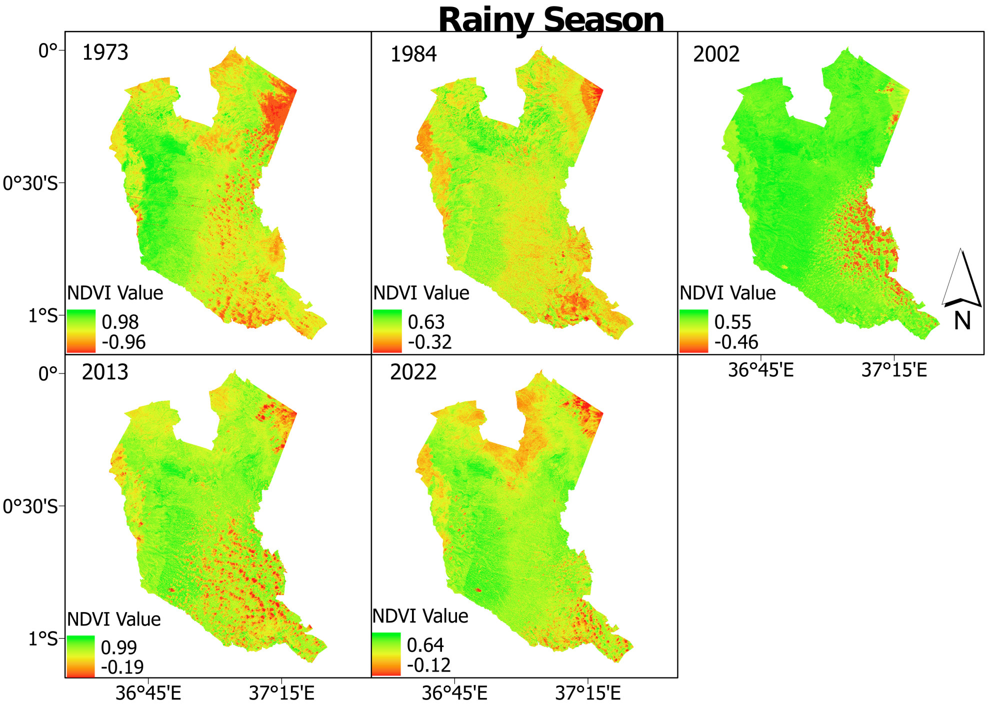

Figure 35: Variation in NDVI in the study area during the Wet Season

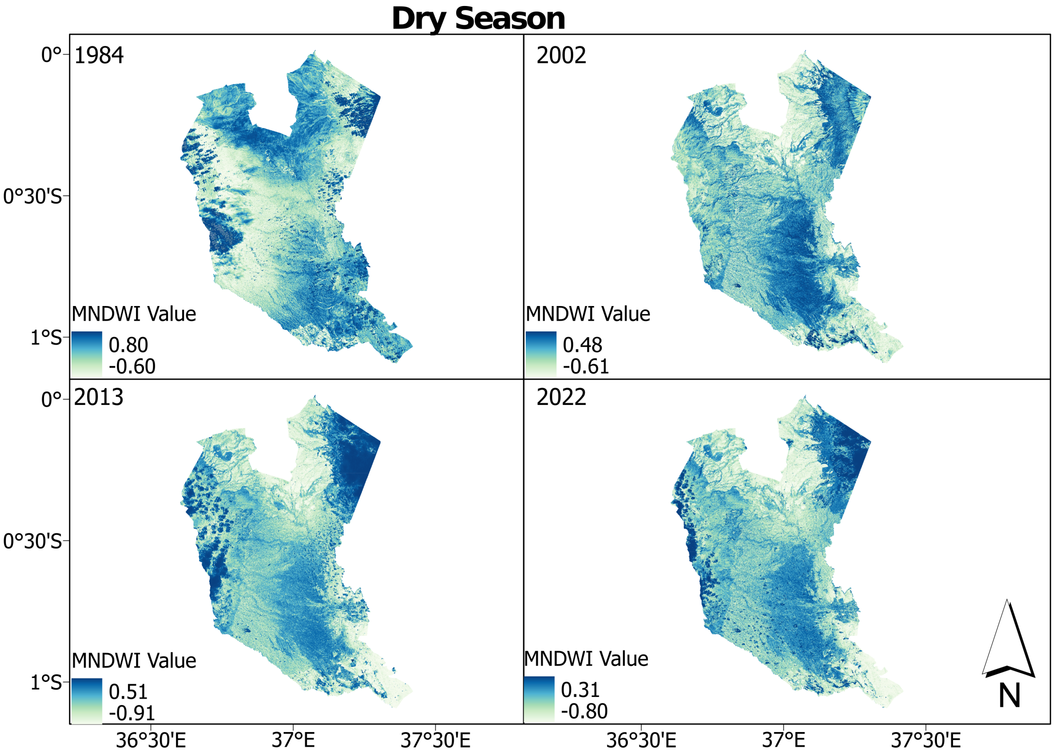

Figure 36: Variation in MNDWI in the study area during the Dry Season

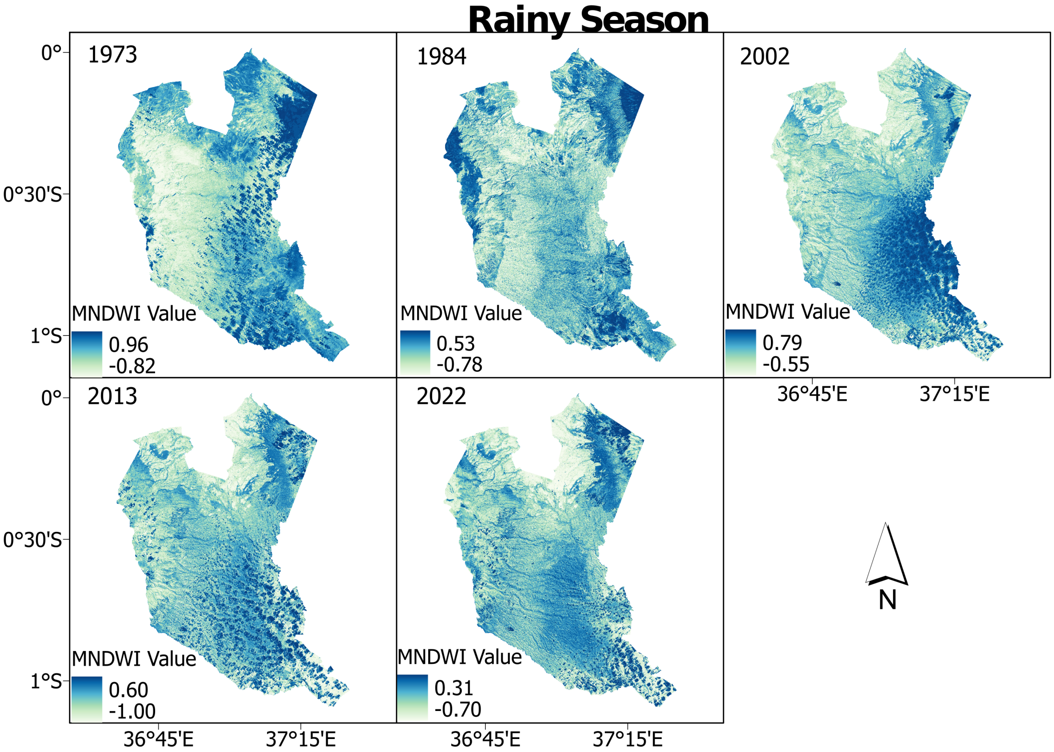

Figure 37: Variation in MNDWI in the study area during the Wet Season

4.2.3 Rainfall Patterns

Precipitation is a well-known trigger for landslides, making it a crucial factor to consider in landslide susceptibility assessments. To perform this analysis, we utilised rainfall data obtained from TAMSAT. It is important to note that deformation data derived from the processing of InSAR was exclusively used in the correlation due to its higher spatial resolution. InSAR provides detailed and localised information on surface deformation, which allows for a more precise correlation with precipitation patterns.

The results of this correlation analysis are presented in detail in Section 4.3.1, which follows. This section explores the relationship between deformation rates and rainfall, shedding light on whether changes in precipitation coincide with notable deformation events within the study area.

Understanding this correlation is of paramount importance in assessing landslide susceptibility. By identifying periods of increased deformation that align with significant rainfall events, insights into the potential triggers of landslides can be gained. These findings contribute to a better understanding of the complex interplay between climatic conditions and the occurrence of landslides in the study area.

4.3 Correlation Analysis

4.3.1 Rainfall and Deformation

Sentinel-1 Derived Deformation

In this section, the results of the correlation analysis between rainfall and deformation patterns derived from processed Sentinel-1 InSAR imagery are presented. This analysis was conducted separately for both the ascending and descending nodes of the satellite

To visualise the relationships between rainfall and deformation, time series deformation data overlaid with precipitation records was plotted. Figures 38 and 39 illustrate these time series graphs, both of which are in monthly intervals. The line represents time series deformation while the bars represent the amount of precipitation in a particular month. This symbolisation is also true for subsequent visualisations of deformation and rainfall.

It is evident from these plots that there is a noticeable trend: high and extreme precipitation events are often followed by subsidence events in the study area. This observation suggests a potential link between rainfall and surface deformation.

To quantitatively assess the strength and direction of this correlation, statistical analysis was performed, calculating the correlation coefficient between deformation and precipitation. The results of this analysis, as expected, reveal a negative correlation between uplift and precipitation and a positive correlation between subsidence and precipitation. This implies that periods of increased rainfall are associated with a reduction in surface elevation (subsidence) in the study area and vice versa.

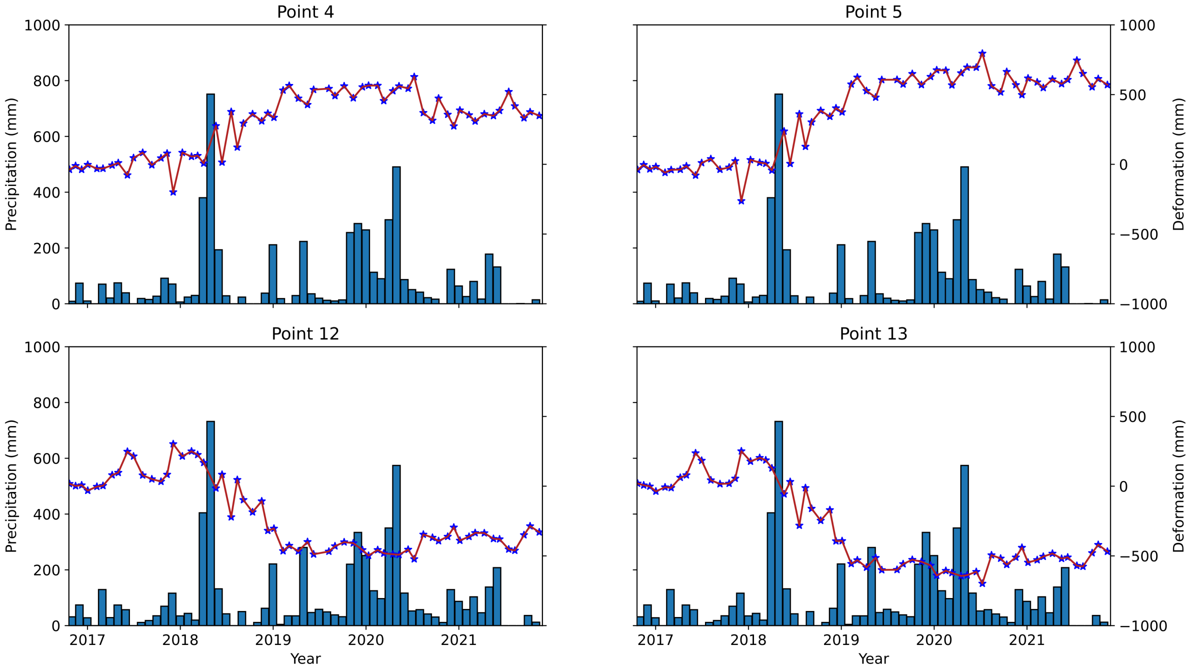

Figure 38: Sentinel-1 Ascending derived deformation superimposed on rainfall data. The line represents time series deformation while the bars represent the amount of precipitation in a particular month

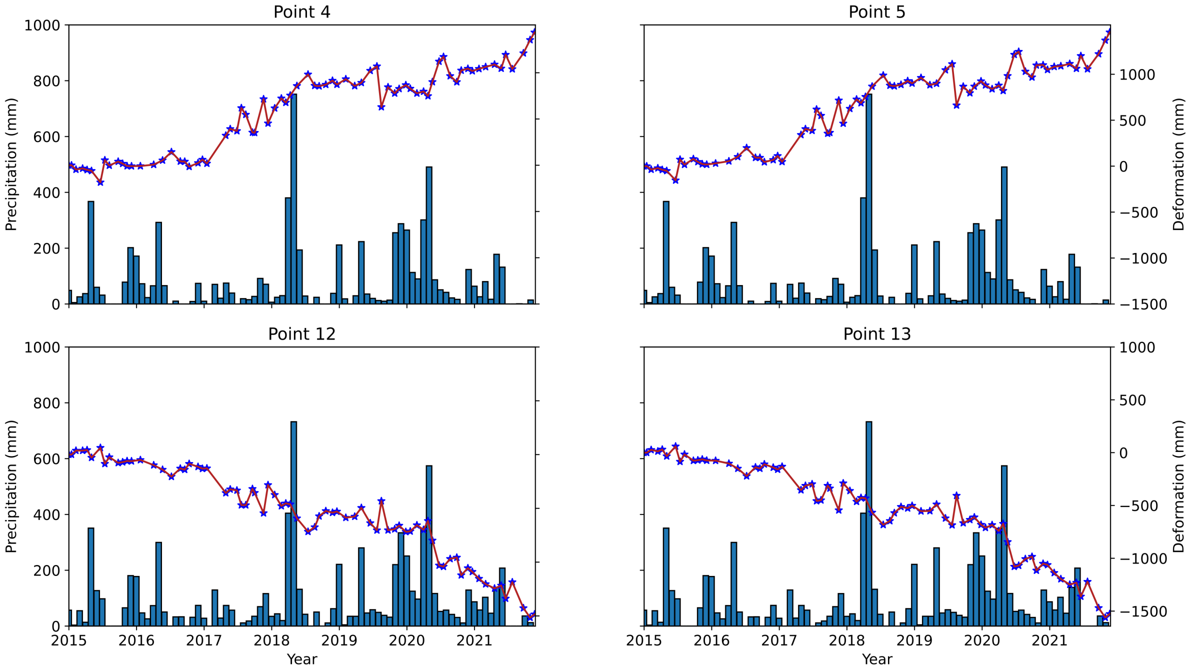

Figure 39: Sentinel-1 Descending derived deformation superimposed on rainfall data. The line graph represents time series deformation while the bar graph represent the amount of precipitation in a particular month

For the ascending node, the correlation coefficients for points 4, 5, 12, and 13 are as follows: -0.14, -0.14, 0.13, and 0.16, respectively. Similarly, for the descending node, the correlation coefficients are: -0.10, -0.10, 0.03, and 0.02 for the same points as illustrated in Figures 40 and 41. These coefficients quantitatively represent the strength and direction of the relationship between precipitation and deformation at each of these points.

These findings offer valuable insights into the impact of rainfall on surface deformation in the study area. However, the unexpected positive correlation coefficients deviate from the typical expectation of a negative correlation, where increased precipitation is usually associated with subsidence. This anomaly suggests the presence of other factors not accounted for in this research that could influence deformation trends. This aspect merits further exploration to enhance the comprehensiveness of landslide susceptibility assessments.

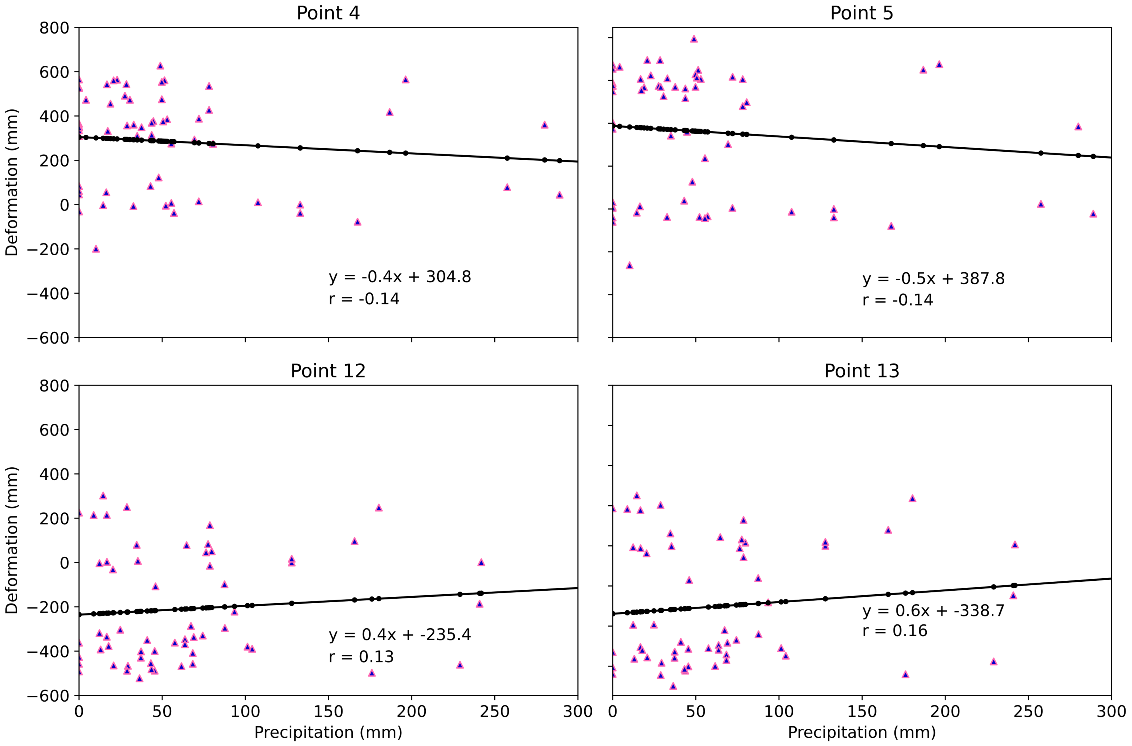

Figure 40: Sentinel-1 Ascending derived time series deformation correlated to rainfall patterns

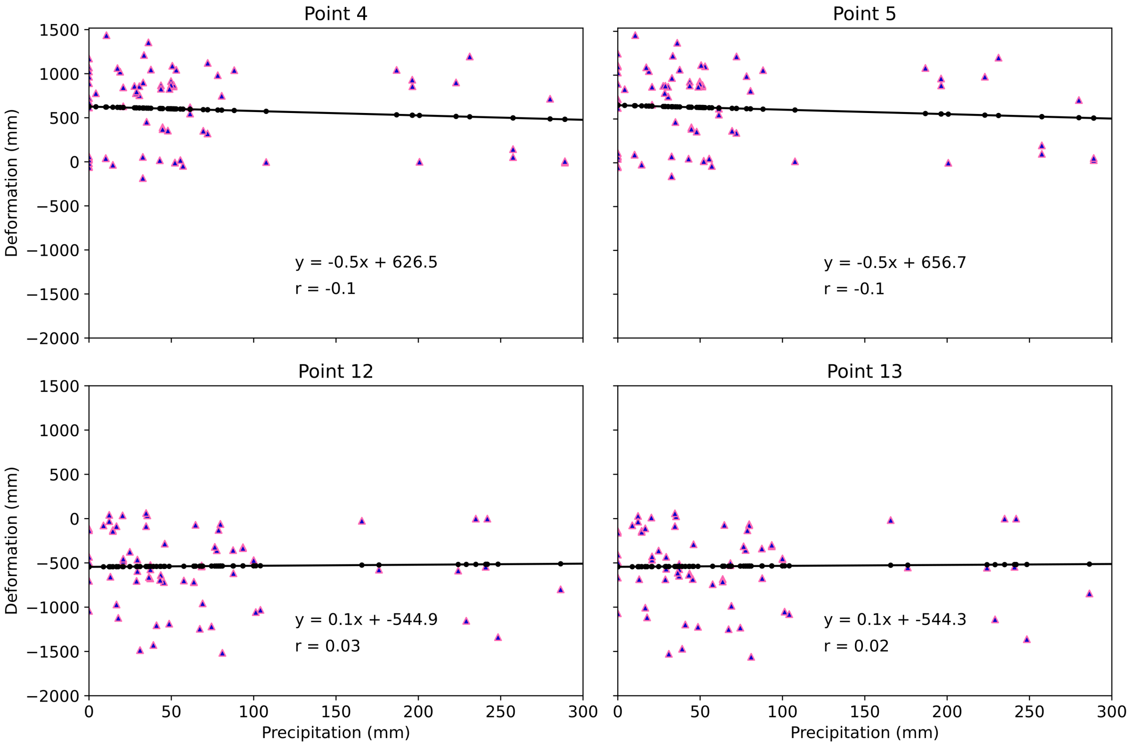

Figure 41: Sentinel-1 Descending derived time series deformation correlated to rainfall patterns

ALOS PALSAR Derived Deformation

In the quest to understand the relationships between deformation and precipitation, the analysis was extended to include deformation data derived from ALOS PALSAR imagery. However, it's crucial to acknowledge certain challenges that influenced this analysis, particularly the scarcity of data from ALOS PALSAR.

Due to limited data availability, only a few time series datasets could be produced from ALOS PALSAR, which inherently impacted the robustness of our correlation analysis. As illustrated in Figure 42, the scarcity of data points from ALOS PALSAR introduces variability and uncertainty into the correlation analysis.

Another challenge arose from the temporal mismatch between ALOS PALSAR imagery acquisitions and the monthly intervals of TAMSAT precipitation data. In contrast to Sentinel-1, where a temporal baseline of 60 days could be applied due to data availability, ALOS PALSAR processing necessitated an extended baseline of up to 875 days to generate sufficient data for time series deformation analysis. Consequently, aligning the relevant precipitation data with specific epochs in the time series deformation became a complex task.

Given these challenges, it is important to approach the correlation analysis between ALOS PALSAR-derived deformation and precipitation with caution. The results of this analysis should receive less weighting or confidence compared to the correlation derived from Sentinel-1-derived deformation, primarily due to data scarcity and temporal mismatches.

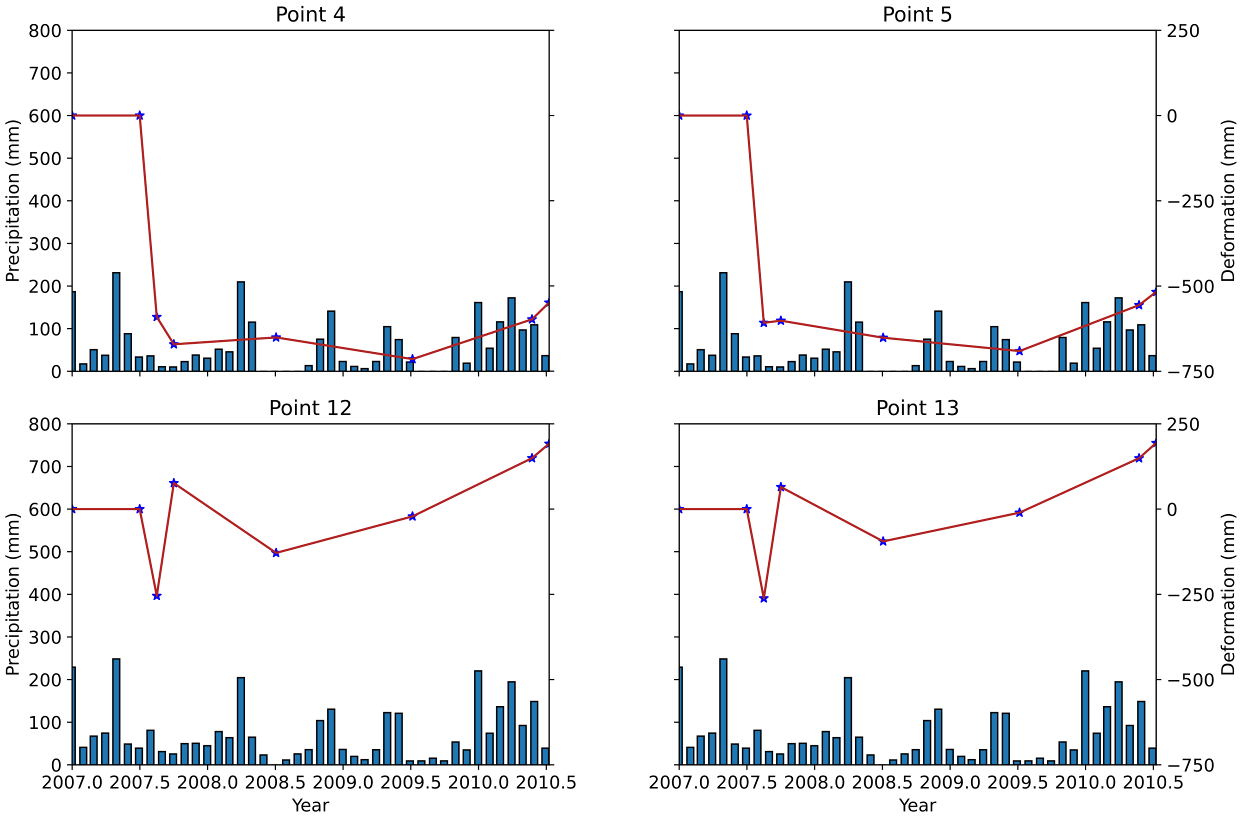

Figure 42: ALOS PALSAR derived deformation superimposed on rainfall data. The line graph represents time series deformation while the bar graph represent the amount of precipitation in a particular month

Surprisingly, the correlation trends for points 4, 5, 12, and 13 in the ALOS PALSAR analysis appear to be in agreement to those derived from Sentinel-1-derived deformation. The correlation coefficients for these points are notably different, with values of -0.82, -0.78, 0.05, and 0.06, respectively, as displayed in Figure 43.

These correlations emphasise the complexity of the relationship between deformation and precipitation, particularly in the context of ALOS PALSAR data.

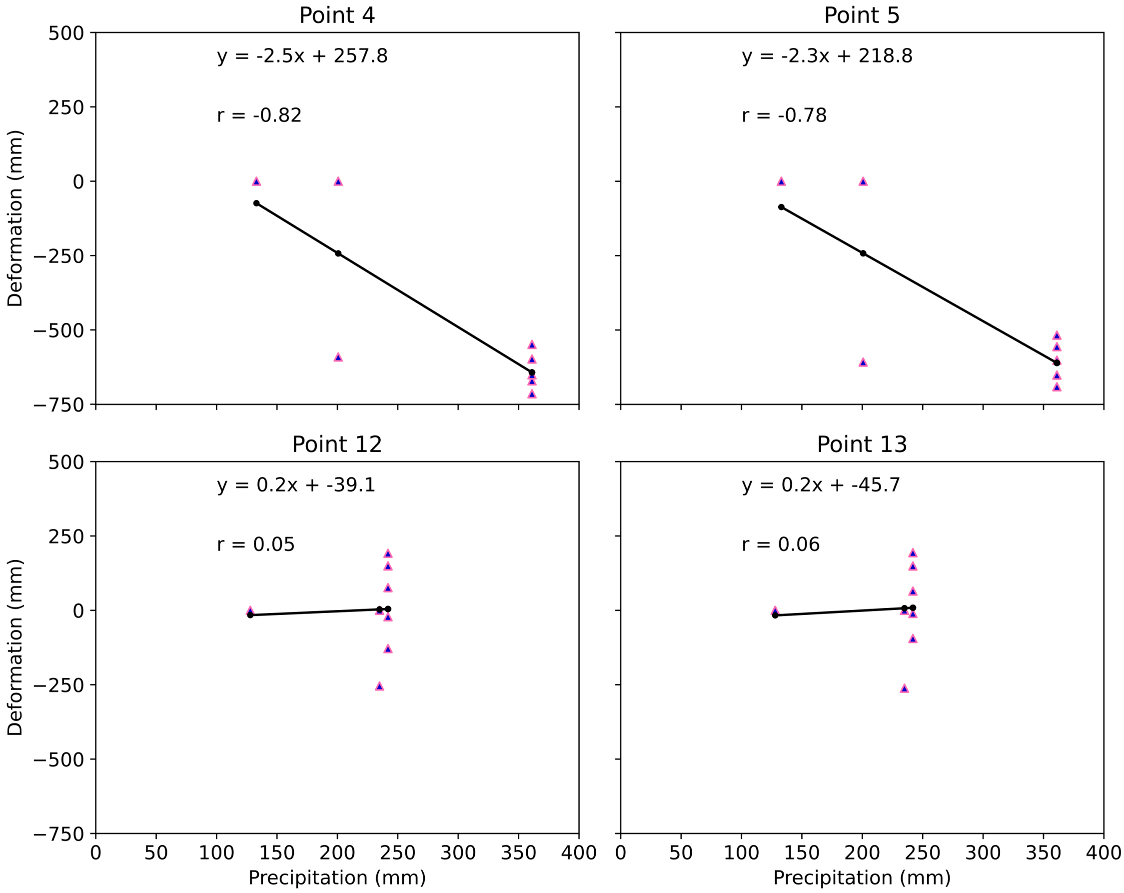

Figure 43: ALOS PALSAR derived time series deformation correlated to rainfall patterns

4.3.2 Geomorphological Factors and Deformation

In the pursuit of a comprehensive understanding of the factors contributing to deformation in the study area, correlation analysis was conducted between deformation and several key geomorphological factors. These factors include elevation, slope, aspect and surface roughness. Datasets from both ALOS PALSAR and Sentinel-1, incorporating all coherent permanent scatterers were utilised in the analysis.

Elevation : The visual representation of this correlation is displayed in Figure 44. For ALOS PALSAR, Sentinel-1 Ascending, and Sentinel-1 Descending, the computed correlation coefficients are -0.18, -0.49 and -0.34 respectively. These negative coefficients indicate a negative correlation, suggesting that as elevation increases, deformation tends to decrease. This implies that higher areas experience less deformation.

Slope : The influence of slope on deformation was also examined. Figure 45 illustrates this relationship. The computed correlation coefficients for ALOS PALSAR, Sentinel-1 Ascending, and Sentinel-1 Descending are -0.01, -0.25 and -0.15 respectively. These coefficients are generally negative, indicating that areas with steeper slopes tend to experience subsidence. However, the correlation is weak in this case.

Aspect : Aspect, representing the direction in which a slope faces, was another factor considered in the analysis. Figure 46 showcases the correlation visualisation. The computed correlation coefficients for ALOS PALSAR, Sentinel-1 Ascending, and Sentinel-1 Descending are 0.09, -0.04 and 0.01 respectively. These coefficients are close to zero, suggesting a weak correlation between aspect and deformation.

Surface Roughness : Lastly, the correlation between surface roughness and deformation was explored, as visualised in Figure 47. The computed correlation coefficients for ALOS PALSAR, Sentinel-1 Ascending and Sentinel-1 Descending are 0.06, -0.12 and -0.08 respectively. While these coefficients are not particularly strong, they indicate a mixed correlation with deformation. The positive coefficient for ALOS PALSAR suggests that areas with higher surface roughness may experience more deformation, while the negative coefficients for Sentinel-1 suggest the opposite.

Based on the results of our correlation analysis, we can rank the geomorphological factors in terms of their influence on deformation, from most to least significant:

Elevation : Elevation appears to have the most substantial influence on deformation, with consistently negative correlation coefficients across all satellite datasets. Higher elevations areas are associated with reduced deformation.

Surface Roughness : Surface roughness follows, although the correlation is not particularly strong. ALOS PALSAR indicates a positive correlation, while Sentinel-1 datasets suggest a negative correlation, making this factor less straight forward to interpret.

Slope : The correlation between slope and deformation is relatively weak, with negative coefficients indicating that steeper slopes tend to subsidence.

Aspect : Aspect shows the weakest correlation with deformation, with coefficients close to zero. The direction in which a slope faces appears to have minimal influence on deformation.

In conclusion, while elevation emerges as the most influential geophysical factor in influencing deformation, it is important to note that deformation is a complex phenomenon influenced by multiple interacting variables. These correlations provide valuable insights into the relationships between geomorphological factors and deformation patterns, contributing to a more comprehensive understanding of the factors driving deformation in the study area.

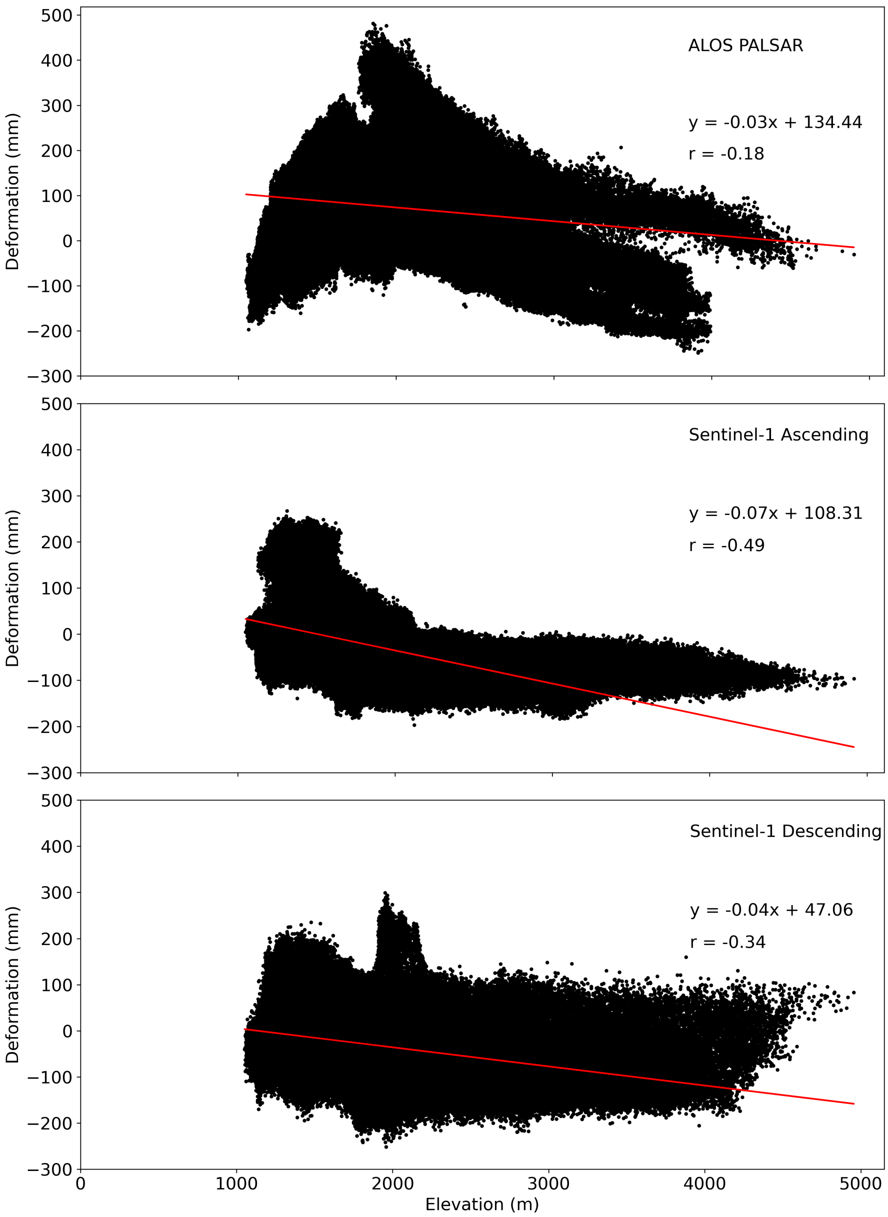

Figure 44: Visualisation of the correlation between Elevation and Deformation

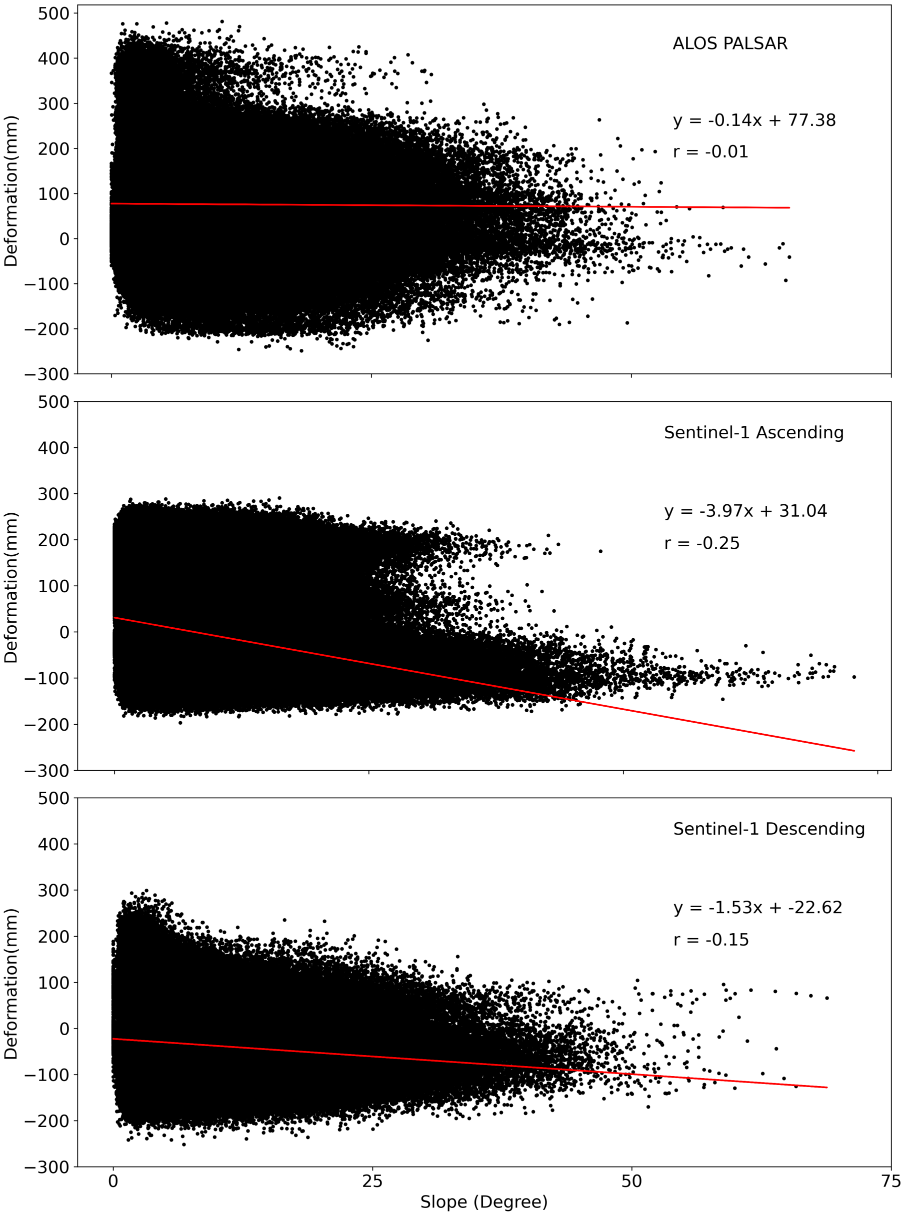

Figure 45: Visualisation of the correlation between Slope and Deformation

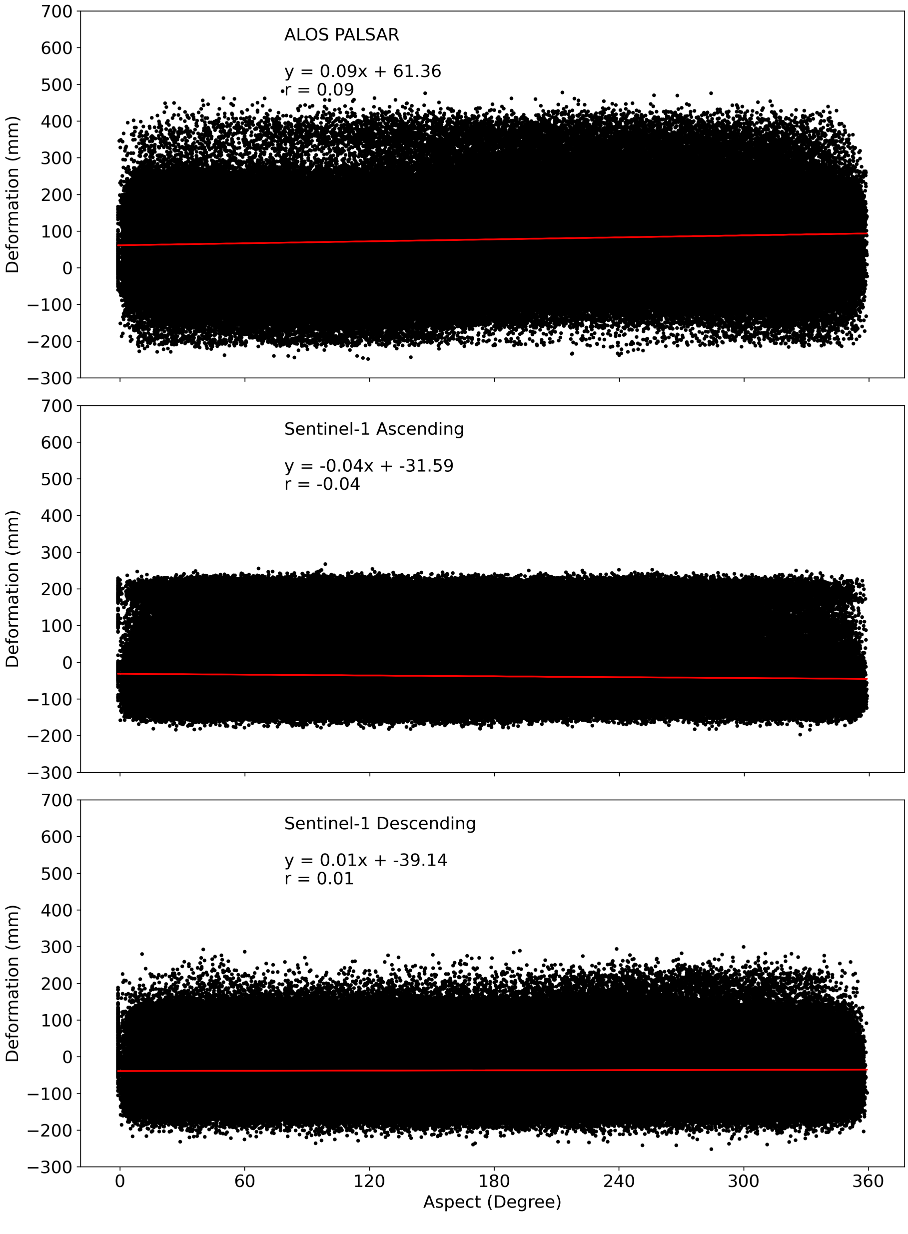

Figure 46: Visualisation of the correlation between Aspect and Deformation

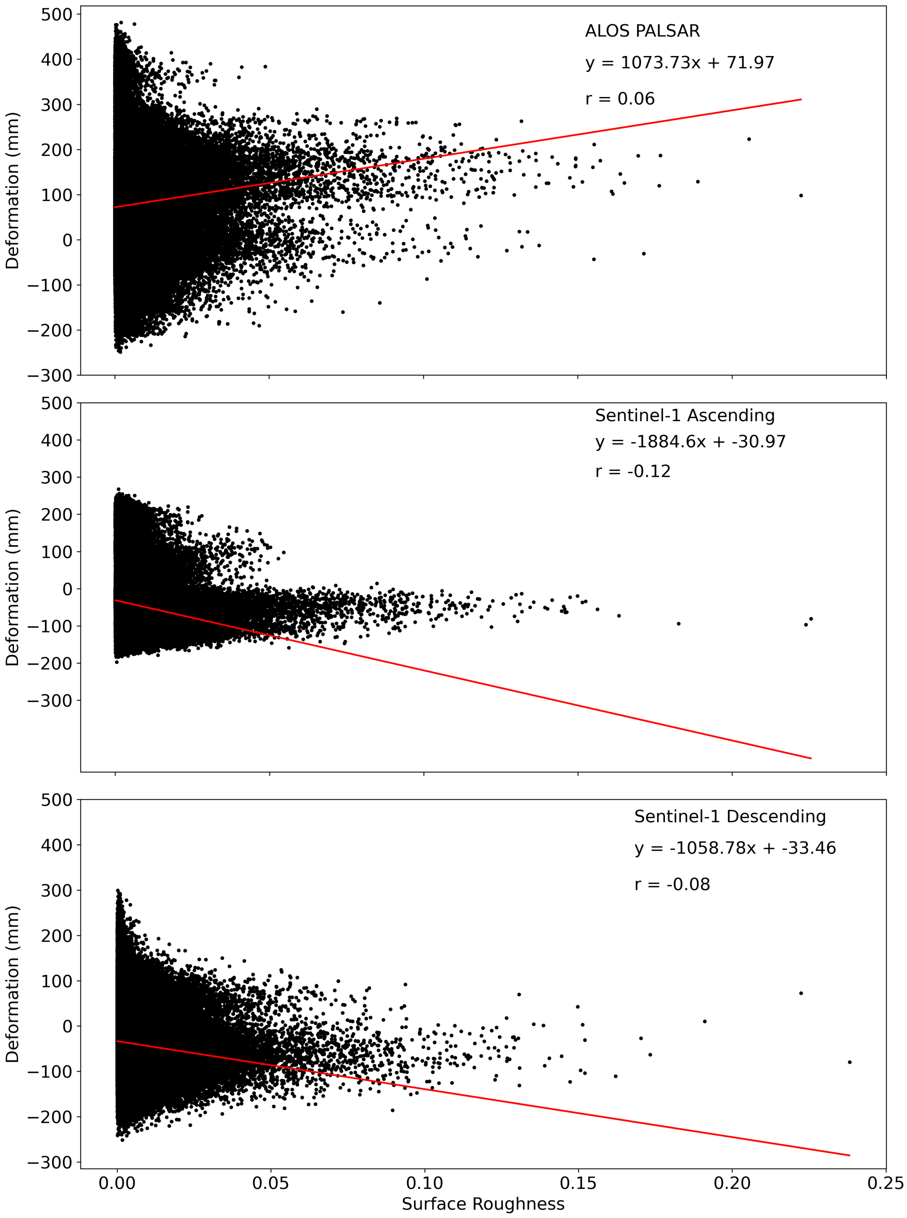

Figure 47: Visualisation of the correlation between Surface Roughness and Deformation

4.3.3 LULC and Deformation

In the comprehensive study of factors influencing deformation patterns and landslide occurrences, the critical role that land use and land cover changes play in these phenomena was recognised. Land use and land cover can undergo seasonal variations, especially during the wet and dry seasons, which can significantly impact deformation patterns.

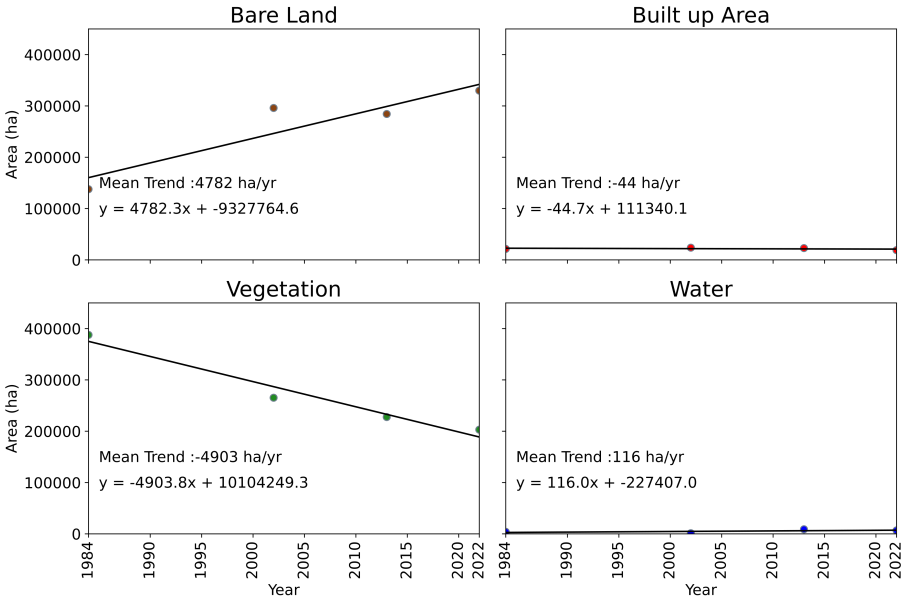

Figure 48: The LULC trend (in hecatres) in the study area during the Dry Season

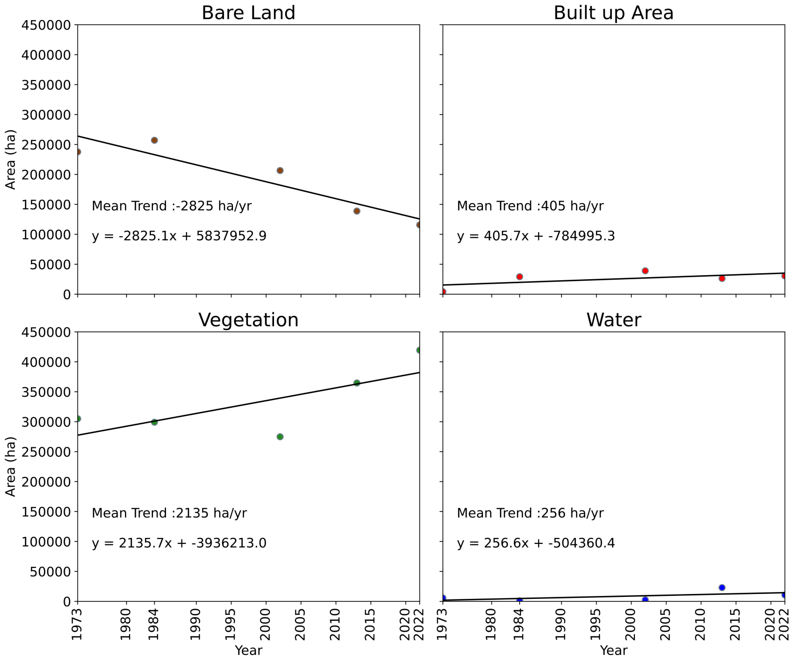

Figure 49: The LULC trend (in hecatres) in the study area during the Wet Season

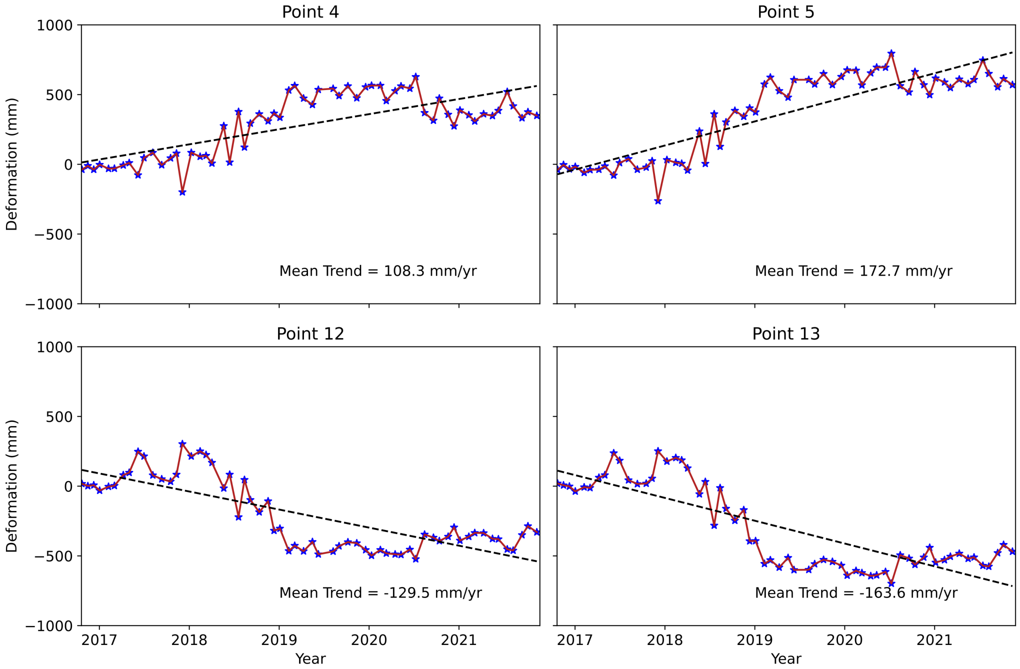

Figure 50: Sentinel-1 Ascending LOS deformation of selected points in the study area

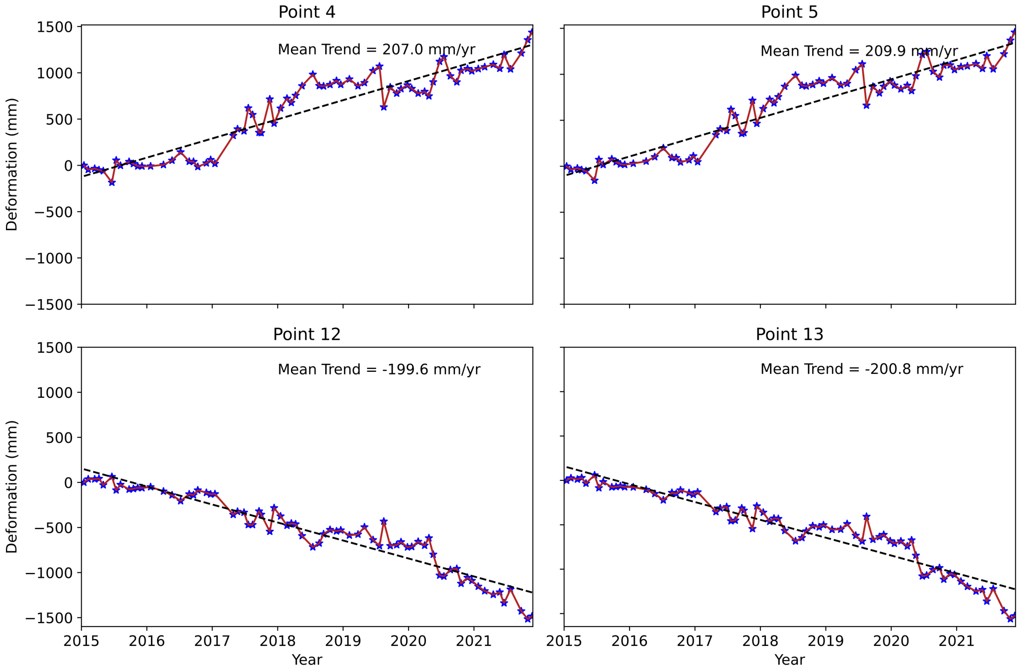

Figure 51: Sentinel-1 Descending LOS deformation of selected points in the study area

To investigate the correlation between changes in land use land cover and deformation trends, changes during the wet and dry seasons were visually represented in Figures 48 and 49. Subsequently, these changes were visually correlated with

Sentinel-1 deformation data in both the ascending and descending nodes, as depicted in Figures 50 and 51.

An intriguing trend emerged from our visualisations, particularly concerning vegetation cover and bare land. During the dry season, there is a noticeable decreasing trend in the land covered by vegetation, while there is a concurrent increase in the land area covered by bare land. Conversely, during the wet season, the trend reverses, with land covered by vegetation increasing and the land covered by bare land decreasing.

This seasonal fluctuation in land use and land cover, particularly the alternation between vegetation and bare land, is of particular interest. It is noteworthy as it is strongly correlated with deformation patterns, as observed in our time series data. Vegetation cover plays a vital role in providing support to slopes, preventing soil erosion, and mitigating mass movements. However, during periods of heavy and extreme rainfall, waterlogging in the soil can also trigger mass movement events, leading to deformation and potential landslides.

Another critical aspect of land use land cover analysis pertains to built-up areas, which can have a direct influence on deformation and landslide occurrences. Two built-up indices, BU and NDBI, were employed to visually correlate deformation patterns with built-up areas. NDBI is used to emphasise built-up areas in urban environments. It is derived from image band maths using the near-infrared and shortwave infrared bands. BU is derived from NDBI and NDVI and is used to highlight urban patterns.

Figure 52 showcases the visual relationship between built-up areas, represented by dark blue regions, and deformation. Intriguingly, it is evident that built-up areas tend to coincide with regions experiencing instability. In the northern part of the study area, where built-up areas are present, subsidence is observed, while in the southern part, built-up areas correspond to areas experiencing uplift.

This correlation suggests that built-up areas may contribute to deformation events. It is essential to recognise that urbanisation and infrastructure development can alter the natural landscape, impacting soil stability and potentially increasing the risk of deformation and landslides.

Additionally, all identified points of interest were systematically examined with respect to lithology, soil, and variations in land use land cover as displayed in Tables 8 and 9. It was observed that all points fall under the category of igneous volcanic lithology and clayey soil. The land use land cover transitions were particularly noteworthy, showing a consistent change from built areas during the dry season to vegetation in the wet season for most points. However, point 4 exhibited unique behaviour, maintaining a constant land cover throughout the epochs. These observations were validated through cross-referencing with Google Earth imagery. The selection of land use land cover epochs was aimed to align approximately with the time series deformation data obtained from Sentinel-1, providing a synchronized view of land surface changes.

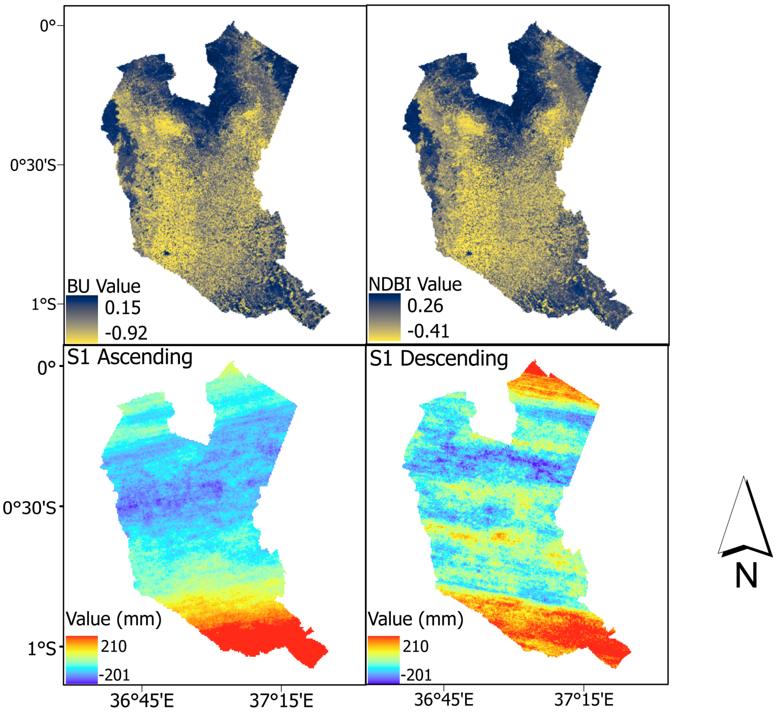

Figure 52: Visualisation of built up area indices and deformation

Table 8: Land use land cover changes over Seasons of selected points in the study area

	Dry Season		Wet Season	
PointID	2013	2022	2013	2022
4	Built Area	Built Area	Built Area	Built Area
5	Built Area	Built Area	Vegetation	Vegetation
12	Built Area	Built Area	Vegetation	Vegetation
13	Built Area	Built Area	Vegetation	Vegetation

Table 9: Lithology and soil types for identified unstable points

PointID	Lithology	Soil
4	Igneous volcanic	Clayey
5	Igneous volcanic	Clayey
12	Igneous volcanic	Clayey
13	Igneous volcanic	Clayey

In summary, the analysis reveals that lithology and soil characteristics as well as changes in land use and land cover, particularly shifts between vegetation and bare land, exhibit a strong correlation with deformation patterns in the study area. The seasonal fluctuations in these land cover types underscore the complex interplay between lithology and soil charactersitics, climatic conditions, vegetation, and deformation. Additionally, the presence of built-up areas is associated with areas experiencing deformation, emphasising the need for careful urban planning and monitoring to mitigate potential geomorphic hazards. These findings contribute to a more comprehensive understanding of the factors influencing deformation and landslide occurrences within the study area.

Chapter 5

Conclusions and Recommendations

5.1 Conclusions

The conclusion section of this dissertation serves as the culmination of an extensive journey through the multifaceted realm of deformation analysis and monitoring, and land use land cover assessment in the study area. The preceding chapters, delved into the complexities of understanding ground movement patterns, the contributing factors, and their implications for landslide susceptibility. This section brings together the key findings, insights, and implications drawn from a diverse array of data sources and analytical techniques. It offers a comprehensive summary of the research's core contributions and underscores their significance in advancing our knowledge of deformation processes and their interactions with the natural environment.

Research Objective i :Quantifying the deformation in the study area has been a central focus of this investigation. The comprehensive analysis conducted using a combination of cutting-edge geospatial techniques and datasets enabled the derivation of precise deformation rates at specific points within the study area. Through InSAR data, detailed LoS deformation rates were obtained, providing millimeter-level accuracy in measuring ground movement. Additionally, the integration of GRACE/GRACE-FO and GLDAS data has furnished us with crucial insights into vertical deformation trends, enhancing our understanding of subsurface processes.

The comparison of deformation rates derived from InSAR, GRACE/GRACE-FO, and GLDAS datasets provides valuable insights into the diverse nature of these measurements. It's important to note that these datasets not only differ in spatial resolution but also exhibit variations in their epoch coverage. InSAR data offer localised measurements with LoS deformation rates, capturing ground movement with millimeter-level precision. In contrast, GRACE/GRACE-FO and GLDAS data provide a broader perspective, focusing on vertical deformation over larger spatial scales.

To illustrate this comparison, Table 5 in Section 4.1.5 presents deformation rates for specific points within the study area, highlighting the disparities between these datasets. These deformation rates have allowed us to quantify the complex patterns of subsidence and uplift across the study area. It is evident that deformation is not uniform but rather exhibits substantial variability, underscoring the multifaceted nature of geomorphic dynamics in this region. By addressing this research objective, we have not only quantified deformation but have also laid the groundwork for a more comprehensive assessment of geomorphic hazards and a better-informed approach to mitigate potential risks.

This quantification of deformation serves as a foundational element in the broader context of geomorphic research and hazard assessment in the study area.

Research Objective ii :Several factors contribute to deformation and landslides in the study area:

Precipitation Patterns: Rainfall, especially during the wet season, appears to be a significant driver of deformation and landslides. High and extreme precipitation events are associated with subsidence events, suggesting that heavy rainfall can trigger mass movements and landslides.

Seasonal Variations in Land Use Land Cover: Seasonal changes in land use and land cover, specifically the alternation between vegetation and bare land, play a crucial role. During the dry season, a decreasing trend in vegetation cover and an increasing trend in bare land are observed, potentially contributing to deformation. Conversely, during the wet season, the opposite trend occurs, with increased vegetation cover and reduced bare land.

Built-Up Areas: The presence of built-up areas, often associated with urbanisation and infrastructure development, appears to be correlated with deformation. Built-up areas can alter the natural landscape, impacting soil stability and contributing to deformation events.

Geomorphological Factors: Geomorphological factors such as elevation, slope, aspect and surface roughness influence deformation. Higher elevations are associated with reduced deformation, suggesting that topography plays a role. Surface roughness can also affect deformation, with mixed correlations observed.

Geology: Geology significantly influences surface characteristics in the study area, with regions featuring igneous volcanic lithology and clayey soils exhibiting more pronounced deformation rates.

In summary, the main causes of deformation and landslides in the study area are likely a combination of climatic factors, seasonal variations in land use land cover, the presence of built-up areas, geology and geomorphological characteristics. These factors interact in complex ways, making it essential to consider multiple variables in landslide susceptibility assessments and deformation studies in the study area.

Research Objective iii : The research objective of investigating the correlation of causative agents of deformation to observed land deformation was pursued through a comprehensive analysis of various factors. Geological characteristics, specifically igneous volcanic lithology and clayey soil, demonstrated a consistent profile across all points of interest as aforementioned in research Objective ii. Simultaneously, the study explored the influence of land use and land cover changes on deformation, revealing a strong correlation between transitions from built areas to vegetation and corresponding deformation patterns.

Furthermore, geomorphological factors, including elevation, slope, aspect, and surface roughness, were examined. The correlation analysis unveiled relationships between these topographic features and deformation trends. Elevation displayed the largest influence while aspect displayed the weakest influence on deformation. Additionally, climatic factors, such as precipitation, were considered, indicating a negative correlation between high rainfall and subsequent subsidence events.

Throughout this study, the research aims have been meticulously pursued and effectively addressed. Research Aim i, focusing on the investigation and quantification of land deformation in landslide-prone areas in Murang'a and Nyeri, is seamlessly integrated into Research Questions i, ii, iii, and iv, along with Research Objective i. Similarly, Research Aim ii, targeting the identification of underlying causal factors for mass movement events in the region, is thoroughly explored through Research Objectives ii and iii. Through a diligent examination of these research aims and objectives, the study has attained its overarching objectives with success. Consequently, the research questions have been comprehensively addressed, resulting in a thorough understanding of landslide induced deformation and their causal factors within the study area.

5.2 Recommendations

The culmination of this extensive research endeavour has yielded valuable insights into deformation processes, land use land cover dynamics, and their interplay within the study area. These findings offer the basis for a series of recommendations aimed at advancing our understanding of geomorphic hazards and deformation thereby enhancing mitigation strategies.

Integration of High-Precision Geodetic Techniques : The research relied on areal deformation monitoring techniques with varying spatial resolutions. While InSAR provided high resolution data, GRACE/GRACE-FO, and GLDAS offered broader coverage at lower spatial resolutions. To further enhance the accuracy of deformation monitoring, it is recommended to employ more precise geodetic methods like GNSS and precise levelling at identified critical points.

These techniques will enable a deeper understanding of ground movement and subsurface processes.

Long Term Monitoring : Given the complex nature of geomorphic processes, long term monitoring is essential to capture evolving trends. Establishing continuous monitoring networks at key deformation points will provide a comprehensive view of ground movement over extended periods. This long term data collection is invaluable for predicting and mitigating potential geomorphic hazards.

Integration of Additional Data Sources : To bolster deformation analysis, integrating data from complementary geospatial sources should be considered. These sources can provide additional geospatial insights and validation for deformation trends.

Enhanced Precipitation Monitoring : As precipitation plays a crucial role in triggering landslides and deformation events, enhancing the monitoring of rainfall patterns is essential. Deploying additional rain gauge stations and weather monitoring instruments within the study area to gather detailed precipitation data, might enable a more precise correlation with deformation patterns.

Interdisciplinary Research : Foster interdisciplinary collaboration among geologists, geophysicists, remote sensing experts, and disaster management professionals. Collaborative efforts can lead to a more holistic understanding of geomorphic hazards and the development of effective mitigation strategies.

By implementing these recommendations, we can enhance our ability to monitor, predict, and mitigate geomorphic hazards, ultimately contributing to the safety and resilience of the study area's communities and infrastructure.

References

Africa Groundwater Atlas (2019). Geological Map of Kenya.
URL: *https://ggis.un-igrac.org/catalogue/#/dataset/1297*

Ajami, H. (2021). Geohydrology: Global Hydrological Cycle, Academic Press, Oxford, pp. 393–398.
URL: *https://www.sciencedirect.com/science/article/pii/B9780124095489123875*

ASF DACC (n.d.). Copernicus Sentinel Data [2015-2021].
URL: *https://search.asf.alaska.edu/#/?zoom=8.270&center=37.440,-2.697&polygon=POLYGON((37.0775 0.001,37.0786 0.0154,37.0253 -0.0469,36.978 -0.0686,36.9857 -0.1327,37.0079 -0.147,37.0194 -0.1737,37.0102 -0.2401,36.9886 -0.2543,36.9983 -0.269,36.9874 -0.2931,36.*

Attia, G. F., Hegazy, M. A. & El-Hameed, A. M. A. (2012). The use of satellite laser observations in studying the crustal movements, *NRIAG Journal of Astronomy and Geophysics* **1**(2): 110–113.
URL: *https://www.sciencedirect.com/science/article/pii/S2090997712000156*

Bekaert, D., Hooper, A. & Wright, T. (2015a). A spatially variable power law tropospheric correction technique for InSAR data, *Journal of Geophysical Research: Solid Earth* **120**(2): 1345–1356.
URL: *https://doi.org/10.1002/2014JB011558*

Bekaert, D. P., Walters, R. J., Wright, T. J., Hooper, A. J. & Parker, D. J. (2015b). Statistical comparison of InSAR tropospheric correction techniques, *Remote Sensing of Environment* **170**: 40–47.
URL: *https://www.sciencedirect.com/science/article/pii/S0034425715301231*

Biggs, J., Anthony, E. Y. & Ebinger, C. J. (2009). Multiple inflation and deflation events at Kenyan volcanoes, East African Rift, *Geology* **37**(11): 979–982.
URL: *https://doi.org/10.1130/G30133A.1*

Biswas, I. (2019). Triangulation vs trilateration vs multilateration - for indoor positioning systesm.

Bogaard, T. A. & Greco, R. (2015). Landslide hydrology: from hydrology to pore pressure, *WIREs Water* **3**(3): 439–459.
URL: *http://dx.doi.org/10.1002/wat2.1126*

Botai, C. M. & Combrinck, L. (2012). Global geopotential models from Satellite Laser Ranging data with geophysical applications: A review, *South African Journal of Science* **108**: 20–29.

Bürgmann, R. & Thatcher, W. (2013). Space geodesy: A revolution in crustal deformation measurements of tectonic processes, *in* M. E. Bickford (ed.), *The Web of Geological Sciences: Advances, Impacts, and Interactions*, Vol. 500, Geological Society of America, p. 0.
URL: *https://doi.org/10.1130/2013.2500(12)*

Chang, F., Dong, S., Yin, H. & Wu, Z. (2022). Using the SBAS InSAR technique to monitor surface deformation in the Kuqa fold-thrust belt, Tarim Basin, NW China, *Journal of Asian Earth Sciences* **231**: 105212.
URL: *https://www.sciencedirect.com/science/article/pii/S1367912022001353*

Chen, J. (2019). Satellite gravimetry and mass transport in the earth system, *Geodesy and Geodynamics* **10**(5): 402–415.
URL: *https://www.sciencedirect.com/science/article/pii/S1674984717301647*

Chen, J., Cazenave, A., Dahle, C., Llovel, W., Panet, I., Pfeffer, J. & Moreira, L. (2022). Applications and Challenges of GRACE and GRACE Follow-On Satellite Gravimetry, *Surveys in Geophysics* **43**(1): 305–345.
URL: *https://doi.org/10.1007/s10712-021-09685-x*

Christodoulidis, D. C., Smith, D. E., Kolenkiewicz, R., Klosko, S. M., Torrence, M. H. & Dunn, P. J. (1985). Observing tectonic plate motions and deformations from satellite laser ranging, *Journal of Geophysical Research* **90**: 9249–9263.

Davies, T. C. (1996). Landslide research in Kenya, *Journal of African Earth Sciences* **23**(4): 541–545.
URL: *https://www.sciencedirect.com/science/article/pii/S0899536297000171*

DiBiase, D. & Dutton, J. A. (n.d.a). 10. Triangulation —The Nature of Geographic Information.
URL: *https://www.e-education.psu.edu/natureofgeoinfo/c5_p11.html*

DiBiase, D. & Dutton, J. A. (n.d.b). 11. Trilateration — The Nature of Geographic Information.
URL: *https://www.e-education.psu.edu/natureofgeoinfo/c5_p12.html*

Dindi, E. (2015). An assessment of the performance of the geophysical methods as a tool for the detection of zones of potential subsidence in the area southwest of Nakuru town, Kenya, *Environmental Earth Sciences* **73**(7): 3643–3653.
URL: *https://doi.org/10.1007/s12665-014-3647-1*

Dubache, G., Asmerom, B., Ullah, W., Ogwang, B. A., Amiraslani, F., Weijun, Z. & Gul, C. (2021). Testing the accuracy of high-resolution satellite-based and numerical model output precipitation products over Ethiopia, *Theoretical and Applied Climatology* **146**(3): 1127–1142.
URL: *https://doi.org/10.1007/s00704-021-03783-x*

El-Ashmawy, K. L. A. (2019). A Simple Methodology for Monitoring and Analysis of Vertical Displacement of Buildings, *American Scientific Research Journal for Engineering, Technology, and Sciences (ASRJETS)* **60**(1): 83–92.

EoPortal (2023). Copernicus: Sentinel-1.
URL: *https://www.eoportal.org/satellite-missions/copernicus-sentinel-1#sas-sar-antenna-subsystem*

Erol, S., Erol, B. & Ayan, T. (2004). A general review of the deformation monitoring techniques and a case study: Analysing deformations using GPS/levelling.

Farr, T. G. & Kobrick, M. (2000). Shuttle Radar Topography Mission produces a wealth of data, *Eos, Transactions American Geophysical Union* **81**(48): 583–585.

Farr, T. G., Rosen, P. A., Caro, E., Crippen, R., Duren, R., Hensley, S., Kobrick, M., Paller, M., Rodriguez, E. & Roth, L. (2007). The shuttle radar topography mission, *Reviews of geophysics* **45**(2).

Farrell, W. E. (1972). Deformation of the Earth by surface loads, *Reviews of Geophysics* **10**: 761–797.
URL: *https://agupubs.onlinelibrary.wiley.com/doi/pdf/10.1029/RG010i003p00761*

Flechtner, F., Reigber, C., Rummel, R. & Balmino, G. (2021). Satellite Gravimetry: A Review of Its Realization, *Surveys in Geophysics* **42**(5): 1029–1074.
URL: *https://doi.org/10.1007/s10712-021-09658-0*

Foumelis, M., Blasco, J. M. D., Desnos, Y. L., Engdahl, M., Fernandez, D., Veci, L., Lu, J. & Wong, C. (2018). Esa Snap - Stamps Integrated Processing for Sentinel-1 Persistent Scatterer Interferometry, *IGARSS 2018 - 2018 IEEE International Geoscience and Remote Sensing Symposium*, pp. 1364–1367.

Giardino, J. R., Regmi, N. R. & Vitek, J. D. (2011). Rock Glaciers, *in* V. P. Singh, P. Singh & U. K. Haritashya (eds), *Encyclopedia of Snow, Ice and Glaciers*, Springer Netherlands, Dordrecht, pp. 943–948.
URL: *https://doi.org/10.1007/978-90-481-2642-2_453*

Gido, N. A. A., Bagherbandi, M. & Nilfouroushan, F. (2020). Localized Subsidence Zones in Gävle City Detected by Sentinel-1 PSI and Leveling Data.
URL: *https://www.mdpi.com/2072-4292/12/16/2629*

Godah, W. (2019). IGiK–TVGMF: A MATLAB package for computing and analysing temporal variations of gravity/mass functionals from GRACE satellite based global geopotential models, *Computers & Geosciences* **123**: 47–58.
URL: *https://www.sciencedirect.com/science/article/pii/S0098300418303418*

Gong, W., Thiele, A., Hinz, S., Meyer, F. J., Hooper, A. & Agram, P. S. (2016). Comparison of Small Baseline Interferometric SAR Processors for Estimating Ground Deformation.

Greco, R., Marino, P. & Bogaard, T. A. (2023). Recent advancements of landslide hydrology, *WIREs Water* .
URL: *http://dx.doi.org/10.1002/wat2.1675*

Grgić, M. & Bašić, T. (2021). Radar Satellite Altimetry in Geodesy - Theory, Applications and Recent Developments, IntechOpen, Rijeka, p. Ch. 5.
URL: *https://doi.org/10.5772/intechopen.97349*

Guerra, A. J. T., Fullen, M. A., Jorge, M. d. C. O., Bezerra, J. F. R. & Shokr, M. S. (2017). Slope Processes, Mass Movement and Soil Erosion: A Review, *Pedosphere* **27**(1): 27–41.
URL: *https://www.sciencedirect.com/science/article/pii/S1002016017602947*

Guo, J., Zhou, L., Yao, C. & Hu, J. (2016). Surface Subsidence Analysis by Multi-Temporal InSAR and GRACE: A Case Study in Beijing.

Highland, L. M. & Bobrowsky, P. T. (2008). The Landslide Handbook - A Guide to Understanding Landslides, U.S Geological Survey, Reston, Virginia.
URL: *https://pubs.usgs.gov/circ/1325/*

Hooper, A. (2008). A multi-temporal InSAR method incorporating both persistent scatterer and small baseline approaches, *Geophysical Research Letters* **35**(16).

Hooper, A., Bekaert, D., Spaans, K. & Arıkan, M. (2012). Recent advances in SAR interferometry time series analysis for measuring crustal deformation, *Tectonophysics* **514-517**: 1–13.
URL: *https://www.sciencedirect.com/science/article/pii/S0040195111004343*

Hwang, C., Yang, Y., Kao, R., Han, J., Shum, C. K., Galloway, D. L., Sneed, M., Hung, W.-C., Cheng, Y.-S. & Li, F. (2016). Time-varying land subsidence detected by radar altimetry: California, Taiwan and north China, *Scientific Reports* **6**(1): 28160.
URL: *https://doi.org/10.1038/srep28160*

ICPAC (2017). Kenya - Soil.
URL: *https://geoportal.icpac.net/layers/data0:geonode:soils*

Ince, E. S., Barthelmes, F., Reißland, S., Elger, K., Förste, C., Flechtner, F. & Schuh, H. (2019). ICGEM – 15 years of successful collection and distribution of global gravitational models, associated services, and future plans, *Earth System Science Data* **11**(2): 647–674.
URL: *https://essd.copernicus.org/articles/11/647/2019/*

Jawan, J., Musa, T. A., Wan Aris, W. A., Putit, R., Abdillah, R. & Mohamad Usop, M. I. (2023). Borneo triangulation 1968: a review and the way forward, *Survey Review* pp. 1–12.
URL: *https://doi.org/10.1080/00396265.2023.2207327*

JAXA/METI (n.d.). ALOS PALSAR L1.1 Complex 2007.
URL: *https://search.asf.alaska.edu/#/?zoom=9.970&center=36.408,-0.432&flightDirs=Ascending&polygon=POLYGON((37.0775 0.001,37.0786*

0.0154,37.0253 -0.0469,36.978 -0.0686,36.9857 -0.1327,37.0079 -0.147,37.0194 -0.1737,37.0102 -0.2401,36.9886 -0.2543,36.9983 -0.26

King, M. A., Altamimi, Z., Boehm, J., Bos, M., Dach, R., Elosegui, P., Fund, F., Hernández-Pajares, M., Lavallee, D., Mendes Cerveira, P. J., Penna, N., Riva, R. E. M., Steigenberger, P., van Dam, T., Vittuari, L., Williams, S. & Willis, P. (2010). Improved Constraints on Models of Glacial Isostatic Adjustment: A Review of the Contribution of Ground-Based Geodetic Observations, *Surveys in Geophysics* **31**(5): 465–507.
URL: *https://doi.org/10.1007/s10712-010-9100-4*

Kirui, P. K., Riedel, B. & Gerke, M. (2023). Determination of anthropologically induced deformation along the Kenyan Rift system using Multitemporal InSAR analysis with Sentinel-1 data.
URL: *http://dx.doi.org/10.5194/egusphere-egu23-12996*

Kirui, P., Oiro, S., Waithaka, H., Odera, P., Riedel, B. & Gerke, M. (2022). Detection, characterization, and analysis of land subsidence in Nairobi using InSAR, *Natural Hazards* **113**(1): 213–236.
URL: *https://doi.org/10.1007/s11069-022-05296-w*

Knapen, A., Kitutu, M. G., Poesen, J., Breugelmans, W., Deckers, J. & Muwanga, A. (2006). Landslides in a densely populated county at the footslopes of Mount Elgon (Uganda): Characteristics and causal factors, *Geomorphology* **73**(1): 149–165.
URL: *https://www.sciencedirect.com/science/article/pii/S0169555X05002060*

Kobrick, M. (2006). On the toes of giants-How SRTM was born, *Photogrammetric Engineering and Remote Sensing* **72**(3): 206–210.

Koros, W. K. & Agustin, F. (2017). Subsidence surveys at Olkaria geothermal field, Kenya, *Journal of Spatial Science* **62**(1): 195–205.
URL: *https://doi.org/10.1080/14498596.2016.1191386*

Larson, K. M. (1995). Crustal deformation, *Reviews of Geophysics* **33**(S1): 371–377.
URL: *https://agupubs.onlinelibrary.wiley.com/doi/abs/10.1029/95RG00439*

Li, B., Rodell, M., Kumar, S., Beaudoing, H. K., Getirana, A., Zaitchik, B. F., de Goncalves, L. G., Cossetin, C., Bhanja, S., Mukherjee, A., Tian, S., Tangdamrongsub, N., Long, D., Nanteza, J., Lee, J., Policelli, F., Goni, I. B., Daira, D., Bila, M., de Lannoy, G., Mocko, D., Steele-Dunne, S. C., Save, H. & Bettadpur, S. (2019). Global GRACE Data Assimilation for Groundwater and Drought Monitoring: Advances and Challenges, *Water Resources Research* **55**(9): 7564–7586.
URL: *https://doi.org/10.1029/2018WR024618*

Li, Z., Yue, J., Li, W., Lu, D. & Li, X. (2017). A comparison of hydrological deformation using GPS and global hydrological model for the Eurasian plate, *Advances in Space Research* **60**(3): 587–596.
URL: *https://www.sciencedirect.com/science/article/pii/S0273117717303034*

Maidment, R. I., Grimes, D., Allan, R. P., Tarnavsky, E., Stringer, M., Hewison, T., Roebeling, R. & Black, E. (2014). The 30 year TAMSAT African Rainfall Climatology And Time series (TARCAT) data set, *Journal of Geophysical Research: Atmospheres* **119**(18).
URL: *http://dx.doi.org/10.1002/2014JD021927*

Maidment, R. I., Grimes, D., Black, E., Tarnavsky, E., Young, M., Greatrex, H., Allan, R. P., Stein, T., Nkonde, E., Senkunda, S. & Alcántara, E. M. U. (2017). A new, long-term daily satellite-based rainfall dataset for operational monitoring in Africa, *Scientific Data* **4**(1): 170063.
URL: *https://doi.org/10.1038/sdata.2017.63*

Maina, C. G., Kipseba, E. K. & Masibo, M. (2013). Chapter 20 - Overview of Landslide Occurrences in Kenya: Causes, Mitigation, and Challenges, *in* P. Paron, D. O. Olago & C. T. B. T. D. i. E. S. P. Omuto (eds), *Kenya: A Natural Outlook*, Vol. 16, Elsevier, pp. 293–314.
URL: *https://www.sciencedirect.com/science/article/pii/B9780444595591000207*

Marshak, S. (2015). Unsafe Ground: Landslides and Other Mass Movements, *in* E. Svendsen, R. Goodman, L. Thomas & S. Hwang (eds), *Earth: Portrait of a Planet*, 5th edn, W.W Norton & Company, Inc., New York, chapter 16, pp. 586–613.

Murang'a County Government (2021). County Annual Development Plan 2022/2023, *Technical report*, Murang'a County Government.

Navidi, W., Murphy, W. S. & Hereman, W. (1998). Statistical methods in surveying by trilateration, *Computational Statistics & Data Analysis* **27**(2): 209–227.
URL: *https://www.sciencedirect.com/science/article/pii/S0167947397000534*

Ngecu, W. M. & Mathu, E. M. (1999). The El-Nino-triggered landslides and their socioeconomic impact on Kenya, *Environmental Geology* **38**(4): 277–284.
URL: *https://doi.org/10.1007/s002540050425*

Ngecu, W. M., Nyamai, C. M. & Erima, G. (2004). The extent and significance of mass-movements in Eastern Africa: case studies of some major landslides in Uganda and Kenya, *Environmental Geology* **46**(8): 1123–1133.
URL: *https://doi.org/10.1007/s00254-004-1116-y*

Nickola, M., Krásná, H., Combrinck, L., Böhm, J. & De Witt, A. (2023). Hartebeesthoek Radio Astronomy Observatory (HartRAO) antenna axis offset determined by geodetic VLBI analysis and ground survey, *South African Journal of Geomatics* **12**(1): 98–111.
URL: *http://dx.doi.org/10.4314/sajg.v12i1.7*

Nie, J., Tian, J., Guo, X., Wang, B., Liu, X., Cheng, Y. & Jiao, P. (2023). Vertical deformation analysis based on combined adjustment for GNSS and leveling data, *Geodesy and Geodynamics* **14**(5): 477–484.
URL: *https://www.sciencedirect.com/science/article/pii/S1674984723000320*

Njiraini, J., Okaka, F. & Omondi, P. (2022). Landslide Disasters' Causal/Trigger Factors as Understood by the Indigenous People in Murang'a County, Kenya, *Journal of Geography, Environment and Earth Science International* **26**(1 SE - Original Research Article): 5–16.
URL: *https://journaljgeesi.com/index.php/JGEESI/article/view/588*

Nyeri County Government (2022). Annual Development Plan Financial Year 2022/2023, *Technical report*, County Government of Nyeri.

Ogundare, J. O. (2015). *Precision Surveying: The Principles and Geomatics Practice*, John Wiley & Sons, Inc., Hoboken, New Jersey.
URL: *https://doi.org/10.1002/9781119147770*

Omali, T. U. (2022). Assessment of Crustal Deformation in Earthquake Process: An Overview, *Asian Journal of Geological Research* **5**(1): 1–10.
URL: *https://journalajoger.com/index.php/AJOGER/article/view/76*

Owczarz, K. (2020). A review of geodetic and remote sensing methods used for detecting surface displacements caused by mining, *IOP Conference Series: Earth and Environmental Science* **609**(1): 12076.
URL: *http://dx.doi.org/10.1088/1755-1315/609/1/012076*

Potin, P., Rosich, B., Grimont, P., Miranda, N., Shurmer, I., O'Connell, A., Torres, R. & Krassenburg, M. (2016). Sentinel-1 mission status, *Proceedings of EUSAR 2016: 11th European conference on synthetic aperture radar*, VDE, pp. 1–6.

Rosenqvist, A., Shimada, M. & Watanabe, M. (2004). ALOS PALSAR: Technical outline and mission concepts, *4th International symposium on Retrieval of Bio- and geophysical parameters from SAR data for land applications*, Innsbruck, Austria, pp. 1–7.

Sahadevan, D. K. & Pandey, A. K. (2021). DInSAR-based monitoring of land subsidence related to groundwater over-exploitation: example from developing urban center of Nairobi, Kenya, *Hydrogeology Journal* **29**(7): 2461–2473.
URL: *https://doi.org/10.1007/s10040-021-02384-2*

Sánchez, L., Pearlman, M., Kosuke, H. & International Doris Service (n.d.). DORIS.
URL: *https://ggos.org/item/doris/#learn-this*

Scaioni, M., Marsella, M., Crosetto, M., Tornatore, V. & Wang, J. (2018). Geodetic and Remote-Sensing Sensors for Dam Deformation Monitoring, *Sensors* **18**(11): 3682–3706.
URL: *https://doi.org/10.3390/s18113682*

Shafiei Joud, M. S., Sjöberg, L. E. & Bagherbandi, M. (2017). Use of GRACE data to detect the present land uplift rate in Fennoscandia, *Geophysical Journal International* **209**(2): 909–922.
URL: *https://doi.org/10.1093/gji/ggx063*

Shimoda, H. & Kimura, T. (2018). Japanese Space Program.

Steckler, M. S., Nooner, S. L., Akhter, S. H., Chowdhury, S. K., Bettadpur, S., Seeber, L. & Kogan, M. G. (2010). Modeling Earth deformation from monsoonal flooding in Bangladesh using hydrographic, GPS, and Gravity Recovery and Climate Experiment (GRACE) data, *Journal of Geophysical Research: Solid Earth* **115**(B8).
URL: *https://doi.org/10.1029/2009JB007018*

Stefano, F. D., Cuevas-González, M., Luzi, G. & Malinverni, E. S. (2022). Assessing Levelling and DInSAR for Deformation Monitoring in Seismic Region, *The International Archives of the Photogrammetry, Remote Sensing and Spatial Information Sciences* .
URL: *https://api.semanticscholar.org/CorpusID:249257136*

Tarnavsky, E., Grimes, D., Maidment, R., Black, E., Allan, R. P., Stringer, M., Chadwick, R. & Kayitakire, F. (2014). Extension of the TAMSAT Satellite-Based Rainfall Monitoring over Africa and from 1983 to Present, *Journal of Applied Meteorology and Climatology* **53**(12): 2805–2822.
URL: *http://dx.doi.org/10.1175/JAMC-D-14-0016.1*

Torres, R., Snoeij, P., Geudtner, D., Bibby, D., Davidson, M., Attema, E., Potin, P., Rommen, B., Floury, N., Brown, M., Traver, I. N., Deghaye, P., Duesmann, B., Rosich, B., Miranda, N., Bruno, C., L'Abbate, M., Croci, R., Pietropaolo, A., Huchler, M. & Rostan, F. (2012). GMES Sentinel-1 mission, *Remote Sensing of Environment* **120**: 9–24.
URL: *https://www.sciencedirect.com/science/article/pii/S0034425712000600*

USGS (n.d.a). LandSat Imagery.
URL: *https://earthexplorer.usgs.gov/*

USGS (n.d.b). Landsat Satellite Missions — U.S. Geological Survey.

Varnes, D. J. (1958). Landslide Types and Processes, *Landslides and Engineering Practice* (29): 20–47.
URL: *http://onlinepubs.trb.org/Onlinepubs/sr/sr29/29-003.pdf*

Wouters, B., Bonin, J. A., Chambers, D. P., Riva, R. E. M., Sasgen, I. & Wahr, J. (2014). GRACE, time-varying gravity, Earth system dynamics and climate change, *Reports on Progress in Physics* **77**(11): 116801.
URL: *http://dx.doi.org/10.1088/0034-4885/77/11/116801*

Wulder, M. A., Loveland, T. R., Roy, D. P., Crawford, C. J., Masek, J. G., Woodcock, C. E., Allen, R. G., Anderson, M. C., Belward, A. S., Cohen, W. B., Dwyer, J., Erb, A., Gao, F., Griffiths, P., Helder, D., Hermosilla, T., Hipple, J. D., Hostert, P., Hughes, M. J., Huntington, J., Johnson, D. M., Kennedy, R., Kilic, A., Li, Z., Lymburner, L., McCorkel, J., Pahlevan, N., Scambos, T. A., Schaaf, C., Schott, J. R., Sheng, Y., Storey, J., Vermote, E., Vogelmann, J., White, J. C., Wynne, R. H. & Zhu, Z. (2019). Current status of Landsat program, science, and applications, *Remote Sensing of Environment* **225**: 127–147.
URL: *https://www.sciencedirect.com/science/article/pii/S0034425719300707*

Xue, L., Fu, Y. & Martens, H. R. (2021). Seasonal hydrological loading in the Great Lakes region detected by GNSS: a comparison with hydrological models, *Geophysical Journal International* **226**(2): 1174–1186.
URL: *https://doi.org/10.1093/gji/ggab158*

Yang, Y.-J., Hwang, C., Hung, W.-C., Fuhrmann, T., Chen, Y.-A. & Wei, S.-H. (2019). Surface Deformation from Sentinel-1A InSAR: Relation to Seasonal Groundwater Extraction and Rainfall in Central Taiwan.
URL: *https://www.mdpi.com/2072-4292/11/23/2817*

Zhang, Z.-S., Yang, Y.-X., Sun, H.-R., Zhang, Z.-F. & You, X.-Q. (1998). Joint solution of leveling and gravity data in crustal deformation monitoring, *Acta Seismologica Sinica* **11**(1): 89–101.
URL: *https://doi.org/10.1007/BF02650459*

Zhou, S., Zhou, S. & Tan, X. (2020). Nationwide susceptibility mapping of landslides in Kenya using the fuzzy analytic hierarchy process model, *Land* **9**(12): 1–22.
URL: *https://www.mdpi.com/2073-445X/9/12/535*

Zulkifli, N. A., Md Din, A. H. & Md Som, Z. A. (2018). Vertical land motion quantification using space-based geodetic methods: a review, *IOP Conference Series: Earth and Environmental Science* **169**: 12024.
URL: *http://dx.doi.org/10.1088/1755-1315/169/1/012024*

Appendix A

Interferometric Baselines

A.1 Sentinel-1 Ascending

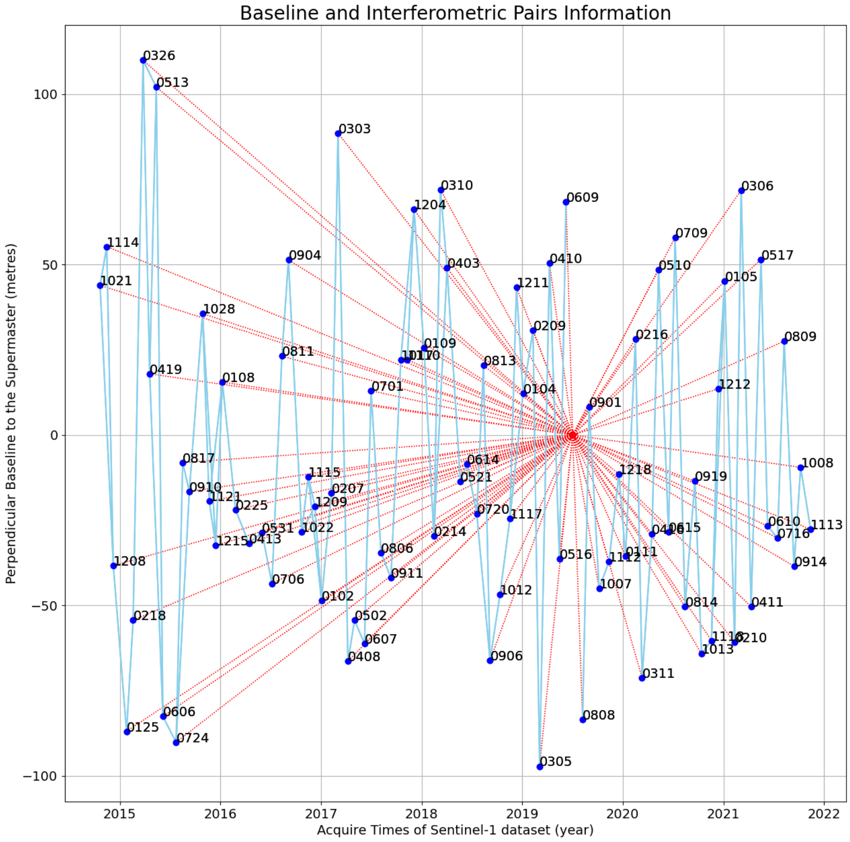

Figure 53: Sentinel-1 Ascending temporal and perpendicular baselines

A.2 Sentinel-1 Descending

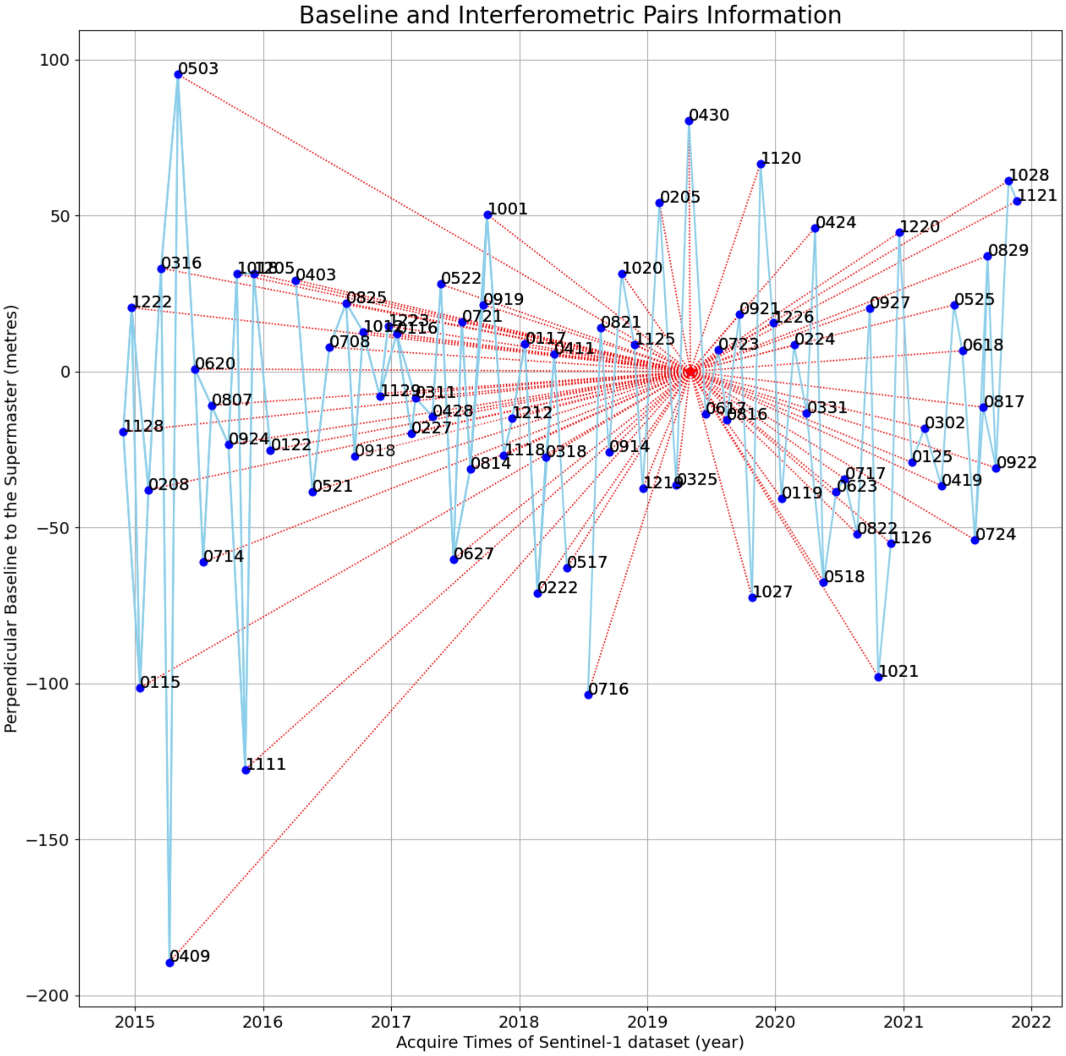

Figure 54: Sentinel-1 Descending temporal and perpendicular baselines

A.3 ALOS PALSAR

A.3.1 Path 565

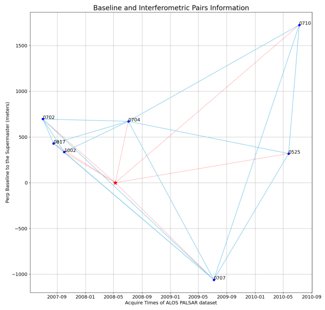

Figure 55: ALOS PALSAR frame 7180 temporal and perpendicular baselines

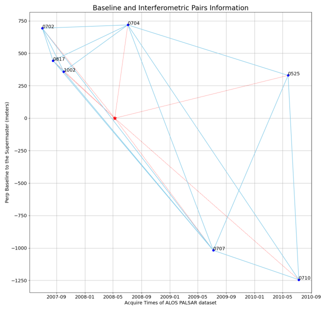

Figure 56: ALOS PALSAR frame 7170 temporal and perpendicular baselines

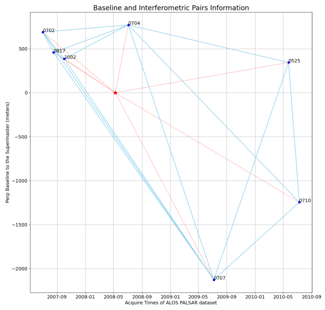

Figure 57: ALOS PALSAR frame 7160 temporal and perpendicular baselines

A.3.2 Path 569

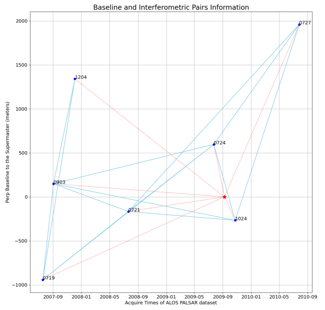

Figure 58: ALOS PALSAR frame 7180 temporal and perpendicular baselines

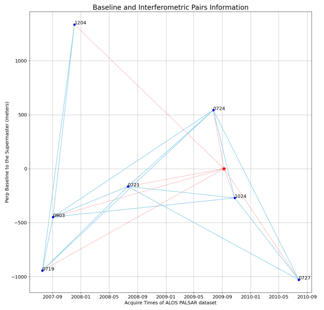

Figure 59: ALOS PALSAR frame 7170 temporal and perpendicular baselines

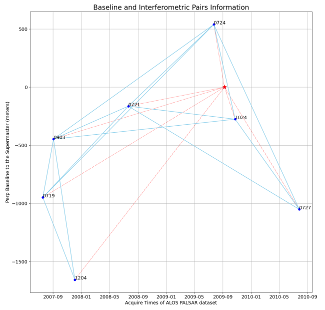

Figure 60: ALOS PALSAR frame 7160 temporal and perpendicular baselines

Appendix B

Computer Programs

B.0.1 Figures 7 and 8

```
# -*- coding: utf-8 -*-
"""
Created on Wed Nov  2 18:56:22 2022

@author: YMBALE001
"""
import pandas as pd
import cartopy.crs as ccrs
import cartopy.feature as cfeature
import matplotlib.pyplot as plt
from matplotlib_scalebar.scalebar import ScaleBar
import numpy as np


plt.rcParams['figure.figsize'] = [12, 16]
fig, axs = plt.subplots(7, 2)
gs = axs[0, 0].get_gridspec()

# remove the underlying axes
for ax in axs[0:3,0]:
    ax.remove()
axbig = fig.add_subplot(gs[0:3:,0], projection = ccrs.PlateCarree()
                                  )
axbig.set_extent([33.5, 42.5, -6, 6])
axbig.add_feature(cfeature.LAND)
axbig.add_feature(cfeature.OCEAN)
axbig.add_feature(cfeature.BORDERS, linestyle=":", edgecolor = '
                                  grey')
axbig.add_feature(cfeature.LAKES, alpha = 0.5)
axbig.add_feature(cfeature.RIVERS)
gl = axbig.gridlines(draw_labels = True, alpha = 0.3, xlocs = [30.5
                                  , 33.5, 36.5, 39.5, 42.5, 45.5],
              ylocs = [-6, -3, 0, 3, 6])
gl.right_labels = False
gl.top_labels = False
gl.xlabel_style= {'size': 12}
gl.ylabel_style= {'size': 12}
```

```
axbig.text(35, 4.5, "1", fontsize = 16, color = 'red')
axbig.text(35, 1.5, "2", fontsize = 16, color = 'red')
axbig.text(35, -1.5, "3", fontsize = 16, color = 'red')
axbig.text(38, 4.5, "4", fontsize = 16, color = 'red')
axbig.text(38, 1.5, "5", fontsize = 16, color = 'red')
axbig.text(38, -1.5, "6", fontsize = 16, color = 'red')
axbig.text(38, -4.5, "7", fontsize = 16, color = 'red')
axbig.text(41, 4.5, "8", fontsize = 16, color = 'red')
axbig.text(41, 1.5, "9", fontsize = 16, color = 'red')
axbig.text(41, -1.5, "10", fontsize = 16, color = 'red')
axbig.text(41, -4.5, "11", fontsize = 16, color = 'red')
axbig.set_title("Grid Reference", fontsize = 16)
axbig.text(35, -5.0,u'\u25B2 \nN ', ha='center', fontsize=24,
                                  family='Arial', rotation = 0)
axbig.add_artist(ScaleBar(6000, location = 'lower right', dimension
                                   = 'si-length'))

for i in range(11):
    if i == 0 or i == 1 or i == 2:
        gg = 'intg'+str(i+1)+".xlsx"
        gi = pd.read_excel(gg)
        axs[i, 1].plot(gi.date, gi.avg*1000, color = 'royalblue')
        axs[i, 1].set_title("Grid "+str(i+1), fontsize = 14)
        axs[i, 1].tick_params(axis = 'x', labelsize = 12)
        axs[i, 1].tick_params(axis = 'y', labelsize = 12)
        axs[i, 1].set_ylabel("EWT(mm)", fontsize = 14)
        axs[i, 1].set_xlabel("Year", fontsize = 14)
        axs[i,1].set_xlim(min(gi.date), max(gi.date))
        xval = np.arange(gi['date'].size)
        coef = np.polyfit(xval, gi.avg*1000, 1)
        coef1 = np.polyfit(gi.date, gi.avg*1000, 1)
        poly = np.poly1d(coef)
        yhat = poly(xval)
        axs[i, 1].plot(gi.date, yhat, 'k')
        axs[i, 1].set_yticks([-400, -200, 0, 200, 400])
        axs[i, 1].set_xticks([2002.5, 2005.0, 2007.5, 2010.0, 2012.
                                          5, 2015.0,
                              2017.5, 2020.0])
        axs[i, 1].text(2002.5, 270, "Mean trend = "+str(round(coef1
                                          [0], 3))+ "mm/yr",
                                          fontsize = 12)

    elif i ==3:
        gg = 'g'+str(i+1)+".xlsx"
        gi = pd.read_excel(gg)
        axs[i, 0].plot(gi.date, gi.avg*1000, color = 'royalblue')
        axs[i, 0].set_title("Grid "+str(i+1), fontsize = 14)
        axs[i, 0].tick_params(axis = 'x', labelsize = 12)
        axs[i, 0].tick_params(axis = 'y', labelsize = 12)
        axs[i, 0].set_ylabel("EWT(mm)", fontsize = 14)
        axs[i, 0].set_xlabel("Year", fontsize = 14)
        axs[i,0].set_xlim(min(gi.date), max(gi.date))
        xval = np.arange(gi['avg'].size)
        coef = np.polyfit(xval, gi.avg*1000, 1)
        coef1 = np.polyfit(gi.date, gi.avg*1000, 1)
```

```
        poly = np.poly1d(coef)
        yhat = poly(xval)
        axs[i, 0].plot(gi.date, yhat, ’k’)
        axs[i, 0].set_yticks([-400, -200, 0, 200, 400])
        axs[i, 0].set_xticks([2002.5, 2005.0, 2007.5, 2010.0, 2012.
                                          5, 2015.0,
                              2017.5, 2020.0])
        axs[i, 0].text(2002.5, 270, "Mean trend = "+str(round(coef1
                                          [0], 3))+ "mm/yr",
                                          fontsize = 12)

    elif i%2 == 0:
        gg = ’g’+str(i+1)+".xlsx"
        gi = pd.read_excel(gg)
        ii = int(i/2 + 1)
        axs[ii, 1].plot(gi.date, gi.avg*1000, color = ’royalblue’)
        axs[ii, 1].set_title("Grid "+str(i+1), fontsize = 14)
        axs[ii, 1].tick_params(axis = ’x’, labelsize = 12)
        axs[ii, 1].tick_params(axis = ’y’, labelsize = 12)
        axs[ii, 1].set_ylabel("EWT(mm)", fontsize = 14)
        axs[ii, 1].set_xlabel("Year", fontsize = 14)
        axs[ii,1].set_xlim(min(gi.date), max(gi.date))
        xval = np.arange(gi[’avg’].size)
        coef = np.polyfit(xval, gi.avg*1000, 1)
        coef1 = np.polyfit(gi.date, gi.avg*1000, 1)
        poly = np.poly1d(coef)
        yhat = poly(xval)
        axs[ii, 1].plot(gi.date, yhat, ’k’)
        axs[ii, 1].set_yticks([-400, -200, 0, 200, 400])
        axs[ii, 1].set_xticks([2002.5, 2005.0, 2007.5, 2010.0, 2012
                                          .5, 2015.0,
                              2017.5, 2020.0])
        axs[ii, 1].text(2002.5, 270, "Mean trend = "+str(round(
                                          coef1[0], 3))+ "mm/yr",
                                          fontsize = 12)

    elif i%2!=0:
        gg = ’g’+str(i+1)+".xlsx"
        gi = pd.read_excel(gg)
        i2 = int((i-1)/2) + 2
        axs[i2, 0].plot(gi.date, gi.avg*1000, color = ’royalblue’)
        axs[i2, 0].set_title("Grid "+str(i+1), fontsize = 14)
        axs[i2, 0].tick_params(axis = ’x’, labelsize = 12)
        axs[i2, 0].tick_params(axis = ’y’, labelsize = 12)
        axs[i2, 0].set_ylabel("EWT(mm)", fontsize = 14)
        axs[i2, 0].set_xlabel("Year", fontsize = 14)
        axs[i2,0].set_xlim(min(gi.date), max(gi.date))
        xval = np.arange(gi[’avg’].size)
        coef = np.polyfit(xval, gi.avg*1000, 1)
        coef1 = np.polyfit(gi.date, gi.avg*1000, 1)
        poly = np.poly1d(coef)
        yhat = poly(xval)
        axs[i2, 0].plot(gi.date, yhat, ’k’)
        axs[i2, 0].set_yticks([-400, -200, 0, 200, 400])
```

```
        axs[i2, 0].set_xticks([2002.5, 2005.0, 2007.5, 2010.0, 2012
                                          .5, 2015.0,
                              2017.5, 2020.0])
        axs[i2, 0].text(2002.5, 270, "Mean trend = "+str(round(
                                          coef1[0], 3))+ "mm/yr",
                                          fontsize = 12)


fig.tight_layout()
plt.savefig("grids_new.svg", dpi = 300)
plt.show()
```

B.0.2 Figures 20, 21 and 22

```
# -*- coding: utf-8 -*-
"""
Created on Tue May 30 13:11:54 2023

@author: YMBALE001
"""

import numpy as np
import pandas as pd
import matplotlib.pyplot as plt
from scipy.stats import pearsonr

fig, axs = plt.subplots(2, 2)
axs = axs.ravel()

v = []
r = []
ch = []
count = 0
for i in range(14):
    gdfrm  = 'P'+str(i+1)+'.xlsx'
    gv = pd.read_excel(gdfrm)
    dt2 = gv.iloc[1:, 3]
    v.append(dt2)

    vel = np.array(v).ravel()
    yr = np.array(gv.iloc[1:, 1])

    if i==3 or i==4 or i==11 or i==12:
        axs[count].set_title("Point "+str(i+1), fontsize = 14)
        axs[count].plot(yr, vel, color = 'firebrick')
        axs[count].scatter(yr, vel, color = 'blue', marker = "*")
        axs[count].set_ylabel("Deformation (mm)", fontsize = 12)
        axs[count].set_xlabel("Year", fontsize = 12)
        axs[count].tick_params(axis = 'y', labelsize = 12)
        axs[count].tick_params(axis = 'x', labelsize = 12)
        coef = np.polyfit(yr, vel, 1)
        poly = np.poly1d(coef)
        yhat = poly(yr)
        axs[count].plot(yr, yhat, "--", color = 'black')
```

```
        axs[count].text(2018, 1200, "Mean Trend = "+str(round(coef[
                                            0], 3))+" mm/yr",
                                            fontsize = 12)
        cf, p = pearsonr(yr, vel)
        axs[count].set_yticks([-1500, -1000, -500, 0, 500, 1000,
                                            1500])
        axs[count].set_xlim(2015.04, 2021.9)

        count += 1

    ch.append(vel[-1])
    v.clear()
    r.clear()

for ax in axs.flat:
    ax.label_outer()

plt.tight_layout()
plt.savefig("desc_diss.svg", dpi = 300)
plt.show()
```

B.0.3 Figures 23, 24, 25, 26, 27, 28 and 29

```
# -*- coding: utf-8 -*-
"""
Created on Mon Aug 21 18:22:43 2023

@author: YMBALE001
"""

import pandas as pd
import numpy as np
import matplotlib.pyplot as plt

fig, axs = plt.subplots(2, 2)
axs = axs.ravel()

count = 0

for i in range(14):
    df = 'gld_no'+str(i+1)+".xlsx"
    gi = pd.read_excel(df)
    vv = gi.Def
    ddd = gi.date
    df1 = 'intg'+str(i+1)+".xlsx"
    gi1 = pd.read_excel(df1)
    ws = gi1.Def
    dd1 = gi1.date


    if i==3 or i==4 or i==12 or i==13:
        k = int(i/2)
        axs[count].set_title('Point '+str(i+1), fontsize = 14)
        GRACE, = axs[count].plot(dd1, ws)
        GLDAS, = axs[count].plot(ddd, vv)
```

```
        axs[count].legend([GLDAS, GRACE], ["GLDAS", "GRACE"], loc =
                                           "lower right")
        plt.xlim(min(ddd), max(ddd))
        axs[count].tick_params(axis='x', labelsize = 12)
        axs[count].tick_params(axis='y', labelsize = 12)
        coefgr = round((np.polyfit(dd1[9:], ws[9:], 1))[0],3)
        coefgl = round((np.polyfit(ddd, vv, 1))[0],3)
        axs[count].text(2010, -25, "Mean Trend", fontsize = 12)
        axs[count].text(2010, -35, "GRACE: "+str(coefgl)+" mm",
                                          fontsize = 12)
        axs[count].text(2010, -50, "GLDAS: "+str(coefgr)+" mm",
                                          fontsize = 12)
        axs[count].set_yticks([-60, -45, -30, -15, 0, 15, 30])
        axs[count].set_ylim(-60, 30)
        axs[count].set_xlim(2003, 2022)

        count += 1

for ax in axs.flat:
    ax.set_ylabel('Difference (mm)', fontsize = 12)
    ax.set_xlabel('Years', fontsize = 12, loc = 'center')
    ax.label_outer()

plt.tight_layout()
plt.savefig("grace_gldas_no_outliers_line.svg", dpi = 300)
```

B.0.4 Figures 31, 33, 48 and 49

```
# -*- coding: utf-8 -*-
"""
Created on Fri Mar 31 03:52:22 2023

@author: YMBALE001
"""

import numpy as np
import pandas as pd
import matplotlib.pyplot as plt

wdf = pd.read_excel("wet.xlsx")
col = np.int64(np.array(wdf.columns)[1:])
nms = np.array(wdf.iloc[:, 0])


x = np.arange(len(col))
width = 0.22
multiplier = 0

fig, ax = plt.subplots()
plt.rcParams['figure.figsize'] = [8, 8]

wdf2 = wdf.iloc[:, 1:]
clr = ['saddlebrown', 'red', 'forestgreen', 'blue']
for value, columns in enumerate(wdf2):
    if value == 0 or value == 1 or value ==2 or value ==3:
```

```
        a = np.float64(np.array(wdf2.iloc[value, :]/10000))
        offset = width * multiplier
        xx = x + offset
        rect = ax.bar(xx, a, width, label = nms[value], color = clr
                                          [value])
        multiplier += 1


ax.set_ylabel("Area (Ha)", fontsize = 14)
ax.set_xlabel("Year", fontsize = 14)
ax.set_title("LULC Wet Season", fontsize = 20)
ax.set_yticks([0, 100000, 200000, 300000, 400000, 450000])
ax.tick_params(axis = 'both', labelsize = 14)
ax.legend(loc = 'upper left', ncol = 1, fontsize = "large")
ax.set_xticks(ticks = (x + width), labels = col)
plt.savefig("LULC Wet Season.png")
plt.show()

fig2, al = plt.subplots(2, 2)
plt.rcParams['figure.figsize'] = [12, 10]

at = al.ravel()
cl = ['forestgreen', 'saddlebrown', 'red', 'blue']
for k in range(len(wdf2)):
    yr = np.array(wdf2.columns, dtype = np.int64)
    val = np.array(wdf2.iloc[k])/10000
    at[k].scatter(yr, val, color = clr[k], marker = ".", s=172,
                                      edgecolor = 'slategrey')
    at[k].set_title(nms[k], fontsize = 20)
    at[k].set_ylim(0, 450000)
    at[k].set_xlim(1984, 2021)
    at[k].tick_params(labelsize = 14)
    coef = np.polyfit(yr, val, 1)
    poly = np.poly1d(coef)
    yhat = poly(yr)
    at[k].plot(yr, yhat, color = 'black')
    at[k].text(1975, 140000, "Mean Trend :"+str(round(coef[0],3))+
                                      " ha",
                fontsize = 14)
    at[k].text(1975, 90000, "y = "+str(round(coef[0], 3))+"x + "+
                                      str(round(coef[1], 3)),
              fontsize = 14)
    at[k].set_xlim(1984, 2022)
    at[k].set_xticks([1973, 1980, 1984, 1990, 1995, 2000, 2005,
                                      2010, 2015, 2020, 2022])
    at[k].tick_params(axis = 'x', rotation = 90)

for ax in at.flat:
    ax.set_xlabel("Year", fontsize = 14)
    ax.set_ylabel("Area (ha)", fontsize = 14)
    ax.label_outer()

fig2.tight_layout()
plt.savefig('lulc_wet_season_trend.png')
plt.show()
```

B.0.5 Figures 38, 39 and 42

```
# -*- coding: utf-8 -*-
"""
Created on Wed Jun  7 16:52:10 2023

@author: YMBALE001
"""

import numpy as np
import pandas as pd
import matplotlib.pyplot as plt
from scipy.stats import pearsonr

test = pd.read_excel("dfrmP1.xlsx")
test2 = pd.read_excel("precipP1.xlsx")

pos = []
for a in range(len(test)):
    aa = test2.iloc[a, 1]
    bb = np.array(test.iloc[:, 1])
    dd = abs(bb - aa)
    ind = np.argmin(dd)
    pos.append(ind)


fig, ax = plt.subplots(2, 2)
ax = ax.ravel()
v = []
r = []
count = 0
for i in range(14):
    gprp = 'precipP'+str(i+1)+'.xlsx'
    gdfrm  = 'dfrmP'+str(i+1)+'.xlsx'
    gp = pd.read_excel(gprp)
    gv = pd.read_excel(gdfrm)
    dt1 = gp.iloc[:, 2]
    dt2 = gv.iloc[:, 2]
    v.append(dt2)
    r.append(dt1)

    vel = np.array(v).ravel()
    prcp = np.array(r).ravel()
    yr = np.array(gv.iloc[:, 1])
    yr2 = np.array(gp.iloc[:, 1])

    if i==3 or i==4 or i==11 or i==12:
        ax[count].set_title("Point "+str(i+1), fontsize = 14)
        ax[count].bar(yr2, prcp, width = 0.08, edgecolor = 'black')
        ax[count].set_ylabel("Precipitation (mm)", fontsize = 12)
        ax[count].set_xlabel("Year", fontsize = 12)
        ax[count].tick_params(axis = 'y', labelsize = 12)
        ax[count].tick_params(axis = 'x', labelsize = 12)
        ax[count].set_yticks([0, 200, 400, 600, 800, 1000])
        ax[count].set_xlim(2015, 2021.9)
```

```
    if i==3 or i==4 or i==11 or i==12:
        axs = ax[count].twinx()
        axs.plot(yr, vel, color = 'firebrick')
        axs.scatter(yr, vel, color = 'blue', marker = "*")
        axs.set_ylabel("Deformation (mm)", fontsize = 12)
        axs.tick_params(axis = 'y', labelsize = 12)
        axs.tick_params(axis = 'x', labelsize = 12)
        axs.set_yticks([-1500, -1000, -500, 0, 500, 1000])

        count +=1

    v.clear()
    r.clear()

for ax in ax.flat:
    ax.label_outer()

plt.tight_layout()
plt.savefig("desc_rain_diss.svg", dpi=300)
plt.show()
```

B.0.6 Figures 40, 41 and 43

```
# -*- coding: utf-8 -*-
"""
Created on Wed Jun  7 18:20:41 2023

@author: YMBALE001
"""

import numpy as np
import pandas as pd
import matplotlib.pyplot as plt
from scipy.stats import pearsonr

test = pd.read_excel("dfrmP1.xlsx")
test2 = pd.read_excel("precipP1.xlsx").iloc[154:,]

pos = []
for a in range(len(test)):
    aa = test2.iloc[a, 1]
    bb = np.array(test.iloc[1:, 1])
    dd = abs(bb - aa)
    ind = np.argmin(dd)
    pos.append(ind)


fig, axs = plt.subplots(2, 2)
axs = axs.ravel()
v = []
r = []
count = 0
for i in range(14):
    gprp = 'precipP'+str(i+1)+'.xlsx'
```

```
    gdfrm  = ’dfrmP’+str(i+1)+’.xlsx’
    gp = pd.read_excel(gprp)
    gv = pd.read_excel(gdfrm)
    dt1 = gp.iloc[pos, 2]
    dt2 = gv.iloc[:, 2]
    v.append(dt2)
    r.append(dt1)

    vel = np.array(v).ravel()
    prcp = np.array(r).ravel()
    if i==3 or i==4 or i==12 or i==13:
        axs[count].set_title("Point "+str(i+1), fontsize = 14)
        axs[count].scatter(prcp, vel, color = ’mediumblue’, marker
                                          = ’^’, s = 24, edgecolor
                                          = ’hotpink’)
        axs[count].set_ylabel("Deformation (mm)", fontsize = 12)
        axs[count].set_xlabel("Precipitation (mm)", fontsize = 12)
        axs[count].tick_params(axis = ’y’, labelsize = 12)
        axs[count].tick_params(axis = ’x’, labelsize = 12)
        coef = np.polyfit(prcp, vel, 1)
        poly = np.poly1d(coef)
        yhat = poly(prcp)
        axs[count].plot(prcp, yhat, ".-", color = ’black’)
        axs[count].text(150, -500, "y = "+str(round(coef[0], 3))+"x
                                           + "+str(round(coef[1], 3
                                          )),
                  fontsize = 12)
        cf, p = pearsonr(prcp, vel)
        axs[count].text(150, -900, "r = "+str(round(cf, 3)),
                                          fontsize = 12)
        axs[count].set_yticks([-1000, -500, 0, 500, 1000, 1500])
        axs[count].set_xticks([0, 50, 100, 150, 200, 250, 300])
        axs[count].set_xlim(0, 300)

        count +=1

    v.clear()
    r.clear()

for ax in axs.flat:
    ax.label_outer()

plt.tight_layout()
plt.savefig("desc_rain_correlation_diss.svg", dpi = 300)
plt.show()
```

B.0.7 Figures 44, 45, 46 and 47

```
-*- coding: utf-8 -*-
"""
Created on Thu Dec 29 18:56:50 2022

@author: YMBALE001
"""
```

```
import numpy as np
from scipy.stats import pearsonr
import matplotlib.pyplot as plt
import pandas as pd
from sklearn.metrics import r2_score

fig, axs = plt.subplots(3, 1)
plt.rcParams['figure.figsize'] = [12, 16]

for i in range(3):
    fl = "f"+str(i+1)+".txt"
    f2 = pd.read_csv(fl)

    s = f2.Aspect
    v = f2.Velocity

    axs[i].scatter(s, v, color = 'black', marker = '.', s = 24)
    axs[i].tick_params(axis = 'x', labelsize = 12)
    axs[i].tick_params(axis = 'y', labelsize = 12)
    coef = np.polyfit(s, v, 1)
    poly = np.poly1d(coef)
    yhat = poly(s)
    axs[i].plot(s, yhat, color = 'red')
    axs[i].text(min(s)+80, 520, "y = "+str(round(coef[0], 2))+"x +
                                      "+str(round(coef[1], 2)),
              fontsize = 16)
    cf, p = pearsonr(s, v)
    corr_matrix = np.corrcoef(s, v)
    corr = corr_matrix[0,1]
    r2 = corr**2
    axs[i].text(min(s)+80, 470, "r = "+str(round(cf, 2)), fontsize
                                      = 16)
    axs[i].set_yticks([-300, -200, -100, 0, 100, 200, 300, 400, 500
                                      , 600, 700])
    axs[i].set_xticks([0, 60, 120, 180, 240, 300, 360])
    axs[i].tick_params(axis='x', labelsize = 16)# rotation = 90)
    axs[i].tick_params(axis='y', labelsize = 16)

    if i == 0:
        axs[i].text(min(s)+80, 620, "ALOS PALSAR", fontsize = 16)
    if i == 1:
        axs[i].text(min(s)+80, 620, "Sentinel-1 Ascending",
                                      fontsize = 16)
    if i == 2:
        axs[i].text(min(s)+80, 620, "Sentinel-1 Descending",
                                      fontsize = 16)


for ax in axs.flat:
    ax.set_ylabel('Deformation (mm)', fontsize = 16)
    ax.set_xlabel('Aspect (Degree)', fontsize = 16, loc = 'center')
    ax.label_outer()

plt.tight_layout()
plt.savefig("aspectcorr.png", dpi = 300)
```

```
plt.show()

fig, axs = plt.subplots(3, 1)
plt.rcParams['figure.figsize'] = [12, 16]

for i in range(3):
    f1 = "f"+str(i+1)+".txt"
    f2 = pd.read_csv(f1)

    s = f2.Elevation
    v = f2.Velocity

    axs[i].scatter(s, v, color = 'black', marker = '.', s = 24)
    axs[i].tick_params(axis = 'x', labelsize = 12)
    axs[i].tick_params(axis = 'y', labelsize = 12)
    coef = np.polyfit(s, v, 1)
    poly = np.poly1d(coef)
    yhat = poly(s)
    axs[i].plot(s, yhat, color = 'red')
    axs[i].text(max(s)-1050, 250, "y = "+str(round(coef[0], 2))+"x
                                      + "+str(round(coef[1], 2)),
              fontsize = 16)
    cf, p = pearsonr(s, v)
    corr_matrix = np.corrcoef(s, v)
    corr = corr_matrix[0,1]
    r2 = corr**2
    axs[i].text(max(s)-1050, 180, "r = "+str(round(cf, 2)),
                                      fontsize = 16)
    axs[i].set_yticks([-300, -200, -100, 0, 100, 200, 300, 400, 500
                                      ])
    axs[i].set_xticks([0, 1000, 2000, 3000, 4000, 5000])
    axs[i].tick_params(axis='x', labelsize = 16)# rotation = 90)
    axs[i].tick_params(axis='y', labelsize = 16)

    if i == 0:
        axs[i].text(max(s)-1050, 420, "ALOS PALSAR", fontsize = 16)
    if i == 1:
        axs[i].text(max(s)-1050, 420, "Sentinel-1 Ascending",
                                          fontsize = 16)
    if i == 2:
        axs[i].text(max(s)-1050, 420, "Sentinel-1 Descending",
                                          fontsize = 16)


for ax in axs.flat:
    ax.set_ylabel('Deformation (mm)', fontsize = 16)
    ax.set_xlabel('Elevation (m)', fontsize = 16, loc = 'center')
    ax.label_outer()

plt.tight_layout()
plt.savefig("elevationcorr.png", dpi = 300)
plt.show()

fig, axs = plt.subplots(3, 1)
plt.rcParams['figure.figsize'] = [12, 16]
```

```
for i in range(3):
    fl = "f"+str(i+1)+".txt"
    f2 = pd.read_csv(fl)

    s = f2.SR
    v = f2.Velocity

    axs[i].scatter(s, v, color = 'black', marker = '.', s = 24)
    axs[i].tick_params(axis = 'x', labelsize = 12)
    axs[i].tick_params(axis = 'y', labelsize = 12)
    coef = np.polyfit(s, v, 1)
    corr_matrix = np.corrcoef(s, v)
    corr = corr_matrix[0,1]
    r2 = corr**2
    poly = np.poly1d(coef)
    yhat = poly(s)
    axs[i].plot(s, yhat, color = 'red')
    axs[i].text(max(s)-0.07, 380, "y = "+str(round(coef[0], 2))+"x
                                      + "+str(round(coef[1], 2)),
              fontsize = 16)
    cf, p = pearsonr(s, v)
    axs[i].text(max(s)-0.07, 300, "r = "+str(round(cf, 2)),
                                      fontsize = 16)
    axs[i].set_yticks([-300, -200, -100, 0, 100, 200, 300, 400, 500
                                      ])
    axs[i].set_xticks([0, 0.05, 0.10, 0.15, 0.20, 0.25])
    axs[i].tick_params(axis='x', labelsize = 16)# rotation = 90)
    axs[i].tick_params(axis='y', labelsize = 16)

    if i == 0:
        axs[i].text(max(s)-0.07, 450, "ALOS PALSAR", fontsize = 16)
    if i == 1:
        axs[i].text(max(s)-0.07, 450, "Sentinel-1 Ascending",
                                          fontsize = 16)
    if i == 2:
        axs[i].text(max(s)-0.07, 450, "Sentinel-1 Descending",
                                          fontsize = 16)


for ax in axs.flat:
    ax.set_ylabel('Deformation (mm)', fontsize = 16)
    ax.set_xlabel('Surface Roughness', fontsize = 16, loc = 'center
                                      ')
    ax.label_outer()

plt.tight_layout()
plt.savefig("surfaceroughnesscorr.png", dpi = 300)
plt.show()
```

Appendix C

Confusion Matrices

Table 10: 1973 Classified Wet Season Confusion Matrix

Overall Accuracy = (19969/20568) 97.0877%

Kappa Coefficient = 0.9077

Class	Ground Truth (Pixels)				
	Built up Area	Water	Vegetation	Bare Land	Total
Unclassified	0	0	0	0	0
Built up Area	4	0	9	0	13
Water	2	0	364	0	366
Vegetation	15	1	3476	91	3583
Bare Land	0	10	107	16489	16606
Total	21	11	3956	16580	20568

Class	Ground Truth (Percent)				
	Built up Area	Water	Vegetation	Bare Land	Total
Unclassified	0.00	0.00	0.00	0.00	0.00
Built up Area	19.05	0.00	0.23	0.00	0.06
Water	9.52	0.00	9.20	0.00	1.78
Vegetation	71.43	9.09	87.87	0.55	17.42
Bare Land	0.00	90.91	2.70	99.45	80.74
Total	100.00	100.00	100.00	100.00	100.00

Class	Commission (Percent)		Omission (Percent)	
	Commission (Percent)	Omission (Percent)	Commission (Pixels)	Omission (Pixels)
Built up Area	69.23	80.95	9/13	17/21
Water	100.00	100.00	366/366	11/11
Vegetation	2.99	12.13	107/3583	480/3956
Bare Land	0.70	0.55	117/16606	91/16580

Class	Prod. Acc. (Percent)		User Acc. (Percent)	
	Prod. Acc. (Percent)	User Acc. (Percent)	Prod. Acc. (Pixels)	User Acc. (Pixels)
Built up Area	19.05	30.77	4/21	4/13
Water	0.00	0.00	0/11	0/366
Vegetation	87.87	97.01	3476/3956	3476/3583
Bare Land	99.45	99.30	16489/16580	16489/16606

Table 11: 1984 Classified Wet Season Confusion Matrix

Overall Accuracy = (82031/82486) 99.4484%

Kappa Coefficient = 0.9864

Class	Ground Truth (Pixels)				
	Water	Vegetation	Bare Land	Built up Area	Total
Unclassified	0	0	0	0	0
Water	136	0	0	0	136
Vegetation	0	22608	67	1	22676
Bare Land	0	0	59276	0	59276
Built up Area	0	387	0	11	398
Total	136	22995	59343	12	82486

Class	Ground Truth (Percent)				
	Water	Vegetation	Bare Land	Built up Area	Total
Unclassified	0.00	0.00	0.00	0.00	0.00
Water	100.00	0.00	0.00	0.00	0.16
Vegetation	0.00	98.32	0.11	8.33	27.49
Bare Land	0.00	0.00	99.89	0.00	71.86
Built up Area	0.00	1.68	0.00	91.67	0.48
Total	100.00	100.00	100.00	100.00	100.00

Class	Commission (Percent)		Omission (Percent)	
	Commission (Percent)	Omission (Percent)	Commission (Pixels)	Omission (Pixels)
Water	0.00	0.00	0/136	0/136
Vegetation	0.30	1.68	68/22676	387/22995
Bare Land	0.00	0.11	0/59276	67/59343
Built up Area	97.24	8.33	387/398	1/12

Class	Prod. Acc. (Percent)		User Acc. (Percent)	
	Prod. Acc. (Percent)	User Acc. (Percent)	Prod. Acc. (Pixels)	User Acc. (Pixels)
Water	100.00	100.00	136/136	136/136
Vegetation	98.32	99.70	22608/22995	22608/22676
Bare Land	99.89	100.00	59276/59343	59276/59276
Built up Area	91.67	2.76	11/12	11/398

Table 12: 2002 Classified Wet Season Confusion Matrix

Overall Accuracy = (46928/46930) 99.9957%
Kappa Coefficient = 0.9999

Class	Ground Truth (Pixels)				
	Water	Bare Land	Vegetation	Built up Area	Total
Unclassified	0	0	0	0	0
Water	1167	0	0	0	1167
Bare Land	0	41772	0	0	41772
Vegetation	2	2307	60019	0	62328
Built up Area	0	51	0	120	171
Total	1169	44130	60019	120	105438

Class	Ground Truth (Percent)				
	Water	Bare Land	Vegetation	Built up Area	Total
Unclassified	0.00	0.00	0.00	0.00	0.00
Water	99.83	0.00	0.00	0.00	1.11
Bare Land	0.00	94.66	0.00	0.00	39.62
Vegetation	0.17	5.23	100.00	0.00	59.11
Built up Area	0.00	0.12	0.00	100.00	0.16
Total	100.00	100.00	100.00	0.00	100.00

Class	Commission (Percent)		Omission (Percent)	
	Commission (Percent)	Omission (Percent)	Commission (Pixels)	Omission (Pixels)
Water	0.00	0.17	0/1167	2/1169
Bare Land	0.00	5.34	0/41772	2358/44130
Vegetation	3.70	0.00	2309/62328	0/60019
Built up Area	29.82	0.00	51/171	0/120

Class	Prod. Acc. (Percent)		User Acc. (Percent)	
	Prod. Acc. (Percent)	User Acc. (Percent)	Prod. Acc. (Pixels)	User Acc. (Pixels)
Water	99.83	100.00	1167/1169	1167/1167
Bare Land	94.66	100.00	41772/44130	41772/41772
Vegetation	100.00	96.30	60019/60019	60019/62328
Built up Area	100.00	70.18	120/120	120/171

Table 13: 2013 Classified Wet Season Confusion Matrix

Overall Accuracy = (24276/24408) 99.4592%
Kappa Coefficient = 0.9890

Class	Ground Truth (Pixels)				
	Built up Area	Vegetation	Water	Bare Land	Total
Unclassified	0	0	0	0	0
Built up Area	16	16	0	101	133
Vegetation	0	14926	0	0	14926
Water	0	0	420	0	420
Bare Land	1	12	2	8914	8929
Total	17	14954	422	9015	24408

Class	Ground Truth (Percent)				
	Built up Area	Vegetation	Water	Bare Land	Total
Unclassified	0.00	0.00	0.00	0.00	0.00
Built up Area	94.12	0.11	0.00	1.12	0.54
Vegetation	0.00	99.81	0.00	0.00	61.15
Water	0.00	0.00	99.53	0.00	1.72
Bare Land	5.88	0.08	0.47	98.88	36.58
Total	100.00	100.00	100.00	100.00	100.00

Class	Commission (Percent)		Omission (Percent)	
	Commission (Percent)	Omission (Percent)	Commission (Pixels)	Omission (Pixels)
Built up Area	87.97	5.88	117/133	1/17
Vegetation	0.00	0.19	0/14926	28/14954
Water	0.00	0.47	0/420	2/422
Bare Land	0.17	1.12	15/8929	101/9015

Class	Prod. Acc. (Percent)		User Acc. (Percent)	
	Prod. Acc. (Percent)	User Acc. (Percent)	Prod. Acc. (Pixels)	User Acc. (Pixels)
Built up Area	94.12	12.03	16/17	16/133
Vegetation	99.81	100.00	14926/14954	14926/14926
Water	99.53	100.00	420/422	420/420
Bare Land	98.88	99.83	8914/9015	8914/8929

Table 14: 2022 Classified Wet Season Confusion Matrix

Overall Accuracy = (66242/66272) 99.9547%

Kappa Coefficient = 0.9987

Class	Ground Truth (Pixels)				
	Built up Area	Vegetation	Water	Bare Land	Total
Unclassified	0	0	0	0	0
Built up Area	16	20	0	0	36
Vegetation	7	51199	3	0	51209
Water	0	0	541	0	541
Bare Land	0	0	0	14486	14486
Total	23	51219	544	14486	66272

Class	Ground Truth (Percent)				
	Built up Area	Vegetation	Water	Bare Land	Total
Unclassified	0.00	0.00	0.00	0.00	0.00
Built up Area	69.57	0.04	0.00	0.00	0.05
Vegetation	30.43	99.96	0.55	0.00	77.27
Water	0.00	0.00	99.45	0.00	0.82
Bare Land	0.00	0.00	0.00	100.00	21.86
Total	100.00	100.00	100.00	100.00	100.00

Class	Commission (Percent)		Omission (Percent)	
	Commission (Percent)	Omission (Percent)	Commission (Pixels)	Omission (Pixels)
Built up Area	55.56	30.43	20/36	7/23
Vegetation	0.02	0.04	10/51209	20/51219
Water	0.00	0.55	0/541	3/544
Bare Land	0.00	0.00	0/14486	0/14486

Class	Prod. Acc. (Percent)		User Acc. (Percent)	
	Prod. Acc. (Percent)	User Acc. (Percent)	Prod. Acc. (Pixels)	User Acc. (Pixels)
Built up Area	69.57	44.44	16/23	16/36
Vegetation	99.96	99.98	51199/51219	51199/51209
Water	99.45	100.00	541/544	541/541
Bare Land	100.00	100.00	14486/14486	14486/14486

Table 15: 1984 Classified Dry Season Confusion Matrix

Overall Accuracy = (52605/52616) 99.9791%
Kappa Coefficient = 0.9996

Class	Ground Truth (Pixels)				
	Bare Land	Vegetation	Built up Area	Water	Total
Unclassified	0	0	0	0	0
Bare Land	29257	0	0	1	29258
Vegetation	0	23336	0	10	23346
Built up Area	0	0	12	0	12
Water	0	0	0	0	0
Total	29257	23336	12	11	52616

Class	Ground Truth (Percent)				
	Bare Land	Vegetation	Built up Area	Water	Total
Unclassified	0.00	0.00	0.00	0.00	0.00
Bare Land	100.00	0.00	0.00	9.09	55.61
Vegetation	0.00	100.00	0.00	90.91	44.37
Built up Area	0.00	0.00	100.00	0.00	0.02
Water	0.00	0.00	0.00	0.00	0.00
Total	100.00	100.00	100.00	100.00	100.00

Class	Commission (Percent)		Omission (Percent)	
	Commission (Percent)	Omission (Percent)	Commission (Pixels)	Omission (Pixels)
Bare Land	0.00	0.00	1/29258	0/29257
Vegetation	0.04	0.00	10/23346	0/23336
Built up Area	0.00	0.00	0/12	0/12
Water	0.00	100.00	0/0	11/11

Class	Prod. Acc. (Percent)		User Acc. (Percent)	
	Prod. Acc. (Percent)	User Acc. (Percent)	Prod. Acc. (Pixels)	User Acc. (Pixels)
Bare Land	100.00	100.00	29257/29257	29257/29258
Vegetation	100.00	99.96	23336/23336	23336/23346
Built up Area	100.00	100.00	12/12	12/12
Water	0.00	0.00	0/11	0/0

Table 16: 2002 Classified Dry Season Confusion Matrix

Overall Accuracy = (25002/25037) 99.8602%
Kappa Coefficient = 0.9968

Class	Ground Truth (Pixels)				
	Built up Area	Bare Land	Water	Vegetation	Total
Unclassified	0	0	0	0	0
Built up Area	418	0	0	0	418
Bare Land	35	17678	0	0	17713
Water	0	0	499	0	499
Vegetation	0	0	0	6407	6407
Total	453	17678	499	6407	25037

Class	Ground Truth (Percent)				
	Built up Area	Bare Land	Water	Vegetation	Total
Unclassified	0.00	0.00	0.00	0.00	0.00
Built up Area	92.27	0.00	0.00	0.00	1.67
Bare Land	7.73	100.00	0.00	0.00	70.75
Water	0.00	0.00	100.00	0.00	1.99
Vegetation	0.00	0.00	0.00	100.00	25.59
Total	100.00	100.00	100.00	100.00	100.00

Class	Commission (Percent)		Omission (Percent)	
	Built up Area (Percent)	Bare Land (Percent)	Built up Area (Pixels)	Built up Area (Pixels)
Built up Area	0.00	7.73	0/418	35/453
Bare Land	0.20	0.00	35/17713	0/17678
Water	0.00	0.00	0/499	0/499
Vegetation	0.00	0.00	0/6407	0/6407

Class	Prod. Acc. (Percent)		User Acc. (Percent)	
	Built up Area (Percent)	Bare Land (Percent)	Built up Area (Pixels)	Built up Area (Pixels)
Built up Area	92.27	100.00	418/453	418/418
Bare Land	100.00	99.80	17678/17678	17678/17713
Water	100.00	100.00	499/499	499/499
Vegetation	100.00	100.00	6407/6407	6407/6407

Table 17: 2013 Classified Dry Season Confusion Matrix

Overall Accuracy = (21604/21611) 99.9676%

Kappa Coefficient = 0.9993

Class	Ground Truth (Pixels)				
	Built up Area	Vegetation	Bare Land	Water	Total
Unclassified	0	0	0	0	0
Built up Area	7	0	0	0	7
Vegetation	7	7232	0	0	7239
Bare Land	0	0	14156	0	14156
Water	0	0	0	209	209
Total	14	7232	14156	209	21611

Class	Ground Truth (Percent)				
	Built up Area	Vegetation	Bare Land	Water	Total
Unclassified	0.00	0.00	0.00	0.00	0.00
Built up Area	50.00	0.00	0.00	0.00	0.03
Vegetation	50.00	100.00	0.00	0.00	33.50
Bare Land	0.00	0.00	100.00	0.00	65.50
Water	0.00	0.00	0.00	100.00	0.97
Total	100.00	100.00	100.00	100.00	100.00

Class	Commission (Percent)		Omission (Percent)	
	Built up Area (Percent)	Vegetation (Percent)	Built up Area (Pixels)	Vegetation (Pixels)
Built up Area	0.00	50.00	0/7	7/14
Vegetation	0.10	0.00	7/7239	0/7232
Bare Land	0.00	0.00	0/14156	0/14156
Water	0.00	0.00	0/209	0/209

Class	Prod. Acc. (Percent)		User Acc. (Percent)	
	Prod. Acc. (Percent)	User Acc. (Percent)	Prod. Acc. (Pixels)	User Acc. (Pixels)
Built up Area	50.00	100.00	7/14	7/7
Vegetation	100.00	99.90	7232/7232	7232/7239
Bare Land	100.00	100.00	14156/14156	14156/14156
Water	100.00	100.00	209/209	209/209

Table 18: 2022 Classified Dry Season Confusion Matrix

Overall Accuracy = (31936/32377) 98.6379%
Kappa Coefficient = 0.9701

Class	Ground Truth (Pixels)				
	Vegetation	Bare Land	Water	Built up Area	Total
Unclassified	0	0	0	0	0
Vegetation	9693	0	0	0	9693
Bare Land	0	21627	0	1	21628
Water	0	0	284	0	284
Built up Area	64	376	0	332	772
Total	9757	22003	284	333	32377

Class	Ground Truth (Percent)				
	Vegetation	Bare Land	Water	Built up Area	Total
Unclassified	0.00	0.00	0.00	0.00	0.00
Vegetation	99.34	0.00	0.00	0.00	29.94
Bare Land	0.00	98.29	0.00	0.30	66.80
Water	0.00	0.00	100.00	0.00	0.88
Built up Area	0.66	1.71	0.00	99.70	2.38
Total	100.00	100.00	100.00	100.00	100.00

Class	Commission (Percent)		Omission (Percent)	
	Vegetation (Percent)	Bare Land (Percent)	Built up Area (Pixels)	Built up Area (Pixels)
Vegetation	0.00	0.66	0/9693	64/9757
Bare Land	0.00	1.71	1/21628	376/22003
Water	0.00	0.00	0/284	0/284
Built up Area	56.99	0.30	440/772	1/333

Class	Prod. Acc. (Percent)		User Acc. (Percent)	
	Prod. Acc. (Percent)	User Acc. (Percent)	Prod. Acc. (Pixels)	User Acc. (Pixels)
Vegetation	99.34	100.00	9693/9757	9693/9693
Bare Land	98.29	100.00	21627/22003	21627/21628
Water	100.00	100.00	284/284	284/284
Built up Area	99.70	43.01	332/333	332/772